The Thesis Committee for Santiago Adolfo Morales
Certifies that this is the approved version of the following thesis:

Investigation of High Strain Rate Behavior of Metallic Specimens Using Electromagnetic Inductive Loading

APPROVED BY
SUPERVISING COMMITTEE:

Supervisor:

Krishnaswamy Ravi-Chandar

Kenneth M. Liechti

Investigation of High Strain Rate Behavior of Metallic Specimens Using Electromagnetic Inductive Loading

by

Santiago Adolfo Morales, B.M.E.

Thesis

Presented to the Faculty of the Graduate School of

The University of Texas at Austin

in Partial Fulfillment

of the Requirements

for the Degree of

Master of Science in Engineering

The University of Texas at Austin

August 2011

Dedication

To my mother Ana Isabel Zamora.

Acknowledgements

I would like to thank my advisor, Professor Krishnaswamy Ravi-Chandar for giving me the opportunity to work on the problems described in this document, as well as the resources and guidance necessary to explore them. Professor Ravi-Chandar has been a great mentor, and his input enriched my experience at The University of Texas enormously. Many thanks are in order to Professor Kenneth Liechti for his guidance and support throughout my stay at the University; his input helped me to expand my understanding of many topics, and made the learning experience a richer one. I would also like to express my gratitude to Aaron Albrecht, Ali Ghahremaninezhad and Fasset Hickey for all their help with the experimental work described herein and to Joseph Pokluda, Pablo Cortes and Travis Crooks for their excellent work in manufacturing many of the samples and components used in these experiments as well as their tutelage in many other aspects. Finally, I would like to say thank you to my fellow graduate students for all their help and for making my graduate experience a great one.

August 2011

Abstract

Investigation of High Strain Rate Behavior of Metallic Specimens Using Electromagnetic Inductive Loading

Santiago Adolfo Morales, M.S.E.

The University of Texas at Austin, 2011

Supervisor: Krishnaswamy Ravi-Chandar

The aim of this thesis is to explore the high strain rate behavior of metallic specimens using electromagnetic inductive loading as the means to inflict the required high strain rate deformation on laboratory scale specimens, allowing for controlled, repeatable experiments to be performed. Three separate experiments were designed and performed, using helical and spiral coils as the sources of radial and unidirectional loading.

The first experiment evaluated the effect of applying a polymer coating on 30.5 mm diameter, Al 6061- O tube samples, in two lengths, 18 and 36 mm. The expanding tube experiment was used to apply a radial loading on the specimens and record the event. Several optical techniques were then used to evaluate the behavior of the samples. Coatings of polyurea and polycarbonate were used. It was observed that the polycarbonate coating seemed to have a more profound effect on the behavior of the metal, by applying a larger restraining pressure on the tube surface during the expansion process, and thereby modifying the stress state of the specimen.

The second experiment looked to design an experimental arrangement to test the plane strain, high strain rate behavior of Al 6061-O tubes of different lengths. A 112 mm long solenoid was designed and manufactured, and testing was performed on 30.5 mm diameter Al 6061-O tubes in lengths of 50, 70 and 90 mm. It was observed that the coil behaved similar to shorter ones at low voltages and that the longer the specimen used, the more its deformation path approached a plane strain condition.

Finally, a third experiment was performed to develop a method to accelerate a flat metallic plate to high linear velocities, as a means to evaluate the use of a flat spiral coil as the driver for future experiments based upon electromagnetic inductive loading. A prototype coil was manufactured and installed into a converted expanding tube experimental setup. Three samples were tested in several sizes, and materials: aluminum and steel. Speeds in the range of 45 to 251 m/s were obtained, validating the apparatus as a viable method to provide a unidirectional loading.

Table of Contents

List of Tables x

List of Figures xi

Chapter 1: Introduction 1

1.1 High Strain-Rate Material Characterization 4

1.2 Outline of Present Study 6

Chapter 2: Experimental Methods 8

2.1 Electromagnetic Inductive Loading 8

2.1.1 Helical Coils 9

2.1.1.1 Expanding Ring/Tube Experiment 10

2.1.1.2 Expanding Tube Experiment with Polymer Coated Al 6061-O Tubes 18

2.1.1.3 Plane Strain Testing of Tube Specimens Using the Expanding Tube Experiment 21

2.1.2 Spiral Coils 28

2.1.2.1 Design of an Experimental Method for Rapid Acceleration of Metallic Plates to High Velocities 29

Chapter 3: Experimental Results 34

3.1 Effect of Applying a Polymer Coating on the Localization and Fragmentation of Al 6061-O Tubes 34

3.2 Plane Strain Expanding Tube Testing of Al 6061-O Samples 47

3.3 Design of an Experimental Method for Rapid Acceleration of Metallic Plates to High Linear Velocities 56

Chapter 4: Conclusions and Recommendations 62

4.1 Effect of Applying a Polymer Coating on the Localization and Fragmentation of Al 6061-O Tubes 63

4.2 Plane Strain Expanding Tube Testing of Al 6061-O Samples 64

4.3 Design of an Experimental Method for Rapid Acceleration of Metallic Plates to High Linear Velocities 67

Appendices.....115

A. Engineering Drawings for Winding Mandrel, Polycarbonate Core and Machining of 112 mm Solenoid 115

B. Engineering Drawings for Vertical Mold Used to Cover 112 mm Solenoid Winding in Epoxy.....120

References.....127

Vita 129

List of Tables

Table 1. List of high speed expanding tube tests on polymer coated Al 6061-O samples.....84

Table 2. List of high speed expanding tube tests on bare Al 6061-O samples.....85

Table 3. List of high speed, plane strain expanding tube tests on bare Al 6061-O samples.....102

Table 4. List of flat plate acceleration tests on bare Al 6061-O and steel samples.....108

List of Figures

Figure 2.1 69
Figure 2.2 69
Figure 2.3 70
Figure 2.4 71
Figure 2.5 72
Figure 2.6 73
Figure 2.7 73
Figure 2.8 74
Figure 2.9 74
Figure 2.10 75
Figure 2.11 75
Figure 2.12 76
Figure 2.13 77
Figure 2.14 78
Figure 2.15 79
Figure 2.16 80
Figure 2.17 81
Figure 2.18 82
Figure 2.19 83
Figure 3.1 86
Figure 3.2 87
Figure 3.3 88
Figure 3.4 89

Figure 3.5 90
Figure 3.6 90
Figure 3.7 91
Figure 3.8 92
Figure 3.9 93
Figure 3.10 93
Figure 3.11 94
Figure 3.12 95
Figure 3.13 96
Figure 3.14 97
Figure 3.15 98
Figure 3.16 99
Figure 3.17 100
Figure 3.18 101
Figure 3.19 101
Figure 3.20 103
Figure 3.21 104
Figure 3.22 104
Figure 3.23 105
Figure 3.24 105
Figure 3.25 106
Figure 3.26 107
Figure 3.27 109
Figure 3.28 110
Figure 3.29 111

Figure 3.30 112
Figure 3.31 112
Figure 3.32 113
Figure 3.33 114

Chapter 1: Introduction

Understanding the high strain-rate localization and fragmentation behavior of metals is critical in a large number of applications; from standard manufacturing techniques, like punching and drawing, to extreme high-speed deformation scenarios such as blast resistance of armor plating. Investigation in this area is based on work performed by Mott (1947), where the fragmentation of pipe bombs was analyzed to generate a criterion that allows for the prediction of the size and kinetic energy distribution of fragments created under a dynamic loading. However, in order to analyze the localization and fragmentation of these dynamic events, they need to be performed, in a relatively controlled, repeatable fashion. Experimentation to study this behavior has been performed since the late 1800's, utilizing ingenious ways of applying the necessary driving force to test samples of multiple metals, such as Al 6061-O, Al 6061-T6, Al 1100-O, Al 1100-H14, Al A5052, OFHC copper, 101 copper, Armco Iron, HF-1 steel, AerMet 100 steel, AISI 1080 steel, 304 stainless steel and U-6% Nb uranium alloy. These techniques include gas powered projectile impacts, pressure wave interaction and electromagnetic inductive loading techniques. A brief summary of the evolution of the above research is presented here.

The work by the Hopkinsons (1872, 1910) represents the most renowned early experimental research on the subject. They carried out experiments based on impact loading on long wires to evaluate their strength. Von Karman and Duwez (1950) impacted a wire with a projectile to generate higher strain rates and then measured the plastic wave propagation in the wire to determine the strength. Kolsky (1949) utilized the Hopkinson bar apparatus to create the split-Hopkinson pressure bar apparatus, which has since then allowed for a large amount of experimentation in high strain rate

characterization of tensile stress-strain behavior of materials. Tensile fracture and fragmentation was initially studied by Niordson (1965) who developed an electromagnetic loading arrangement to expand a metallic ring. This arrangement was subsequently exploited by Grady and Benson (1983) to expand OFHC copper and 1100-O aluminum rings to strain rates in the range of 10^2 - 10^4 s^{-1}. Niordson used photography to document his experiment, and through his observations concluded that fractures seem to occur almost simultaneously on the samples and that this fracture occurred after shear localization at an angle to the direction of tension. Gourdin (1989) incorporated a Velocity Interferometer System for Any Reflector (VISAR) to the expanding ring experiment to measure the expansion velocity of the ring sample accurately.

Walling and Forrestal (1973) modified Niordson's expanding ring apparatus to accommodate cylindrical samples. Wesenberg and Sagartz (1977) consequently used this arrangement to test Al 6061-T6 tubes. The modification utilized a contoured copper sheet placed inside the specimen to conduct a current discharge. Lorentz force interaction between the copper sheet and the specimen caused the sample expansion; this arrangement provided strain rates in the order of 10^4 s^{-1} and a high-speed camera was used to document the event. Shear localization bands at an angle of 30º from the direction of tension were observed.

Winter (1979) developed a technique to expand tube samples where a gas fired projectile impacted an elastomeric insert placed inside the specimen. The impact would deform the elastomer in such a way that it would try to bulge; however since it was encased by the specimen, it would apply a pressure loading on it, causing the expansion. The pressure pulse would move along the specimen in an axial direction. Strain rates in the range of 2-4x10^4 s^{-1} were achieved and again high speed photography was used to observe the events. Forrestal et al. (1980) developed an explosive loading technique,

were a PETN charge was exploded inside a specimen and the rapid gas expansion would apply a pressure on the specimen internal wall, causing it to expand. A mesh was used to ensure uniform pressure distribution throughout the specimen. It was observed that the strain at initial fracture increased as the thickness of the specimen increased. Mock and Holt (1983) performed a similar experiment without the use of the mesh, generating uneven pressure distribution.

Most of the experimental work in existence on the expanding tube topic was performed using pressure loadings created by explosives or projectile-elastomer interaction. However, this led to non-uniform expansion of the tubes due to a variable pressure loading on the surface of the specimen (except for the work by Forrestal et al. 1980). Using electromagnetic inductive loading provides a much more uniform deformation, obtaining a better characterization of the material properties. Jansen (1968) developed an expanding tube method utilizing a solenoid (helical coil) inside the cylindrical specimen to induce the expansion. The Lorentz force was induced by discharging a large voltage, stored in a capacitor bank, quickly through the coil, using a heavily damped circuit. The material used in this case was Al 6061-O with the intention of forming it into a larger radius cylinder. The radius and magnetic field evolution were measured directly.

Electromagnetic inductive loading can also be used to propel flat plate specimens to very high velocities. Seth et al. (2005) examined the formability of sheet steel under high velocity impact, by using a flat spiral wound coil and an aluminum driver plate to accelerate steel plates against different shaped punches – wedge shaped to induce a plane strain deformation path, and axisymmetric (missile-shaped) to induce bi-axial stress states. Speeds in the range of 50 – 220 m/s were achieved and it was concluded that the useful formability of low-ductility steels could be dramatically improved by this mode of

forming and that the ductility of materials that already had a good quasi-static formability was not affected substantially. Oliveira et al. (2005) performed similar experiments on aluminum alloy sheets using a double spiral flat coil. In this case the specimens were clamped down. Maximum speeds of 250 – 300 m/s were obtained. Strain rates in the range of 2000 – 3000 s^{-1} were observed. No indications of obtaining much larger strain levels prior to the onset of failure compared to traditional forming methods were observed.

1.1 High Strain-Rate Material Characterization

Experiments such as split-Hopkinson bar tests, drop weight apparatus tension tests, exploding wire pressure loading tests and expanding ring/tube tests have been performed by numerous investigators; these are either limited to compressive stress states or to low strain rate tension experiments. The expanding ring/tube experiments are of special relevance in this thesis because they are able to probe the high strain-rate dynamic tensile properties of materials.

In recent work, Zhang and Ravi-Chandar (2006) used an expanding ring setup similar to those described above, where the driving force for the experiment was provided by a helical coil wound without pitch; Chapter 2 describes this arrangement in detail. Thin Al 6061-O rings were used as specimens, with cross-sectional dimensions of 0.5 x 1 mm and a diameter of 30.5 mm. A custom designed high-speed camera, with high spatial and temporal resolution was used to document the events. Strain rates in the range of 4000 – 10,000 s^{-1} were observed. The results indicated that neither strain-rate dependence of the constitutive response of the material, nor inertial effects, that were speculated would push the onset of necking to larger strain levels, were observed.

Similar experiments were performed on Al 1100-H14, Al 6061-O and Cu 101 specimens with varying aspect ratios (Zhang and Ravi-Chandar, 2008). The same loading system was used to achieve strain rates in the range of 4000 – 10,000 s^{-1}. It was observed that geometrical and inertial effects control the propagation of localization across the cross-sectional dimension and this in turn dictates the uniform strain levels that may be achieved under high strain rate uniaxial tension. Zhang, Liechti and Ravi-Chandar (2009) studied the effect of compliant coatings on the onset of localization in metallic specimens under high strain rate loading. Interest in this topic developed from the use of such coatings for improved armor protection, as described by Mathews (2004). The specimens used consisted of Al 6061-O and Cu 101 rings coated with polyurea. The expanding ring experiment used in the previous papers was also used here to expand the rings at high strain rates in the range of 4000 – 15,000 s^{-1}. It was observed that the coating did not affect the onset of localization in any meaningful manner. Additionally, nucleation and propagation of the localization were not significantly affected by the presence of the polyurea and it was noted that adhesion between the polymer and the metal layer is an important parameter that was worth exploring further. Finally, Zhang and Ravi-Chandar (2010) explored the dynamic failure of cylindrical Al 6061-O specimens – 30.5 mm in diameter in lengths of 18 and 36 mm. A modified expanding ring experimental arrangement was used, where a longer solenoid was used, together with a conical mirror and a different high-speed digital camera (Cordin Model 550). The conical mirror allowed for a real time tracking of the local strain on the surface of the specimens; Chapter 2 also describes this arrangement thoroughly. The specimens were expanded at strain rates in the range of 4000 – 15,000 s^{-1}. It was observed that the tube specimens experienced uniform expansion until a critical strain, followed by almost simultaneous nucleation of shear band localization, and eventually by fracture at the

intersection of the shear bands. An approximately uniaxial stress state was observed in the 18 mm specimens, while a slight migration towards a plane strain deformation path was observed in the 36 mm tubes. Localization developed in the form of shear bands oriented at about 54º from the tensile loading direction. Finally, it was also observed that the specimens conformed to the quasi static-forming limit for the material.

From the above experimental work and the lessons learned from it, interest in several topics was developed. In particular, three areas are to be explored:

- An evaluation of the effect of adding a polymer coating on Al 6061-O tubes is desired, as to assess if the effect of the coating on the base material behavior changes with the added length. Polyurea is the polymer of choice, due to its importance as described earlier.
- Plane strain testing is of interest. This deformation path might constrain the type of localization experienced by the specimen.
- High strain rate behavior of plate specimens needs to evaluated, to form a better understanding of localization and fragmentation under a biaxial tensile stress state.

1.2 Outline of Present Study

The aim of the work performed in this thesis was to approach the above topics of interest and either perform the required testing, or develop suitable test methods. Because of the existence of a proven expanding tube experimental setup for 18 mm and 36 mm long tubes, the effect of adding a polymer coating on these was investigated using this setup. Two polymer coatings were investigated, polyurea and polycarbonate; this allowed a better characterization of the effect of the coating, by exploring the effect of

having different material constitutive properties. Al 6061-O was the base material again, to allow for a direct comparison to previous experimental work.

Additionally, initial experimental setup design was performed for the plane strain testing of tubes and for the flat plate acceleration. For the former, a design for a longer solenoid was carried out, and the current expanding tube setup was modified to accommodate this new solenoid; testing was then performed with multiple samples to characterize the operation of the new equipment. The goal was to evaluate the plane strain tendencies of the specimens, to fine tune an experimental procedure for future testing. For the latter, a proof-of-concept experimental arrangement was developed, to explore how the driving system (flat spiral coil) for this type of experimentation behaves. In order to do this, new experimental hardware was developed, and the expanding tube experiment was retro-fitted to incorporate this experimental scheme. Finally, testing was performed on flat plates to evaluate the nature of the coil – specimen interaction.

This thesis is organized as follows: in Chapter 2 the concepts employed to perform the required testing and manufacture the necessary components are described. Detailed instructions as well as any particulars associated with each test are presented. The results from the individual tests, as well as detailed descriptions of the observed behaviors with the corresponding quantitative analysis are included in Chapter 3. Finally, Chapter 4 presents conclusions on the obtained results and evaluates further steps that are recommended to continue and improve the work performed here.

Chapter 2: Experimental Methods

In this work, the principle of electromagnetic inductive loading is used to perform three different experiments; firstly the dynamic localization and fragmentation properties of polymer coated Al 6061-O are studied. Secondly, an experimental setup is designed to test the localization and fragmentation properties of Al 6061-O in a plane strain condition. Finally, an experimental setup is also designed to accelerate flat metallic plates to high speeds. The following describes in detail the experimental concepts and procedures used in these tests.

2.1 Electromagnetic Inductive Loading

Electromagnetic inductive loading refers to the application of forces on a body that are caused by the effects of electromagnetic interactions. Faraday stated that an electric current will be induced in a closed circuit whenever the magnetic flux through the conductor changes. Furthermore, Lenz' Law states that the direction of said induced current will be opposed to the motion or varying magnetic flux causing it. Additionally, Lorentz forces are developed by the interaction of electric and magnetic fields and are dependent on the magnitude of these vectors. For example, for a point charge,

$$\boldsymbol{F} = q[\boldsymbol{E} + (\boldsymbol{v} \times \boldsymbol{B})] \tag{2.1}$$

where $\boldsymbol{F}$ is the Lorentz force, q is the electric charge of the particle, $\boldsymbol{E}$ is the electric field, $\boldsymbol{v}$ is the instantaneous velocity of the particle and $\boldsymbol{B}$ is the magnetic field; all quantities in bold are vector quantities.

Therefore, if an alternating current is passed through a wire next to a metallic sample, a current will be induced in the sample and this current will flow in the opposite direction as the one in the wire. Additionally, this interaction will cause opposing

Lorentz forces to develop, pushing the wire and sample away from each other. The magnitude of this repulsion is then dependent on the magnitude of the current flowing through the wire. This is the principle behind electromagnetic inductive loading (EML). By restricting the motion of the wire, the sample can then be repelled by a force equivalent to the Lorentz forces developed between the conductors.

By having more wires in proximity to the specimen, or the same wire interacting several times with the sample, stronger Lorentz forces can be generated; therefore a larger driving force can be applied. Coil structures permit the latter to be accomplished; the most typical configurations are helical and spiral arrangements. For the work described in this document, both of these were used. The former were implemented to study the high strain rate deformation of polymer coated Al 6061-O tubes as well as plane strain expansion of tubes of the same material. The latter were explored as means of applying a loading on metallic plates to accelerate them. The following sections explain the particular details of the hardware and experimental setups used.

2.1.1 Helical Coils

In the context of EML, helical coils are utilized to apply radial loads on cylindrical specimens placed concentrically over the coil. These are ideal for this task, as the magnetic field interactions between the coil and the sample produce an almost purely radial loading, since the components of the Lorentz forces along the axis of the cylinder cancel out. The pitch of the helix affects the actual orientation of the fields, determining the level to which this cancellation occurs; the smaller the pitch, the larger the cancellation. Helical coils are the core of the expanding ring/tube experiment which is the main experimental tool used in the work with Al 6061-O tubes described here.

2.1.1.1 Expanding Ring/Tube Experiment

The principle of EML for this experiment is simple. The specimen consists of an aluminum ring or tube, of radius r_0 and cross sectional dimensions t and h. The sample is inserted over a helical coil (solenoid) of n turns ideally wound without pitch (to provide a purely radial loading), making sure that the central plane of the sample is in line with the central plane of the solenoid. When a current I_1, flows through the solenoid, a current I_2 develops in the specimen. The interaction between these generates Lorentz forces that cause both bodies to repel each other. The coil is rigidly constrained, causing the tube to expand radially. A 20kV, 25 μF capacitor is discharged to generate I_1; the current generated by this event can produce a loading on the sample that can accelerate it to expansion speeds up to 200 m/s, depending on the actual specimen and discharge voltage used. The switching of the circuit is performed by using a thyratron-ignitron circuit that is synchronized with the data recording systems. Figure 2.1 shows this conceptual arrangement. The solenoid-ring/tube system can be considered as two equivalent RLC circuits: a main circuit containing the capacitor and solenoid, and a simple secondary circuit containing the specimen. The current in the main circuit is measured using a Rogowski coil that loops around the wire connecting the capacitor to the solenoid. The current in the secondary circuit can be calculated by measuring the current through both the solenoid and the sample with another Rogowski coil. This instrument measures $nI_1 + I_2$, where n is the number of turns in the solenoid, I_1 is the current in the main circuit and I_2 is the current in the secondary circuit. Therefore, by knowing I_1 and n, I_2 can be obtained.

The expanding ring experiment is a one-dimensional problem and is simpler than the expanding tube. However, the analysis of both is similar. For the expanding ring, analyzing the described circuits in detail allows for a relationship to be established

between the expansion velocity of the samples and the current in the circuit, as shown by Zhang and Ravi-Chandar (2006). For the main circuit, Kirchhoff's voltage law gives

$$C\frac{dV}{dt} = I_1$$

$$V + R_1 I_1 + L_{11}\frac{dI_1}{dt} + \frac{d(L_{12}I_2)}{dt} = 0 \tag{2.1}$$

where C is the capacitance, $R_1$is the resistance of the solenoid circuit, $L_{11}$is the self-inductance of the solenoid, $L_{12}$is the mutual inductance between the solenoid and the ring specimen, V is the discharge voltage and I_1 and I_2 are the currents in the main and secondary circuits respectively.

For the secondary circuit,

$$R_2 I_2 + \frac{d(L_{22}I_2)}{dt} + \frac{d(L_{12}I_1)}{dt} = 0 \tag{2.2}$$

where R_2 is the resistance of the tube, L_{22} is the self inductance of the ring. L_{12} and L_{22} are both functions of the separation between the sample and the coil, or in other words, functions of the instantaneous radius of the ring $r(t)$. Introducing this into Eqs (2.1) and (2.2), we obtain,

$$\ddot{I_1} = -\frac{R_1}{L_{11}}\dot{I_1} - \frac{L_{12}}{L_{11}}\ddot{I_2} - \frac{2\dot{I_2}\dot{r}+I_2\ddot{r}}{L_{11}}\frac{dL_{12}}{dr} - \frac{I_2\dot{r}^2}{L_{11}}\frac{d^2L_{12}}{dr^2} - \frac{I_1}{L_{11}C} \tag{2.3}$$

$$\dot{I_2} = -\frac{R_2}{L_{22}}I_2 - \frac{L_{12}}{L_{22}}\dot{I_1} - \frac{I_1\dot{r}}{L_{22}}\frac{dL_{12}}{dr} - \frac{I_2\dot{r}}{L_{22}}\frac{dL_{22}}{dr} \tag{2.4}$$

The self-inductance of the ring is given by

$$L_{22} \approx 4\pi r\left[\left(1+\frac{r_w^2}{8r^2}\right)\ln\frac{8r}{r_w} + \frac{r_w^2}{24r^2} - \frac{7}{4}\right] \text{ x } 10^{-7}$$

$$\approx 4\pi r\left[\ln\frac{8r}{r_w} - \frac{7}{4}\right] \text{ x } 10^{-7} \tag{2.5}$$

where $r_w = \sqrt{\frac{A}{\pi}}$ is the area-equivalent cross-section radius of the ring. For the expanding ring test, $\frac{r_w}{r} < 10$, therefore the simplification shown in Eq. (2.5) can be made.

The mutual inductance of the solenoid and the ring can be calculated from

$$L_{12} = 2\mu_0 \sum_{i=1}^{N} \frac{\sqrt{r_i r}}{k}\left[\left(1 - \frac{k^2}{2}\right)K(k) - E(k)\right] \tag{2.6}$$

where

$$k = \sqrt{\frac{4r_i r}{(r_i + r)^2 + z_i^2}}$$

$$K(k) = \int_0^{\pi/2} \frac{d\theta}{\sqrt{1 - k^2 \sin^2\theta}}$$

$$E(k) = \int_0^{\pi/2} \sqrt{1 - k^2 \sin^2\theta}\, d\theta$$

and r_i is the radius of the i coil loop and z_i is the perpendicular distance between the plane of this coil loop and the central plane of the ring.

Looking at the radial expansion of the ring, the following equation describes the total energy of the system, and can be used to obtain the equation of motion for the specimen.

$$W = \frac{1}{2}CV^2 + \int_0^t (R_1 I_1^2 + R_2 I_2^2)dt + \frac{1}{2}\sum_{i=1}^{2}\sum_{j=1}^{2} L_{ij} I_i I_j$$
$$+ \tfrac{1}{2} M\dot{r}^2 + \int_0^t 2\pi A \dot{r}\sigma(\epsilon)dt \tag{2.7}$$

where the first term is the energy stored in the capacitor, the second term corresponds to the dissipation of energy in the resistors, the third term refers to the

inertia of the inductors (i, j correspond to the main and secondary circuits), the fourth term is the kinetic energy of the specimen (assuming a rigid solenoid) and the last term is the mechanical work done by the ring. M is the mass of the ring, A and r are the cross-sectional area and the mean radius of the ring, ρ is the mass density of the specimen and $\sigma(\epsilon)$ is the constitutive law for the sample material. Letting $dW = 0$ and recalling Eqs. (2.3) and (2.4), we obtain that the acceleration of the expanding ring is

$$\ddot{r} = \frac{I_1 I_2}{2\pi r A \rho}\frac{dL_{12}}{dr} + \frac{I_2^2}{4\pi r A \rho}\frac{dL_{22}}{dr} - \frac{\sigma}{\rho r} \tag{2.8}$$

For a given $\sigma(\epsilon)$, Eqs. (2.3)-(2.6) and (2.8) must be solved simultaneously to determine the variation in r. dL_{22}/dt can be calculated from Eq. (2.5), dL_{12}/dt on the other hand is more difficult to obtain and is simplified by considering that

$$\frac{dL_{12}}{dt} = 2\pi r\, b(r) \tag{2.9}$$

where $b(r)$ is the magnetic induction of the solenoid. Essentially, the solenoid is approximated as a stack of identical circular rings in planes parallel to that of the sample. The magnetic field at r can be calculated by the Biot-Savart Law, such that the axial and radial components of the field produced by coil i are

$$b_i^z(r) = \frac{\mu_0}{2\pi}\int_0^{\pi} \frac{r_i^2 - r_i r\cos\theta}{(r^2 - 2rr_i\cos\theta + r_i^2 + z_i^2)^{\frac{3}{2}}}\, d\theta \tag{2.10}$$

$$b_i^r(r) = \frac{\mu_0}{2\pi} r z_i \int_0^{\pi} \frac{1}{(r^2 - 2rr_i\cos\theta + r_i^2 + z_i^2)^{\frac{3}{2}}}\, d\theta \tag{2.11}$$

where r_i and z_i are the same as described previously. Additionally, it can be shown that $b^z(r) = 0$ for all loops due to symmetry when the ring is placed in the center of the solenoid, therefore from Eqs. (2.9) and (2.11)

$$\frac{1}{2\pi r}\frac{dL_{12}}{dr} = b(r) = \sum_{Loop_i} b_i^r(r) = \frac{\mu_0}{2\pi}\sum_{Loop_i}\int_0^{\pi} \frac{1}{\left(r^2-2rr_i\cos\theta+r_i^2+z_i^2\right)^{\frac{3}{2}}}d\theta \quad (2.12)$$

Eq. (2.12) is then used in Eq. (2.8) to calculate dL_{12}/dt.

The temperature of the specimen can change considerably if the Joule heating and plastic work effects are large enough. In order to account for these, the heat balance equation needs to be incorporated into the formulation. Due to the very rapid nature of the experiment, an adiabatic condition can be assumed, causing the temperature change to be given by

$$\dot{T}_s = \frac{R_2 I_2^2}{2\pi r A C_p \rho} + \frac{\sigma \dot{\epsilon}_p}{C_p \rho} \quad (2.13)$$

where C_p is the specific heat capacity of the specimen and $\dot{\epsilon_p}$ is the plastic strain rate experienced by the ring. Because of the large straining of the sample, elastic strains can be ignored, allowing the approximation $\dot{\epsilon_p} = \dot{r}/r$ to be used. With this, Eqs. (2.3)-(2.6), (2.8), (2.12) and (2.13) can be solved numerically to calculate the ring expansion history for a given $\sigma(\epsilon)$. Jansen (1968) provides a similar model for the expanding tube experiment.

In order to track the expansion of the ring/tube specimens, a high-speed camera is needed. For the experiments performed in this work, a Cordin Model 550 high-speed camera was used. This camera is capable of recording 30 frames at speeds of 400,000 frames per second with a spatial resolution of 1000 x 1000 pixels. Additionally, two xenon flash lamps and a conical diffusing reflector were used to illuminate the sample. Finally, a conical mirror was employed to observe the entire surface of the tube specimen and consequently measure the strain evolution on the surface in real time, as performed

by Zhang and Ravi-Chandar (2010). Figure 2.2 illustrates the full experimental configuration.

The conical mirror is placed behind the specimen in a coaxial manner, such that the entire surface of the sample is reflected. This reflection is projected onto the focal plane of the camera and appears as an annular band around the solenoid in the direct view image of the solenoid-tube arrangement. If the cone angle of the mirror is known, the projected image of the specimen surface can be unwrapped to a rectangular band, showing a complete view of the entire surface. Figure 2.3 shows the details of the geometrical optics for this mapping process (for this experiment $2\alpha = 130^{\circ}$). The unwrapping is achieved by mapping a point $V(p,q)$ on the reflected annular band, to a point $M(m,n)$ in the unwrapped rectangular image. This is achieved through the following relationships:

$$p = p_0 - r\sin\theta, \text{ and } q = q_0 - r\cos\theta \tag{2.14}$$

where $r = r_i + h(w-m)/w$ and $\theta = 2\pi n/u$. u and w are the length and width of the unwrapped image, and can be obtained from $u = 2\pi r_s$ and $w = h/\sin(2\pi - 2\alpha)$, where r_s is the tube radius in the direct image of the solenoid-tube arrangement and h is the tube width in the projected annular band. Figure 2.4 illustrates the unwrapping concept. This procedure is particularly sensitive to misalignment between the sample and mirror, as well as non-perfectly axisymmetric deformations of the sample. The errors in strain associated with measurements made from the unwrapped images were estimated to be $\pm 3\%$ by Zhang and Ravi-Chandar (2010), assuming that quantitative measurements were restricted to areas where the deformation may be considered to be reasonably axisymmetric.

The main quantitative measurements that can be made of the samples in the expanding tube experiment are: evolution of the current in the sample, tube radius evolution, tube radial expansion speed, global hoop strain evolution and local hoop and axial strain evolution on the tube surface. The current measurement is obtained from the Rogowski coils, as described previously.

The tube radius evolution and radial expansion speeds can be obtained from measuring the radius of the sample in the different frames recorded by the high-speed camera and calculating its rate of change. An average global strain evolution can also be calculated from these measurements. The sample radius must be calculated as an average because the expansion of the specimen is not perfectly uniform, resulting in a slight elliptical shape of the expanded tube. The average global strain is defined as

$$\epsilon = \ln \frac{r}{r_0} \tag{2.15}$$

where r is the mean radius of the sample in the image of interest, and r_0 is the initial radius of the tube. The local hoop and axial strain evolution can be obtained by measuring the evolution of a circular pattern on the specimen surfaces as a function of time. This is possible by using the unwrapped images of the events. It is worth noting that during the tests, the samples tend to barrel slightly as they expand; this means that the edges of the sample will be at a further distance from the conical mirror than the middle portions of the sample, causing a slight error in the size of the circles in the reflected image. This discrepancy induces a scaling error in the unwrapped image, affecting the measured strain. The center portion (lengthwise) of the sample is affected less by this phenomenon, therefore taking the local measurements of strain here will yield a more representative value for the local strain of the specimen. It must also be considered that the barreling of the specimen implies that the radial expansion of the center section of the

tube will be greater than that of the edges. Since the average global strain is determined by measuring the variation of the sample radius at the edge closest to the camera, the obtained strain level will be smaller than that measured locally; the level of the discrepancy will depend on the degree of barreling observed. The surface pattern used consists of a grid of circles, 2.719 mm in external diameter, electrolytically etched onto the aluminum tubes; these deform into ellipses where the major axis corresponds to the hoop direction of the sample. The local hoop strain is calculated by

$$\epsilon_1 = \ln \frac{d}{d_0} \tag{2.16}$$

where d and d_0 are the length of the major axis of the deformed circles in the unwrapped images and the original circle diameter respectively. The local axial strain (ϵ_2) is calculated in the same way, but replacing the major axis length of the deformed circle with the minor axis length.

The etching process used to mark the sample surface consists of the following: a fabric covered electrode (anode) is wetted with an electrolyte (Electrolyte solution LNC 9 by Lectroetch); then a mask with the desired pattern is laid on the anode. The aluminum specimens are then fitted onto a Teflon mandrel and slowly rolled over the mask while in contact with the cathode of the circuit. As the circuit is closed, aluminum particles migrate from the sample through the openings in the mask, to the anode, etching a pattern on the specimens. Once the etching is complete the samples are washed with Formula 1 All Purpose Cleaner by Lectroetch.

The specific solenoid details for the expanding ring experiment depend on the actual goal of the test. The following sections illustrate the different helical coil designs used for the specific experiments carried out in this work.

2.1.1.2 Expanding Tube Experiment with Polymer Coated Al 6061-O Tubes

The goal of this set of experiments was to analyze the effect of applying a uniform polymer coating on the localization and fragmentation of Al 6061-O tubes, while subjecting the specimens to high strain rate deformation. In order to evaluate this, an experiment had to be performed that allowed for a direct comparison between the obtained results and existing data for bare Al 6061-O tubes expanded in the same manner. Zhang and Ravi-Chandar (2010) carried out 12 tests on Al 6061-O cylinders using the expanding tube experiment described earlier, where they characterized the localization and fragmentation dynamics of 30.5 mm diameter tubes with a wall thickness of 0.5 mm and lengths of 18 and 36 mm. In order to make a valid comparison between the polymer coated results and the data presented by Zhang and Ravi-Chandar (2010), the experiment had to be duplicated exactly, but with the addition of the polymer coating. In this case two polymers were investigated: polyurea and polycarbonate.

Zhang and Ravi-Chandar used two different solenoids for their experiments, both made from 16-gauge square cross-section magnet copper wire. Their design was identical except for the number of turns used and therefore the length of the coil. The 18 mm tube samples were expanded using a 6 turn coil, wound without pitch, where the separation of the turns was selected so that the turns would span 18mm in total and be equally spaced. The 36 mm tube samples used a 12 turn coil, spanning 36 mm. The goal was to achieve a uniform distribution of driving force in the tube specimen.

The coil manufacturing procedure consisted of several steps. Firstly, a bakelite core was machined to have grooves perpendicular to the core longitudinal axis, ensuring a coil winding with no pitch. Next, the square copper wire was threaded through the grooves to form the coil. The entire assembly was then covered with a bakelite sleeve and potted in epoxy to hold together and electrically insulate it, avoiding arcing between

consecutive wire loops; the cured part was later machined to the desired dimension. Finally, electrical insulation was added to the exposed leads, and ring connectors were soldered on. Figure 2.5 illustrates this procedure. The coil design was evolved from analysis performed by Zhang and Ravi-Chandar (2006) for the coil used in expanding ring experiments.

The tube samples used by Zhang and Ravi-Chandar were selected to allow for large strains before localization, and to investigate the length dependence of the tube behavior. Their diameter and thickness was defined to match the samples used in their initial ring experiments. The exact length was determined from experimentation to avoid barreling and flaring of the sample, allowing for a uniform radial expansion. The aluminum specimens were machined from Al 6061-T6 tube stock to the desired dimensions and finally annealed to achieve the Al 6061-O condition. The annealing process consisted of heating the material to 760 F, holding the temperature for 3 hours and then cooling down the sample in 50 F steps, lasting one hour each, until 500 F was reached; then the oven was turned off and the samples were allowed to cool to room temperature. The annealed material displayed the true stress – true strain behavior presented in Figure 2.6 for uniaxial tension tests. This constitutive law can be approximated by a power law of the form

$$\sigma = \sigma_y\left(1 + \beta\epsilon_p\right)^n \tag{2.17}$$

where $\beta = 14165$, $n = 0.22$ and $\sigma_y = 25$ MPa. The strain at the onset of localization was found to be $\epsilon_N^{qs} = 0.22$. All the specimens used for the polymer coated experiments were prepared in the manner described above, and were obtained from the same stock material.

All Al 6061-O tubes were electro-etched per the procedure described earlier before being coated with the desired polymer. The coating procedures were vastly

different depending on the type of polymer used. Coating of the tubes with polyurea was accomplished with a two-step process. In the first step, a thick layer of polyurea is applied and in the second step the coating is machined down to achieve the desired thickness. The polyurea is prepared as described by Zhang, Liechti and Ravi-Chandar (2009). This involves the reaction of Isonate 143L (Dow Chemical) and Versalink P1000 (Air Products) in equivalent weight ratio of 1:4. Both chemicals are separately degassed at 30 ºC in a vacuum of ~ -25 in of Hg for 30 min while stirring continuously. These are then mixed in a 1:4 ratio by weight under vacuum for 2 min. Finally, the mixture of Isonate and Versalink is vented and slowly poured over the aluminum tube which is mounted on a slowly rotating Teflon mandrel. Because the mixture is extremely viscous, the mixture will not drip off the sample if the rotation speed is adjusted properly. The rotation of the mandrel is continued until the polyurea hardens completely (in about 5 minutes). The specimen is left to cure on the mandrel for 7 days. The mandrel is then placed in a lathe and the polyurea is gradually machined down to the desired thickness, typically in the range of 0.3 to 0.5 mm; a very sharp cutting tool, high rotating speed and small feed rates were required to achieve a good surface finish.

The polycarbonate coating was applied by machining a sleeve out of polycarbonate tube stock to dimensions of 16.25mm mean radius and ~0.5 mm wall thickness. A sliding fit was employed so that the sleeve could be fitted on the aluminum samples without the risk of damaging the very ductile metallic specimen. Although the polycarbonate is transparent in its stock form, once machined the surface finish becomes opaque, making it difficult to observe the electro-etched circular patterns on the metal surface through the coating, therefore hindering the ability to perform real time local strain measurements from the unwrapped images. In order to overcome this problem, a staggered circular pattern is painted onto the surface of the polycarbonate sleeve, by

means of a stainless steel mask. The mask is aligned with the sleeve in such a way that the row and column directions of the pattern match the hoop and axial strain directions in the aluminum specimen; the separation of the painted circles in the hoop and axial directions is 1.778 mm and 1.015 mm respectively. Figure 2.7 shows the painted polycarbonate sleeve. Figure 2.8 shows the quasi-static stress-strain curve for both polyurea and polycarbonate.

Once the samples and coatings are prepared, they are tested per the expanding tube experiment procedure described in Section 2.1.1.1, recording the events at a rate of 150,000 frames per second. The results of these tests are presented in Section 3.1.

2.1.1.3 Plane Strain Testing of Tube Specimens Using the Expanding Tube Experiment

From the expanding tube experiments on bare Al 6061-O samples performed by Zhang and Ravi-Chandar (2010), it was observed that short (18 mm) specimens presented a uniaxial stress state during electromagnetic inductive loading, and that longer (36 mm) samples showed a stress-state that migrated slightly towards a plane strain condition. This generated interest in investigating the behavior of Al 6061-O tubes under high strain rate, plane strain deformation. In order to research this, longer tube samples need to be expanded, which requires that a new electromagnetic coil be created that can accommodate them, and provide enough driving force to induce the same strain rates observed in the existing literature for shorter specimens (4,000 – 12,000 s^{-1}).

The added sample length translates into a larger mass that needs to be accelerated; therefore more energy needs to be applied to the sample to achieve the desired strain rates. In order to provide this extra energy, more wire-specimen interactions or a higher current flowing through the coil, that will create larger Lorentz forces are needed.

Increasing both is the ideal choice; however, these strategies bear negative consequences as well. A longer solenoid will have a higher inductance, slowing down the discharge pulse of the circuit; therefore the instantaneous driving force applied to the sample will be smaller, hindering the effectiveness of the coil. A larger current in the solenoid will cause the wire to heat up more; depending on the wire gauge used, the instantaneous temperature of the conductor might increase enough to melt the copper wire, destroying the component.

As a starting point to the plane strain condition investigation described above, a 23 turn, 112 mm long solenoid was developed for preliminary testing. The solenoid, shown in Figure 2.9, was wound from 8-gauge craft copper wire with a pitch of 5.1 mm and mounted onto a polycarbonate core. A 1.63 mm diameter rubber o-ring chord was used as a spacer, to maintain uniform separation between the coil turns. The entire assembly was then cast in epoxy and machined to the desired dimensions, with special interest on achieving an outer diameter of 30.4 mm. The following describes this procedure in detail.

The first step in the coil manufacturing process is the winding of the copper solenoid. An 8-gauge copper craft wire was selected in an effort to allow higher currents to eventually be used and to evaluate the advantages and disadvantages present in using a larger diameter conductor. In order to create the helical winding, a wrapping mandrel was developed. The tool consists of a machined steel bar, with grooves and rounded edges appropriately positioned to guide the wire during the winding process; the copper wire is threaded through the core of the mandrel and then bent 90º at the top of the tool to transition into the helical winding. The first turn is guided by the machined contour on the mandrel. The pitch of the helix is established by the user as the wrapping is being formed. After the solenoid turns are completed, the remaining wire is locked into place

by bending around a cavity in the mandrel. Finally, the mandrel is removed to unveil the final coil. Figure 2.10 shows the winding mandrel and wrapped coil; detailed drawings of the tool can be found in Appendix A.

Once the coil is ready, a polycarbonate core is inserted into its center, to give it support and rigidity, and a circular cross-section rubber o-ring chord is inserted between the coil turns, to achieve uniform spacing between these. The core is machined to allow the center wire of the coil to pass through it, as well as to allow for positioning of a Rogowski coil through the entire solenoid. The diameter of the core was selected to fit into the existing expanding tube experiment containment hardware (~Ø 22 mm). The o-ring chord diameter (Ø 1.63mm) was chosen to enforce the desired pitch of the helix (5.1 mm). Figure 2.11 shows the above procedure and Appendix A presents a detailed drawing of the core. The o-ring is tacked in place using quick-drying glue.

The above assembly is then cast in epoxy to fix the components in place permanently and provide electrical insulation between the wire turns, avoiding arcing during the high-voltage discharge.

Epoxy is a thermosetting polymer made from the reaction of two liquid components, an epoxide "resin" and a polyamine "hardener"; once mixed, a reaction takes place that allows the polymer to cure and harden into a completely solid form. There are different types of epoxy which have different cure times; some can cure in a matter of minutes while others can take hours. For solenoid making, it is extremely important to avoid bubbles in the epoxy, since these can initiate failure of the coil and lead to arcing between adjacent coil loops. Typically, solenoids for the expanding tube experiment were manufactured using a relatively fast-setting epoxy (30 min cure time); the two components were mixed together thoroughly and placed under vacuum for a few minutes to extract any bubbles of trapped air left over from the mixing process. Then the

mixture was poured into a mold and left to cure. For the 112 mm long solenoid however, the increased length of the coil requires a considerably larger volume of epoxy to encase the winding and allow for extra material to machine down to the desired dimensions. Epoxy is very viscous, making it hard for the gas bubbles to move to the surface of the liquid under vacuum. Experimentation showed that the time needed to properly de-gas the volume of fast-setting epoxy needed for the 112 mm long coil was longer than that available from the curing reaction. This yielded bubbles in the pour that expanded due to the exothermic nature of the chemical reaction in the epoxy, ruining the potting process. In order to avoid this, a slow-setting epoxy was used instead, made by mixing EpoxiCure Epoxy resin 20-8130-128, and EpoxiCure Epoxy hardener 20-8132-032 from the Buehler brand in a 5:1 ratio by weight.

In order to pour the epoxy in the desired shape, a vertical mold and molding technique was developed. Figure 2.12 shows an exploded view of the mold-coil assembly; detailed engineering drawings of the mold can be found in Appendix B. This tool consists of a base plate, a conical plug, 4 posts with stops, a cardboard cylinder and a top support plate with a locking bolt. The base plate consists of a machined aluminum plate with the following features:

- Four threaded through holes for the mold columns which establish the alignment of the mold end plates.
- A central cylindrical cavity to mold the support for the front end of the solenoid in the expanding tube containment assembly.
- A shallow, larger diameter cylindrical cavity that acts as an alignment edge for the cardboard cylinder which will act as the container for the epoxy.
- A mounting hole for the conical plug. The plug will seal the hole in the coil core for the Rogowski coil, preventing the resin from closing it up. Additionally, it

will act as a stop determining the height above the base plate where the coil will sit in the mold and also give lateral positioning to the solenoid with respect to the machined cylindrical cavities of the base plate.

- A set screw in the center of the plate is also present. This creates a guide for the machining of the solenoid on a lathe. The set screw will leave a cavity in the epoxy which serves as a concentric reference to the coil longitudinal axis, allowing the coil to be supported on the longitudinal axis of the component and eliminating vibrations from any imbalance in the resulting epoxy coating after the pour is complete.

When used, the entire surface of the base plate and plug exposed to the epoxy is coated with mold-release agent, to ensure an easy separation from the finished product. The cardboard cylinder is made from a 160 mm by 180 mm cardboard sheet, 0.55 mm thick. It is rolled into a tube with an outer diameter equal to that of the inner diameter of the shallow cavity of the base plate. An overlap will exist that is joined together with an all-purpose liquid glue. The entire cylinder is then covered with duct tape, to make it impermeable and placed in the shallow cavity of the base plate. The base plate-cardboard cylinder interface is then covered with glue and left to dry; this will act as a seal, preventing the epoxy from spilling out from under the cardboard container.

The four posts are made from ¼”-UNC galvanized steel threaded rod, cut to the desired length. These are screwed into place on the base plate, making sure they do not protrude on the bottom; they are then secured with hexagonal nuts on the top of the base plate. These will act as the guides for the mold, maintaining the top and base plates aligned. Another set of nuts is placed onto the posts, and will act as stops to hold the top plate at the correct height above the base plate.

The top plate consists of an aluminum plate with 4 through holes for the posts. Additionally a center hole exists that fits the polycarbonate core of the coil. There is an additional offset hole that overlaps the central one, intended to be the pour cavity. Finally, there is a threaded lateral hole that traverses one side of the plate from the edge to the central cavity. This is intended for a bolt that will secure the solenoid in place during the molding procedure.

In order to cover the coil in epoxy, the coil is suspended from the top plate and then lowered into the cardboard cylinder. The posts will run through the holes in the top plate, aligning it with the base plate. The coil orientation is such that the Rogowski coil cavity in the solenoid's polycarbonate core aligns with the conical plug in the base plate. Furthermore, the vertical position of the solenoid on the top plate is adjusted to ensure proper sealing of the Rogoswki coil cavity. The stops on the posts are then adjusted to ensure the vertical position of the coil. Once all of the above is achieved, the epoxy is prepared and poured into the cardboard cylinder and left to cure overnight.

For this particular coil, 110 ml of epoxy are needed. In order to obtain this volume of epoxy without any bubbles requires a specific procedure to be followed. It is assumed that the resin and hardener have similar densities, therefore recalling the 5:1 resin to hardener ratio by weight, the required volume of epoxy is divided into six parts; the volume of resin is then measured and weighed. Then the volume of hardener equivalent to one fifth of that mass is measured. Both components are then mixed together in a container using a wooden stick. The mixing process is carried out slowly to avoid introducing large amounts of air into the mixture. This operation is performed for about 2 minutes. After this, the mixture is transferred to a large surface area container. This will spread the mixture out, reducing the thickness, facilitating any trapped bubbles to rise out of the viscous liquid. Ideally the container should be large enough that the

height of the epoxy column does not exceed 4 mm. The mixture is then subjected to a vacuum of -25 in of Hg for 5-10 minutes. Once this has been completed, the mixture is removed from the vacuum chamber and inspected. If any bubbles are observed on the surface, they are burst by waving the flame from a butane torch carefully above the bubbles, making sure not to light the mixture on fire. This is repeated until no bubbles can be seen on the surface. Once this is completed, the epoxy is ready for pouring into the mould. To avoid introducing bubbles through the pouring process, the mold is held at an angle and the epoxy volume is slowly added through the pour hole in the top plate of the mold; as the liquid fills the cardboard cylinder, the orientation of the mold is brought slowly to vertical. A funnel can be used to facilitate the process. Once the epoxy has cured, the mold is disassembled and the set screw in the bottom plate is used to eject the coil-epoxy assembly. The cardboard cylinder is peeled off and the epoxy is then inspected for any severe flaws.

A lathe is required to machine the solenoid to its required dimensions shown in Appendix A. The outside diameter of the coil is chosen as 30.5 mm with a sliding fit tolerance to allow the same 30.5 diameter, 0.5 wall thickness tube samples to be used (in longer lengths and identical material properties). This however means that the actual thickness of epoxy covering the copper wire will be very thin, due to the combination of wire gauge and polycarbonate core diameter. Due to this, proper alignment of the coil in the lathe is extremely important, to ensure that a uniform epoxy coating will surround the copper coil. The back end of the coil is mounted on the lathe chuck, and the front of the coil is supported with a conical rotating support placed at the cavity left by the set screw in the base plate. This aligns the longitudinal axis of the coil with the longitudinal axis of the lathe, ensuring uniform machining. The actual machining procedure is straight forward, removing the excess epoxy with a cutting tool. High rotational speeds and slow

feed rates are recommended. Once this is completed, the exposed wire leads are covered with heat-shrink insulation and connectors are soldered onto the wire terminals.

For the plane strain experiments, the standard expanding tube experiment hardware was modified slightly to accommodate the longer coil. The standard containment enclosure for the expanding tube test is shown in Figure 2.13a and consists of two glass plates and a polycarbonate spacer mounted on bolts and secured with nuts. Additionally, a central cardboard liner is used to contain the specimens; this is necessary, to contain the sample fragments in case the specimen fractures. In order to accommodate the 112 mm coil, these nuts and bolts had to be replaced with longer lengths of ¼" UNC threaded galvanized steel bar and 4 nuts per bar. Additionally, a new cardboard ring was also fabricated to bridge the longer gap between glass plates. The modified setup for the containment hardware can be observed in Figure 2.13b. In addition to this, a new Rogowski coil was fabricated to be able to measure I_2 as discussed in Section 2.1.1.1, as the existing ones were too short to encircle the extended containment enclosure; Figure 2.14 shows the Rogowski coil. With this completed, the expanding tube experiment was ready to be performed with the 112 mm coil. The Al 6061-O samples were prepared identically to those in Section 2.1.1.2, with variation only in the tube lengths used and the thickness in some cases. The results for this experiment can be found in Section 3.2.

2.1.2 Spiral Coils

In the context of EML, spiral coils are utilized to apply unidirectional loadings on typically flat, plate-like specimens. These are ideal for this task, because the spiral arrangement allows for the current in the conductor to always flow in the same plane, therefore the out of plane magnetic field around the wire always acts in the same

direction, perpendicular to surface of the coil. The field contribution from each wire segment adds up, creating a uniform field perpendicular to the surface of the coil. This allows Lorentz force interaction to occur on a plane parallel to the coil surface, repelling a specimen placed over the coil in a direction perpendicular to the coil surface, assuming the coil is fixed in place. The spiral arrangement allows for tight packaging of the wire loops, allowing for a high level of specimen-conductor interaction per unit area (if the spiral pitch is kept small and the conductor has a small diameter), which can translate into the generation of strong Lorentz forces per unit area.

2.1.2.1 Design of an Experimental Method for Rapid Acceleration of Metallic Plates to High Velocities

Having the ability to rapidly accelerate a metallic plate to high velocities can open the door to a large amount of experimental research. This capability is particularly useful in simulating projectile impacts or blast loadings on flat plate specimens. A traditional projectile impact is characterized by a fast moving body interacting with a stationary object; in simulating this situation, a plate tends to be the stationary object. However, the same interaction can be achieved by accelerating the plate and maintaining the projectile stationary; as long as the relative velocity between the bodies is kept constant, the interaction between the parts should be the same. Depending on the actual geometry of the component impacting the plate, different stress-states can be induced. EML permits a specimen to be accelerated to very high speeds over a very small distance, allowing for a simple experimental setup to study this phenomenon, occupying relatively little space. Blast loading can also be simulated with EML, by fixing the edges of a plate sample and applying a high-speed loading on a portion of the specimen. Examples of this type of

research have been performed by Oliveira et al. (2005), Seth et al. (2004) and Takatsu et al. (1988).

The goal of the design was to create a proof-of-concept initial experimental setup that accelerated a small flat metallic plate to speeds in the range of 100 - 200 m/s using the experimental hardware available. Because of the nature of the loading, the main challenge was to manufacture a coil that would apply the desired loading on a flat plate, since the expanding tube solenoids can only provide a radial loading. A spiral coil configuration was selected as the appropriate driving element.

To simplify the initial effort, a small scale coil was designed. Sixteen-gauge square cross-section copper magnet wire was selected as the conductor. It was to be wound with uniform spacing into a 7 loop, 44 mm diameter Archimidean spiral. In order to maintain this uniform separation and facilitate winding, a 1.61 mm diameter rubber O-ring chord was to be wound with the copper wire. A polycarbonate plate, 76 mm by 101 mm, and 5.6 mm thick was selected as the base for the coil. After winding, the coil needs to be covered in epoxy to fix it in place, and provide electric insulation between the wire turns, analogous to the manufacturing procedure for the 112 mm coil in Section 2.1.1.3. Finally, once the epoxy cured, the assembly would be machined to ensure that the surface of the epoxy would be parallel to the plane onto which the spiral coil was wound.

In order to lock the spiral coil in place and provide a starting point for the coil winding process, a hole was drilled through the center of the polycarbonate plate that would allow the 16-gauge wire through, with minimum play. The copper wire was then threaded through this hole and bent 90º, providing an anchor for the wire; this bent wire would become one of the electrical leads for the spiral coil. Once the wire was locked in place, the winding process could be performed. The wire was wrapped on itself to form the smallest loop possible, without allowing the conductor to come into contact with itself

at any point. Additionally, this operation was performed in such a way to ensure that the same face of the square wire was always in contact with the polycarbonate base. The rubber O-ring chord was then inserted to provide the required separation between wire turns. Once this was performed, both the wire and O-ring were hand-wrapped in a spiral fashion to create the coil. When the necessary diameter was reached, the wire and O-ring were tensioned to ensure maximum compaction of the spiral and then tacked in place with quick-drying glue. The second coil lead was then threaded through a slit cut into the polycarbonate plate, locking it in place, and allowing both leads to be parallel to each other on the bottom of the plate and facing in the same direction. Finally, the leads were wrapped around the edge of the polycarbonate to make them point upward and facilitate posterior connection with the capacitor bank leads. Figure 2.15 shows photographs of the spiral coil.

The process of covering the winding assembly with epoxy was performed using a rectangular container made from thin Mylar film as the mold. This container was 80 mm x 105 mm x 25 mm. The coil assembly was placed in the mold suspended by two polycarbonate filler plates coated with mold-release agent. The goal of these plates was to create a cavity in the epoxy that allowed the bottom of the polycarbonate base plate to be exposed. The top and bottom surfaces of this plate define the plane onto which the coil is wound, and therefore can be used as a machining reference to ensure that the machined top surface of the epoxy-covered coil is parallel to the coil horizontal reference plane, allowing for a purely vertical driving force to be applied to the sample once placed on the coil. Figure 2.16 shows these filler plates and their location on the coil during molding.

Once the assembly was in position, 125 ml of epoxy were mixed per the method described in Section 2.1.1.3. Once prepared and bubble free, the epoxy was poured into

the mold while holding it at a slight angle, allowing all the air to be pushed out. In order to stop the assembly from shifting with respect to the filler plates or the mold itself, all components were tacked in place with quick-drying glue; the epoxy was left to cure overnight. Once the epoxy had cured completely, the Mylar mold was peeled off. The filler plates were then removed by exposing them with some coarse machining. Finally, using the exposed polycarbonate plate as a reference, the top surface of the coil was machined down such that it was parallel to the polycarbonate plate onto which the coil was wound and provided a 1 mm separation between the top of the highest point of the coil winding and the specimen when positioned on the epoxy covered assembly. Additional machining to make the finished coil shape more uniform was then performed, although it was not necessary for proper coil operation. It is desirable to minimize the separation between the plate specimen and the coil surface, to maximize the Lorentz force interactions and therefore the driving force applied to the specimen.

For this initial experimentation, square thin metallic plates were used. These were cut to different sizes using a shear. Details on the actual dimensions and material used can be seen in Section 3.3.

Finally, the expanding tube experiment had to be modified to fit the new spiral coil and be able to document the displacement of the flat plates and measure the sample velocities. The expanding tube hardware allows for a large voltage to be discharged through a coil very quickly and to record the events generated by this discharge with a high-speed camera. In the case of the plate acceleration experiment, the Cordin camera will photograph the specimen as it displaces with respect to the spiral coil. By measuring the separation of the specimen from its initial position in each image, and plotting this evolution against time, the speed at which the specimen is traveling can be calculated. In order to perform this, the containment assembly of the expanding tube experiment, shown

in Figure 2.13a, was replaced; the camera, flash and capacitor bank were maintained. Figure 2.18 shows the experimental setup used. The new containment assembly was designed to allow the flat plate to move upward freely for up to 216 mm, and then collide with a rigid metal plate to stop the motion.

In the expanding tube experiment, the containment assembly was secured in place by a hydraulic jack that clamped together two plates sitting on linear guides. This hydraulic jack was used to clamp the spiral coil in place by using three 216 mm long wooden columns and four 10 mm high wooden spacers, all 16 mm in diameter. As the only surfaces on the underside of the coil assembly parallel to the top surface were the channels left by the filler plates, the coil assembly was supported from these by sitting the entire assembly on the wooden spacers. Then, the columns were placed between the top plate of the hydraulic jack-holder assembly and the top of the spiral coil assembly and clamped in place by raising the hydraulic jack. A connector strip was used to link the coil leads to the capacitor bank circuit. Finally, two clear polycarbonate plates 9.25 mm thick were placed in front and behind the entire assembly and clamped in place, protecting the camera and other sensitive equipment from the specimen. A white background was employed to give contrast to the sample in the high speed images. Figure 2.19 shows this arrangement in detail. The sample was placed in such a way that its center would be aligned with the center of the coil and its edges were parallel and perpendicular to the focal plane of the camera.

Section 3.3 presents the results from the testing performed with the experimental setup described above.

Chapter 3: Experimental Results

As described earlier, three different experimental studies were performed for this work. The first one used the expanding tube experiment to investigate the dynamics of localization and fragmentation for polymer coated Al 6061-O tubes. The second looked to evaluate initial experimental setup designs for expanding tube testing of Al 6061-O samples in a plane strain condition. Finally, initial evaluation of experimental setup designs for flat plate acceleration to high velocities using electromagnetic inductive loading were performed. The results for these studies are presented in the following sections.

3.1 Effect of Applying a Polymer Coating on the Localization and Fragmentation of Al 6061-O Tubes

Experiments were performed on 13 aluminum 6061-O samples, 7 using polycarbonate sleeves and 6 with polyurea coatings. The polyurea coated specimens exhibited expansion speeds of 55 - 141.3 m/s or strain rates of ~3600 - 9200 s^{-1}. In contrast, for the same range of imposed load levels, the polycarbonate coated specimens experienced expansion of speeds of 64.6 - 90.4 m/s or strain rates of ~4200 - 5900 s^{-1}. Table 1 shows the experimental conditions for each of these tests. The results from Zhang and Ravi-Chandar (2010) for twelve uncoated Al 6061-O specimens are reported in Table 2, where the expansion speeds were in the range of 69 to 196 m/s or strain rates of ~4,000 – 12,000 s^{-1}.

Figures 3.1 and 3.2 present two selected sequences of images from expanding tube experiments Al 6061-O tubes with polyurea and polycarbonate coatings, respectively. We will refer to these as Al/PU and Al/PC specimens. All images contain two views of the sample; at the center of each image the direct view of the expanding

tube as seen in the direction of its longitudinal axis can be observed. Secondly, the reflection of the specimen surface in the conical mirror can be seen as an annular image around the specimen in the direct view. This second image can be unwrapped using the conical mirror projection mapping technique discussed in Chapter 2, allowing for quantitative interpretation of the behavior of the specimen surface, such as the tracking of real time local strain evolution on the sample. Figures 3.3 and 3.4 show the unwrapped image sequences corresponding to the samples seen in Figures 3.1 and 3.2, where the entire surface of the cylindrical samples can clearly be observed, albeit with some distortion arising from barreling of the cylindrical specimen. The evolutions of the hoop and axial strains, as well as the onset of fracture, can be clearly observed from these images.

As mentioned in Section 2.1.1.1, using the images from Figures 3.1-3.4, it is possible to determine the strain evolution of the samples in two different ways. Figures 3.5 and 3.6 show the evolution of average global strain and local strain for the tests presented in Figures 3.1-3.4.

Looking at the results displayed in Figures 3.1-3.6, it is possible to describe several stages in the expansion tests for both the polyurea and polycarbonate coated samples. These make evident the differences and similarities between the uses of both polymers to coat the Al 6061-O tubes. For the Al/PU specimens, the following is observed:

- The sample accelerates over the first 20 μs of the test, to a speed of 136.1 m/s.
- From 20 μs to ~47 μs the tube expands at a uniform speed of 136.1 m/s, corresponding to a strain rate of ~6700 s^{-1}. As observed by Zhang and Ravi-Chandar (2010) for the bare Al 6061-O tubes, the hoop strain increases to about 0.2; the specimen experiences a slight bulging or barreling due to the effect of

free boundaries at the ends as well as slight inhomogeneities in the electromagnetic interaction. This phenomenon starts to become evident visually after about 20μs.

- Due to the poor spatial resolution of the camera and the optical interference produced by the translucent polyurea coating, which is yellow and therefore darkens the reflected image of the tube surface, it is impossible to observe the localization bands in their early development directly. The first indication of their presence is the appearance of cracks on the specimen. These grow in a zig-zag manner, agreeing with the observations made by Zhang and Ravi-Chandar (2010).
- From 47 μs to 93 μs the specimen keeps expanding at a relatively constant strain rate of ~6700 s^{-1}. At 79.5 μs a spot becomes visible in the unwrapped image as indicated by the highlighted box corresponding to A-1 in Figure 3.3; this spot corresponds to the onset of localized deformation, when the hoop strain is about 0.5; the high magnification sequence **A** shows the evolution of this feature in time. Sequence B, also in Figure 3.3 shows the evolution of the first feature to produce arcing. The onset of this localized deformation is not clearly observed until 112.6 μs due to lack of clarity in the images and obstruction by a foreign object; however, it is suspected that it initiates at about the same time as the feature observed in sequence A.
- From 93 μs to 99 μs, the sample expansion begins to slow down, as the driving force begins to dwindle due to the increasing separation between the coil and the tube and the diminishing of the current pulse. As the tube expands, the bright spot just mentioned continues to increase in brightness. At 99.4 μs, a first crack appears at the point where this spot has been evolving; this event occurs at an average hoop strain of 0.57.

- It is evident in Figure 3.5 that up until the 99.4 μs mark, the local and global strains follow the same trend, differing only slightly in magnitude mainly as a result of the different methods of measuring both strains. The global strain is obtained from the measurement of the diameter of the sample in the direct view images (Figure 3.1). Because of the nature of these images, the most well-defined boundary to measure the diameter from is the inner diameter of the sample at one of the ends. The local strain however, is determined by measuring the evolution of the etched circle on the top surface of the aluminum tube (Figure 3.3) at the center of the sample. This location lies on the crest of the barrel shape exhibited by the sample during expansion, while the global strain is measured at the average point of this curved shape. Both these result in the measured local strain appearing slightly greater than the measured global strain.
- From 99 μs to 205 μs, the specimen continues to expand at an approximately constant speed of 40 m/s. Parts of the specimen are broken into fragments; the global and local strain time histories of Figure 3.5 clearly illustrate the trend – in the broken parts, where the first cracks appear, the Mott release wave begins to unload the sample, causing the fragments to stop straining; therefore, the local strain measure levels out at about 0.61. However, due to the inertia, the fragments continue moving radially outward at nearly the speed that they had at the instant of fracture. Therefore the global measurement of radius increases; however, this should not be interpreted incorrectly as strain in the specimen.
- Cracks begin to grow from ~112 μs until 152 μs; these are readily identified by the arcing at the crack tip that can be noted in the images. As observed by Zhang and Ravi-Chandar (2010), when the fractured surfaces separate and break electrical contact, the electric potential is still high and hence electric arcs jump

across the gap between fragments. These cracks propagate very quickly across the entire length of the tube in a time interval between one to three frames, providing a lower bound crack tip speed of about 900 m/s.

- *Post mortem* analysis of the sample shows the presence of well-defined localization bands on the inside of the sample. The density and definition of these bands is uniform throughout this surface.

For the Al/PC specimen, the following observations are recorded:

- The acceleration stage for this specimen extends from 0 to 18 μs. During this phase, the sample accelerates to a speed of 90.4 m/s. Analogous to the polyurea coated tubes, barreling is distinctly observed after 18 μs.
- From 18 μs to 52 μs the tube expands at a uniform speed of 90.4 m/s, corresponding to a constant strain rate of ~5928 s^{-1}. After 52 μs the expansion begins to slow down, reducing gradually in *speed until the expansion stops completely* at 91 μs. The average global strain at this point is 0.361; from the 91 μs mark until the 210 μs, when the camera stops recording the event, the diameter of the specimen remains essentially constant. Figure 3.6 shows clearly how the local strain and global strain behave in the same way for this test, with the differences in the magnitude being a reflection of the method used in estimating the strain. The barreling observed for this specimen was substantial, producing a large discrepancy between the global and local strains; the maximum local strain observed is 0.423.
- Finally, it is not possible to observe the formation of localizations on the surface of the sample in real time, as the polycarbonate is even more opaque than the polyurea, making discerning even the circular patterns etched onto the aluminum

samples almost impossible in the unwrapped images, much less distinguish localizations.

- *Post-mortem* analysis of the sample does not show the presence of localization bands on the inside of the sample. However, in specimen PC-4 the beginning stages of these bands are visible as we shall show later.

Zhang and Ravi-Chandar (2010) reported the evolution of deformation and failure in a 36 mm long bare Al 6061-O sample expanded by using a 15 kV discharge. From that account, certain key observations are summarized below for comparison to the polymer coated tubes:

- Initial acceleration occurred in the first 20 μs, reaching an expansion speed of 170 m/s, or equivalently, a strain rate of ~10^4 s^{-1}. Bulging was observed during expansion due to the effect of free boundaries.
- Localized deformations occurred simultaneously at many locations on the sample at a specific value of strain. Crack formation started from these localizations as indicated by real time and *post mortem* observations. Initial cracks appeared at 64.8 μs at a strain level of ~0.46.
- Arcing was observed as cracks propagated and fragments began to separate. Cracks propagated in a zig-zag manner from the center of the sample to the edges and many fragments were formed.
- Complete failure of the specimen occurred in this test, resulting in fragments that continued to move away with kinetic energy imparted by the electromagnetic inductive loading. The fragments travel radially outward with the velocity they possessed at the time of fragmentation.

– Finally, the observed behavior for the local and global strains matches the patterns seen in Figure 3.5 for the polyurea sample. Figure 3.7 shows the exact behavior of the uncoated aluminum sample.

Looking at the behavior of all three sample configurations, several similarities can be found. The acceleration phases of all three samples have approximately the same duration of 15-20 μs. However, in this period of time, the bare aluminum sample accelerated to 170 m/s, while the polyurea and polycarbonate coated tubes only achieve 136.1 m/s and 90.4 m/s, respectively, despite having equal or even greater driving force (15 kV for bare Al 6061-O and polyurea samples, and 16 kV for polycarbonate sample). The drop in expansion speed with coating can be attributed, at least partially, to the additional mass present in the composite specimens; by Newton's second law, if the same or a similar driving force is applied, the achieved acceleration will be inversely proportional to the mass variation of the samples. Bulging was also observed in all samples and is to be expected as they all have the same end boundary conditions. Localization and forming of cracks appeared at 64.8 μs in the bare aluminum sample, while in the polyurea sample localization did not appear until 99 μs into the test; while this represents a delay in time of the onset of localization, it does not indicate a change in the strain level at the onset of localization; this will be explored further in the following paragraphs. Even more interestingly, the polycarbonate coated sample exhibited no cracking of the aluminum at all. We will examine these quantitatively in terms of the strain levels at which these events appeared.

Figures 3.8, 3.9 and 3.10, show the average (global) hoop strain time histories of all the polyurea and polycarbonate coated samples tested in this work, as well as the 18 mm bare aluminum samples reported in Table 2. The point at which the specimen

exhibited cracking is marked by an X; the portion of the curves beyond this point is shown by a dashed line since this really does not correspond to strain, but merely radial expansion of the fragments.

- The bare Al 6061-O samples (Figure 3.8) fractured into fragments at strain levels in the range of 0.35 to 0.6, and then the fragments simply moved away radially with significant residual kinetic energy. The maximum expansion speed observed, corresponding to a charge of 14 kV was 196 m/s, or a strain rate of 12,800 s^{-1}. If the charge is low enough, such as 11.5 kV and 12 kV, the samples do not have enough energy to reach the required localization strain, and the specimens do not fail, but decelerate and stop deforming, after straining to about 0.2 to 0.35.
- The polyurea coated samples (Figure 3.9) exhibit a very similar response; at small charge levels, the specimens stop deforming after about 100 μs. As the loading intensity is increased, the Al/PU bilayer eventually reaches the strain threshold where the Al strain localizes and fails, with the fragments contained within the intact polyurea. However, the Al/PU bilayer appears to withstand a larger discharge (13 kV and 14 kV) without reaching failure than the bare Al specimen.
- Finally, for the polycarbonate coated samples (Figure 3.10), the maximum observed expansion speed achieved at the highest discharge voltage of 16 kV was 90.4 m/s corresponding to a strain rate of 5900 s^{-1}; the maximum strain reached for this case was 0.41. This level is below the strain threshold for strain localization and hence the Al/PC specimens did not exhibit any failure, either in the metal or in the polymer.

Before proceeding to analyze the response of the polymer coated aluminum tubes, we examine the details of the deformation in the tube to identify the strain evolution and the onset of strain localization. Optical images of the inner surface of the fragments from

three experiments (Al-2[1], PU-3 and PC-4) are shown in Figure 3.11; localization bands are clearly visible in all specimens. Note that the Al and Al/PU specimens are fragments, with arrested cracks visible as well, but the Al/PC specimen was cut and mounted in an inclined position in order to be able to observe the inner surface of the Al tube. Optical images of the assembled fragments of the Al and Al/PU specimen and the intact Al/PC specimen are shown in Figure 3.12. Clearly, the Al specimen has fragmented into a number of pieces (Figure 3.12a) and the Al/PU specimen has broken into five pieces (Figure 3.12c), but the Al/PC specimen (Figure 3.12b) is fully intact; neither the aluminum nor the polycarbonate exhibited any signs of failure. The electrolytically etched circles on the aluminum samples tested deform into ellipses (this can be observed in Figure 3.12 as well); measuring the length of the major and minor axes of these ellipses allows for an estimate of the maximum strains experienced by the samples as described in Chapter 2. *Post mortem* measurements of the ellipses were used to obtain the principal logarithmic strains, ϵ_1 and ϵ_2, where ϵ_1 corresponds to the hoop direction ($\epsilon_1 > \epsilon_2$) from the surfaces of a large number of recovered fragments (for the Al/PC specimens, the polycarbonate coating was cut and removed in order to observe and measure the etching on the surface of the aluminum). Figures 3.14 and 3.15 show these measurements for the polyurea and polycarbonate coated specimens respectively on a forming limit diagram. Figure 3.14 presents data from four tests with polyurea coating on the aluminum, including both 18 and 36 mm long tubes (strain rates are in the range of 3600 – 8900 s^{-1}). Figure 3.15 shows data from four tests as well, but corresponding to polycarbonate coating, although only for 18 mm long samples (strain rates in the range of 4200 – 5900 s^{-1}).

[1] The image of the Al-2 specimen was obtained from the actual test sample used by Zhang and Ravi-Chandar (2010). This was obtained directly from Dr. Ravi-Chandar, as it was in storage at the University of Texas at Austin.

In these figures, data from tubes expanded at different speeds are distinguished by different colors, blue corresponding to the slowest speeds and red to the highest. Additionally, strains measured from regions where no localization was evident under optical micrography are plotted as open symbols, while the strains measured from regions where a shear band was observed crossing an ellipse are plotted as filled symbols.

In addition to the circles, two lines are included. The dash-dot line corresponds to a state of uniaxial stress, with $\epsilon_1 = -2\epsilon_2$, while the dashed line represents the theoretical quasi-static forming limit for sheet materials, given by

$$\epsilon_1 = \frac{n}{1+\beta} \text{ and } \epsilon_2 = \frac{\beta n}{1+\beta} \text{ or } \epsilon_1 + \epsilon_2 = n \tag{3.1}$$

where ϵ_1 and ϵ_2 are the principal strains, $\beta = \epsilon_1/\epsilon_2$ is the ratio of biaxiality ($\beta = -0.5$ for sheet metals under uniaxial tension) and n is the hardening exponent from Eq. (2.16), as shown by Zhang and Ravi-Chandar (2010). There is considerable scatter in the data for the polyurea and polycarbonate coated samples, analogous to what was observed for the bare Al 6061-O samples in Table 2. This is caused by two reasons; firstly, the local measurements of strain are influenced by the curvature of the specimen to appear systematically larger, particularly the minor principal strains. Secondly, for strains measured on ellipses containing a shear band, the distortion provided by the shear band is neglected. The main observations from these forming limit diagrams (FLDs) are described below.

– In both Al/PU and Al/PC specimens, most of the measured data fall in the region $\epsilon_1 \geq -2\epsilon_2$, following the pattern observed by Zhang and Ravi-Chandar (2010) for the uncoated specimens (Figure 3.13). However, for the coated specimens, the data is not spread evenly around the uniaxial stress path; the data traces a steeper line than the $\epsilon_1 = -2\epsilon_2$ condition, implying that the stress state is migrating just

slightly from a uniaxial stress towards a plane strain condition ($\epsilon_2 = 0$). Furthermore, for the Al/PU coated tubes, the 36 mm samples seem to migrate more towards the plane strain condition than the 18 mm samples, as is expected from observing Figure 3.13. It can also be observed that the Al/PC samples (all 18 mm in length) exhibit a larger shift towards the plane strain condition than the polyurea coated specimen of the same length. This indicates that the polycarbonate coating seems to have a greater influence on the stress state of the aluminum than the polyurea.

- For the polyurea coated samples, the expanding velocities are in the range of 55 – 136.1 m/s. All specimens, including the ones that stopped deforming as a result of low loading levels, show shear bands throughout their surface.
- For the polycarbonate covered samples, the expanding velocities are in the range of 64.6 – 90.4 m/s. No localizations were observed in specimens PC-1, PC-2 and PC-3. However, the sample PC-4 showed very faint shear bands throughout its internal surface; the average local strains attained in this specimen correspond to an average hoop strain of 0.50 and an average longitudinal strain of -0.24. The other specimens exhibit lower average local strains and do not show localization bands. It is worth noting that specimen PC-3, with a higher expansion speed of 90.4 m/s, exhibits no shear localization but has very similar average strains (average hoop strain = 0.47, average longitudinal strain = -0.21) to the specimen PC-4, suggesting that the formation of distinguishable shear bands occurs in the range of 0.47 to 0.50 average hoop strain and -0.21 to -0.24 average longitudinal strain; these appear to be slightly above the quasi-static forming limit for the Al 6061-O.

- Additionally it can be noted that for the polyurea covered samples, most measured circles demonstrate strain levels above or close to the forming limit for the material. Since all the samples show clear shear localization, and are located immediately above the predicted forming limit, this is indicative that the polyurea coating does not affect the quasi-static forming limit for the aluminum under this forming operation, and therefore the material behaves almost identically to the bare aluminum samples in Figure 3.13.
- Finally, from the data of the polycarbonate coated samples, the forming limit does not seem to agree with the quasi-static forming limit predicted for the uncoated aluminum specimens. It is observed that there are a significant number of open symbols above the quasi-static forming limit dash-dot line in Figure 3.15. This implies that the forming limit seems to have shifted upward, allowing for a larger strain level without the onset of localization. From the experimental data shown here it is difficult to determine this new forming limit exactly; however, an upward shift of the quasi-static limit by 6% strain would seem to fit better to the observed results. This may be caused by a modification of the stress state of the aluminum caused by a pressure loading applied by the polymer on the top surface of the tube and needs to be explored further.

From Table 1, and Figures 3.14 and 3.15, it is evident that the strain levels achieved by the Al/PU samples were considerably larger than those experienced by the Al/PC, despite the fact that the charging voltages used in the tests were in the same range (13-16 kV). It can be inferred that adding a coating reduces the strain the aluminum can experience, since the acceleration of the additional mass will consume some of the energy that would otherwise be used in straining the metal. However, it can also be noted that the actual added mass from the coatings is relatively similar for both polyurea and

polycarbonate, and the vast difference in the strain levels observed (25% difference in maximum hoop strain) is due to the fact that plastically deforming the polycarbonate requires a much larger amount of energy than that needed to elastically deform the polyurea, as is expected from the material properties. This higher resistance also accounts for the larger effect on the stress state of the aluminum as described before, as it creates a larger pressure on the surface of the tubes than the polyurea coating would.

Finally, from the previous analysis, it is evident that no references are made to the Al/PC samples PC-5, PC-6 and PC-7, which correspond to the 36 mm long specimens tested. This omission exists because these specimens exhibit a phenomenon that yields them unusable for the previously performed analysis. Initially, the samples behave in the same manner as the 18 mm long tubes; however, the post-mortem analysis of these reveals the presence of lengthwise banding, which resembles wrinkling. These bands make it impossible to evaluate the level of localization of the specimens, and therefore makes extracting useful data about the behavior of the aluminum, other than the expanding speed and global strain, also impossible. Figure 3.16 shows *post mortem* views of these samples and clearly illustrates the bands described above (third column). The exact cause for the formation of these bands is unknown; an idea attributes them to buckling under a compressive external pressure, caused by the elastic relaxation of the polycarbonate coating, however, there is no evidence yet to support this.

The bands are only found in the 36 mm specimens, suggesting that their formation is aspect ratio dependent. The bare aluminum and polyurea coated 36 mm specimens do not exhibit this behavior; Figure 3.17 shows a comparison between two fractured specimens: a localized polyurea coated 36 mm specimen and a polycarbonate coated tube. It is clearly visible that the Al/PU specimen localized as expected from the observations made by Zhang and Ravi-Chandar (2010) of bare aluminum samples; shear

bands are clearly observed throughout the surface. The Al/PC sample shows clear longitudinal banding throughout the entire surface and no distinguishable presence of shear localization bands. It is also worth noting that as seen in Figure 3.16, several samples fractured, in contrast to the 18 mm samples, where in all cases the samples remained whole. It is possible that the failures were triggered by imperfections in the aluminum specimens or in the polycarbonate coatings or by the longitudinal bands themselves; however it is impossible to determine the exact mechanism of failure for these samples, as the presence of the longitudinal bands make observations about the shear localization unattainable.

3.2 Plane Strain Expanding Tube Testing of Al 6061-O Samples

As described in Section 2.1.1.2, in order to perform plane strain expanding tube experiments, it is necessary to test longer specimens than previously done (L > 36 mm) [2]; these longer specimens tend to experience a stress state that migrates from a uniaxial tension condition towards plane strain as observed by Zhang and Ravi-Chandar (2010). The actual required length to achieve a pure plane strain condition is unknown; it was the objective of the experimentation performed here to better define the requirements for inducing this condition on Al 6061-O tubes and to generate understanding of the performance of the experimental setup developed for this type of testing.

The first step in the experimentation process was to evaluate the performance of the newly fabricated 112 mm solenoid described in Section 2.1.1.3. Particular interest was placed on examining the pulse shape generated by the coil in contrast to that of existing shorter ones. Figure 3.18 shows a comparison between the Rogowski coil

[2] This length is specific for the expanding tube experimental setup available.

measurements of the current through the entire solenoid for a 36 mm solenoid and the 112 mm coil, per the expanding tube experiment configuration described in Section 2.1.1.1. Both were subjected to voltage discharges of 2 and 3 kV. Rogowski coil output is given by

$$V = K\frac{dI_T}{dt} \tag{3.2}$$

where V is the voltage output of the sensor, K is a scaling constant defined by the construction of the instrument and dI_T/dt is the variation in $nI_1 + I_2$, where I_1 is the current through the solenoid, n is the number of turns in the solenoid and I_2 is the current in the specimen. For the data presented in Figure 3.18, no samples were present on the coils, therefore dI_T/dt corresponded only to the variation with time of nI_1 ($n = 12$ and 23 for the 36 mm and 112 mm coils respectively). Dividing the signal in Figure 3.18 by the corresponding n for each coil allows for Figure 3.19 to be generated. This figure displays $K\frac{dI_1}{dt}$ as a function of time, which allows for a better interpretation of the behavior of the current flowing through the conductor in each solenoid. It is evident from Figure 3.19 that the variation in current through the solenoid conductor is only slightly greater in the 36 mm than in the 112 mm. From the above observations, it can be concluded that the 112 mm coil behaves relatively similar to the shorter 36 mm coil at low voltages. The differences are not large enough, or particularly negative, as to affect the expanding ring experiment; however, it is possible that at higher voltage discharges, larger variations may appear. Larger voltage evaluations of the 112 mm coil were impeded by the hardware available for this experiment, as the voltage amplitude of the Rogowski coil signal would exceed the range for the oscilloscope available to measure it.

In an attempt to achieve a plane strain condition in bare Al 6061-O tubes, several specimens in various lengths were manufactured from the same stock used for the

specimens used in the experiments in Section 3.1 and prepared identically. The internal diameter was kept constant at 30.5 mm with wall thicknesses of 0.35 and 0.5 mm; three lengths were used, 50, 70 and 90 mm, and all specimens were electro-etched with a circular pattern on their surface. Five tests were performed using discharge voltages in the range of 8 – 16 kV. Expansion speeds between 15.5 – 90.1 m/s were experienced, corresponding to strain rates of ~1000 - 5900 s^{-1}. Table 3 shows the experimental conditions for each of these tests. The goal of using multiple lengths was to quantify the effect of longer specimens on migration of the stress state from a uniaxial condition to plane strain. The discharge voltage range was implemented to generate an understanding of the energy levels needed to achieve the same strain rates as experienced in other expanding tube experiments, such as those analyzed in Section 3.1 (~3600 - 9200 s^{-1}). Also, it was of interest to examine the strain levels that could be achieved in the specimens with this experimental setup.

Figure 3.20 presents a selected sequence of images from one of the tests performed (PS-5). Analogous to Figures 3.1 and 3.2, these images present two views: a direct view at the center of each image, showing the expansion of the specimens as seen in line with the longitudinal axis of the sample, and a reflection of a portion of the specimen in the conical mirror placed behind the sample; this reflection is observed as an annular image surrounding the sample in the direct view image. In the traditional expanding tube tests performed by Zhang and Ravi-Chandar (2010) on bare Al 6061-O tubes, this reflection was unwrapped as discussed in Chapter 2, to allow the evolution of the local strain on the surface of the sample to be determined; this was also performed in the analysis in Section 3.1. The objective of this experiment, however, is to validate the initial setup of the modified expanding ring procedure for plane strain testing, which looks to quantify how the strain experienced by the specimen approaches a plane strain

condition. In order to do this, only *post mortem* strain measurements of the sample are needed, therefore the unwrapping of the reflected images of the sample surface was not performed. Additionally, it must be mentioned that because of the added length of the specimens used in these tests, and the physical dimensions of the conical mirror available, only a partial section of the specimen surface can be observed in the reflection in the conical mirror, which can omit important information about the localization and fragmentation process of the samples. For future detailed studies of the plane strain deformation of Al 6061-O tube samples, a larger mirror must be employed that can reflect the entire sample surface.

As described in Chapter 2, the images in Figure 3.20 can easily be used to determine the average global hoop strain evolution of the specimen per Eq. (2.14). Figure 3.21shows this strain evolution for the PS-5 specimen. Looking at Figures 3.20 and 3.21, it is possible to describe several stages and phenomena present in the expansion of this tube, which allows for a comparison between the sample's behavior and that of shorter specimens as described by Zhang and Ravi-Chandar (2010). The following is observed:

- The sample accelerates over the first 13 μs of the test to a speed of 90.1 m/s, expanding uniformly.
- At 20 μs, the sample begins to exhibit flaring, where the edges of the specimen expand faster than the main body, due to the interactions of the ends with the Lorentz forces. It is observed that the main body of the specimen slows down and maintains a linear expansion at 44.5 m/s until 73 μs, achieving a strain of 0.21. This is equivalent to a strain rate of ~2900 s^{-1}. The edge continues to expand at 90.1 m/s until 59 μs. By this point in time the edge has strained to 0.26; the

corresponding strain rate is ~5900 s^{-1}. From 59 μs to 73 μs, the edge experiences a gradual decrease in speed.

- Similar to what is described in Section 3.1, because of the poor spatial resolution of the camera, even though no coating is present, it is impossible to distinguish the development of localization bands on the sample. The first indication of localization is the appearance of cracks. In this case, two cracks appear simultaneously at 73 μs. Both are found at the sample edges; one can be seen in the direct image on the lower-left quadrant of the specimen, and the other is visible on the reflection of the sample surface, again in the lower-left quadrant of the image. Both originate at the edge, propagating inward. The strain level at this point is 0.31.
- From 73 μs to 150 μs, the body of the tube stops expanding, maintaining a constant strain of 0.21. The edge continues to expand, slowing down gradually to a speed of 17.5 m/s at 152 μs. At this point, the strain achieved is 0.41. During this period of time, the existing cracks continue to grow and multiple others appear as well and grow, generating a petal like geometry on both ends of the sample. At 112 μs, arcing is observed at one of the cracks.
- From 152 μs to 204 μs, the body of the sample begins to re-expand, at a constant speed of 17.5 m/s; the edge also expands constantly at this speed. The body of the specimen achieves a strain of 0.26, while the edge reaches 0.44. The re-expansion of the body is caused by the inertia present in the formed petals. These expand outward at a high speed and eventually drag the rest of the sample along. Additionally, at 152 μs, a large arcing is visible on the lower-right of the image. This phenomenon grows as time progresses and triggers a crack propagation that will split the specimen in half almost completely, as shown in Figure 3.22.

Figure 3.22 also shows an interesting characteristic present in all of the experiments performed with the 112 mm solenoid. It can be clearly observed that the profile of the main body of the specimen exhibits a sinusoidal nature. The local axial strain was measured *post mortem* on a lengthwise row of consecutive circles on the specimen surface, visible in Figure 3.22a. The strain values were then plotted as a function of position along the sample, generating Figure 3.23. It is evident that there is a sinusoidal profile to the sample, where the variation in axial strain between peaks and troughs oscillates between ~ -0.03 – -0.05. The cause for this oscillation is unknown, but it has been hypothesized that it may be a problem similar to a beam on elastic foundation, generated by the interaction of the Lorentz forces and the sample. More in-depth analysis needs to be performed to find a suitable explanation.

Section 3.1 described the deformation and failure in a 36 mm long bare Al 6061-O sample expanded by using a 15 kV discharge, as observed by Zhang and Ravi-Chandar (2010), stating the following:

- Initial acceleration occurred in the first 20 μs, reaching an expansion speed of 170 m/s, or equivalently, a strain rate of ~10^4 s^{-1}. Bulging was observed during expansion due to the effect of free boundaries.
- Localized deformations occurred simultaneously at many locations on the sample at a specific value of strain. Crack formation started from these localizations as indicated by real time and *post mortem* observations. Initial cracks appeared at 64.8 μs at a strain level of ~0.46.
- Arcing was observed as cracks propagated and fragments began to separate. Cracks propagated in a zig-zag manner from the center of the sample to the edges and many fragments were formed.

- Complete failure of the specimen occurred in this test, resulting in fragments that continued to move away with kinetic energy imparted by the electromagnetic inductive loading. The fragments travel radially outward with the velocity they possessed at the time of fragmentation.
- Finally, the observed behavior for the local and global strains followed Figure 3.7.

Comparing this with the behavior of the PS-5 sample, it is evident that similarities exist, but mostly the two specimens behave differently. The acceleration phase in both cases is essentially identical, in that it lasts between 13 and 20 μs. However, the speeds achieved are quite different. The 36 mm sample achieved an expansion velocity of 170 m/s with a discharge of 15 kV, while the 90 mm sample only experienced a speed of 90.1 m/s with a discharge of 16 kV. This is expected as the energy levels input into the specimens were similar, but the mass of the 90 mm tube was more than twice that of the 36 mm sample, therefore, the possible maximum acceleration for the 90 mm specimen under these conditions was considerably lower according to Newton's Second Law. It was also observed that the 36 mm tubes showed signs of bulging due to the effect of free ends. The 90 mm sample showed flaring, also indicative of interaction between the free ends of the sample and the Lorentz forces. In the case of bulging, the sample is longer than the area of application of the Lorentz forces, therefore the ends of the specimen do not get as big of a force applied on them relative to those received by the main body of the tube; this translates into a slower expansion speed, causing the barreling shape. Flaring occurs in the opposite case, when the sample is too short for the coil; in this case, the free ends are acted on by the same Lorentz forces as the main body of the tube. However, they are free, thus they have less resistance to motion as the rest of the specimen, expanding more rapidly, causing the characteristic shape.

Continuing the comparison, the 36 mm specimen presented its initial crack at a strain of ~0.46, while the 90 mm tube showed its initial crack at a strain of ~0.31, considerably lower. Arcing and failure were observed in both cases; the failure of the 36 mm sample yielded many fragments, while the 90 mm specimen did not produce any. Additionally, the propagation of the cracks in both specimens followed a zig-zag path. Furthermore, the average global hoop strain of the 36 mm sample matched that of the edge of the 90 mm sample, but not that of the main body. It is clear that the 15 kV discharge induced a much more violent expansion in the 36 mm specimen than that observed for the 90 mm. This is expected as described above due to the added mass in the longer sample and the comparable energy levels present in both tests.

Figure 3.24 shows the variation of average global hoop strain for all the samples in Table 3. As mentioned in Section 3.1, Figure 3.8 presents the same data for the 18 mm long bare Al 6061-O samples tested by Zhang and Ravi-Chandar (2010). It can be observed that the general trends observed are the same. For example, in both cases, the lower energy tests, that is the ones with discharge voltages that do not cause failure of the specimen, accelerate the samples at a constant speed and then hit a plateau, where the strain level remains constant for the remainder of the test. The expansion velocities observed in Figure 3.8 where this occurs are in the range of 69 to 90.5 m/s, while for Figure 3.24, this range is 15.5 – 45.4 m/s (ignoring the 90 mm test). The other type of behavior observed is that of a specimen that exhibits fracture. In this situation, the samples accelerate and expand at a constant speed, then localize and fracture; at this point, the expansion speed is decreased and the specimen continues to expand under rigid body motion at a lower speed. In the case of the 18 mm specimens, initial fracture occurs at strain levels of ~0.35 – 0.5. In the longer specimens, this occurs as early as strains of ~0.2. From the expansion speeds and strain levels observed in Figure 3.24, it seems that

tests need to be performed at higher discharge voltages, to better compare the behavior of the different length specimens when expanded with the 112 mm coil.

Figure 3.25 presents *post mortem* images of all the specimens expanded with the 112 mm solenoid. It is quite clear that in all cases, flaring was observed, suggesting that all samples were too short for the coil. Additionally, all specimens exhibit the sinusoidal profile on their walls, pointing towards a systematic cause. It can also be observed in these images that no shear localization bands are visible in any of the samples. However, longitudinal banding is present in all the tubes expanded with a voltage higher than 8 kV. These bands resemble those observed in the 36 mm long polycarbonate covered tubes in Section 3.1. The bands are very distinct and become more defined as the discharge voltages and strain levels observed increase.

Finally, *post mortem* measurements of the local hoop and axial strains of the specimens were performed to illustrate the stress state of the specimens. Figure 3.26 displays this data in a dynamic forming limit diagram. Due to the presence of the longitudinal banding described above, no assessment of the level of localization of the specimens could to be performed, therefore in this figure, in contrast to Figures 3.13, 3.14 and 3.15, all circles are filled and this does **not** signify localization. Figure 3.26 shows scatter, particularly in the shorter specimens. As the tubes become longer, the scatter is reduced to a narrower band. It is quite evident that as the length of the samples is increased, their stress state migrates more towards a plain strain condition. The *dash-dot line* in the figure represents the uniaxial path $\epsilon_1 = -2\epsilon_2$, observed in the 18 mm long specimens described in previous sections. The red *dash-dot-dot line* represents the path $\epsilon_1 = -3.4\epsilon_2$, which seems to be the average path experienced by the 90 mm tube. A significant migration of the stress state towards a plane strain condition is evident; however, it is also clear that longer samples are needed to approach this desired condition

even more closely. The FLD also illustrates that the strain levels observed in the specimens are below the quasi-static forming limit of the material. However, failure was observed in both the 70 mm and 90 mm samples, as cracks propagated from the edges of the tubes, which exhibited flaring, although no localization bands were distinguishable. Heavy longitudinal banding was also observed as shown in Figure 3.25. It is possible that the presence of these bands facilitated the formation of the cracks that triggered the failure in the specimens. An in depth study must be performed to better understand these phenomena, as they seem to have a big role in the plane strain expansion of Al 6061-O tubes.

3.3 Design of an Experimental Method for Rapid Acceleration of Metallic Plates to High Linear Velocities

The goal of the experimentation performed here was to evaluate the proof-of-concept experimental setup described in section 2.1.2.1. This design looked to accelerate a flat metallic plate to speeds in the range of 100 - 200 m/s. Several modifications were made to the expanding tube test equipment, including the replacement of the solenoid used to apply the radial loading on the tube samples with a prototype flat spiral coil that would apply a unidirectional driving force to the plate specimens. In order to validate these modifications, three small scale tests were performed: the first two used small 30 x 30 mm plate specimens of different materials at a relatively low voltage, aiming to validate the effectiveness of the spiral coil in a safe manner; the third test used a larger 65 x 65 mm plate and attempted to better characterize the behavior of the specimen itself under the electromagnetic inductive loading provided by the spiral coil Table 4 shows the experimental conditions for each of these tests. Speeds in the range of 45.3-251 m/s were obtained at a constant discharge voltage of 8 kV for all tests.

All samples were cut from sheet stock using a shear. The larger aluminum specimen was partially electro-etched with the same pattern of circles and method used in Chapter 2 on the tube specimens. A voltage of 8 kV was chosen to provide a strong enough loading to the plates to ensure liftoff, but low enough to reduce the possibility of a violent mishap, as the spiral coil design had never been used before.

Figure 3.27, 3.28 and 3.29 show a selected sequence of images from the three tests performed (FS-1, FS-2 and FS-3). These images present a direct view of the event and illustrate clearly the variation with time of the vertical displacement of the specimens. It can be observed at first glance that the focal plane of the image is not exactly parallel with the plane on which the specimens displace. This discrepancy will cause a distortion in the measured displacement of the samples on the images, compared to the actual quantity; however, because the quantitative analysis performed here is used only as a method for proving the experimental concept in question, the error induced by this misalignment can be neglected. In a finalized design of this experimental technique for detailed research purposes, this issue would need to be resolved.

By tracking the displacement of a representative point on the samples as a function of time, the speed of the plates can be calculated from the high-speed images. By fitting the displacement-time history for a specimen with a curve and finding the derivative of the corresponding equation, the velocity of the plate can be calculated as a function of time. Figure 3.30 shows the variation of the vertical displacement for all three tests. In order to obtain the quoted values for the expansion speeds, the points in the interval between 15 and 50 μs for each test were fitted with a line; the slope of this line is the quoted speed and corresponds to the initial speed observed. It was observed that the displacement-time histories experienced a slight deceleration as time progressed; therefore an attempt was made to quantify this behavior. Figure 3.31 shows the

displacement-time histories for tests FC-1 and FC-3 fitted using a second order polynomial. It is clear that this approximation fits the displacement of the specimens quite well and might have some usefulness in future modeling of the experiment, although this is not within the objectives of the current investigation.

Looking closely at Figures 3.27, 3.28 and 3.29, it can be observed that there are some similarities between the behaviors of the specimens, although mostly they are very different. The following is observed:

All three samples remain immobile for the first 13.2 μs of the test and then accelerate to their initial speed over a period of 6 μs. This initial speed is then maintained throughout the test, experiencing only a very slight decrease as time progresses. All tests were conducted with the same discharge voltage, ensuring that the energy available to accelerate each plate was always the same. However, a very large range of initial speeds was observed. Additionally, the physical behavior of the specimens during their displacement also varied considerably; the geometrical and material particulars are responsible for these phenomena.

Aluminum is a better electrical conductor than steel and has a lower density as well; on the other hand, steel has a higher elastic modulus than the aluminum. These characteristics account for the differences in behavior observed in the specimens.

From Figure 3.27, it can be observed that specimen FC-1 was deformed into a petal shape from the very beginning of its acceleration. This deformation evolved from 19.8 to 59.3 μs, when the deformed shape remained constant. This morphing of the plate was caused by inhomogeneities in the field of the spiral coil, the relative size of the sample with respect to the coil and to the bending stiffness of the plate. Since the specimen was smaller than the coil diameter, each edge could experience a different loading depending on where on the coil they were located, as the field generated by the

coil is not perfectly uniform. Additionally, the size of the specimen is comparable to the center of the spiral coil, where a void is present, due to the nature of the winding process. At this point, the Lorentz force interaction would be lower than in the surrounding areas. The sum of these characteristics would cause an erratic strong loading on the edges of the specimen and a smaller one in the center. This would accelerate the edges faster than the center and possibly affect each edge differently.

In contrast, Figure 3.28 shows the response of a steel plate to the same issues. In this case specimen FC-2 was almost four times as heavy as specimen FC-1. This would suggest that, according to Newton's Second Law, if the same force was applied to FC-2 than experienced by FC-1, it would be accelerated to a velocity four times smaller than FC-1. However, the Lorentz forces applied to the specimen are affected by how good of a conductor the specimen material is, since this will affect the electromagnetic induction in the specimen. As steel is not as good a conductor as aluminum, it is expected that the FC-2 plate would experience lower Lorentz forces than FC-1; this combined with the added weight would suggest that this sample would be accelerated to less than a quarter of the velocity reached by FC-1 or less than 62.75 m/s, which is what is observed from the experimental results. It is also observed that the steel plate remains almost un-deformed during the test, compared to what was observed in FC-1. This can be attributed to the thicker specimen and the larger elastic modulus of steel compared to aluminum. These factors increase the bending stiffness of the specimen; considering that the Lorentz forces experienced by the steel plate are also lower than those experienced by the aluminum plate, it is expected that the deformation induced into steel plate would be less than for the aluminum one.

Figure 3.29 presents the behavior of an aluminum sample larger than the actual coil. The mass of this plate is more than four times greater than that of FC-1. However,

because it covers the entire spiral coil, it will have Lorentz force interaction over a greater area as well. If we assume that the same force is applied per unit area on each portion of the specimen covering the coil as experienced by FC-1, then we can expect a larger total force to be applied to the plate, compensating for the increase in mass somewhat. In this case the increase in mass that will cause a penalty towards the velocity the sample can achieve will be the mass of the specimen that exceeds the diameter of the coil; this penalty will lower the initial speed obtained by the plate, as is observed in the experiment. This is reasoning is also supported by the deformation observed in the plate. The FC-3 specimen deforms in the form of a bulge or dome matching the diameter of the coil and located exactly over it. The bulge grows quickly and does not appear to affect the portion of the sample not in contact with the coil until about 65.6 μs, when wrinkling is exhibited at the edges of the specimen as the bulging plate wants to pull these upwards. The behavior of the plate is similar to that of a *draping* cloth. It is not until the late stages of the test that the entire plate has become airborne.

Figure 3.32 presents *post mortem* images of the three plate specimens, illustrating the very different behaviors of each specimen described above. It must be mentioned that after the events captured by the high-speed images, the specimens collided with a metallic plate that stopped their motion, causing some additional deformation, as seen in Figure 3.32a. It is also worth mentioning that both aluminum specimens exhibit *draping* characteristics.

Post mortem local strain measurements were performed on specimen FC-3. These are presented in Figure 3.33 and were measured on two areas of the specimen, at the center of the plate and at an area ~15 mm from one of the edges. The 11 and 22 directions were chosen as the directions of two adjacent edges of the plate. It can be observed that the strains experienced by the specimen were very small, in the range of

~0.004 – 0.05. Also it is noted that the strains in the center of the plate were larger than in the second location. Additionally, the strains appear to follow the bi-axial path $\epsilon_{11} = \epsilon_{22}$.

From the above results, it is clear that the experimental concept designed fulfilled all of its requirements, by accelerating metallic plates successfully to speeds greater than 200 m/s. It is worth noting however, that after the three tests described here, the epoxy coating of the spiral coil assembly began to crack and fracture. It is believed that the support system employed allowed the assembly to bend in response to the Lorentz forces experienced, stressing the epoxy and causing it to crack and later fracture. Future designs of the coil require attention to this issue, and will probably call for a redesign of the system employed to secure the coil in place.

Chapter 4: Conclusions and Recommendations

Possessing a grasp on the particularities of high strain rate localization and fragmentation behavior of metals is critical for activities like industrial forming operations, armor plating systems development, etc. In order to comprehend this behavior, research needs to be performed on the subject, which inevitably requires the investigators to replicate the high strain rate behavior of the material in a controlled manner; this can be a challenge. Many experimental methods have been developed to achieve this, including some that utilize electromagnetic inductive loading as a means to induce the required strain rates on particular specimens. In these cases, Lorentz force interaction between the current in a conductor, typically a helical or spiral coil, and an induced current in the metallic specimen results in a very rapid acceleration of the specimen, resulting in high strain rates under certain configurations. It was the aim of the present study to utilize electromagnetic inductive loading techniques to undertake three tasks:

- Analyze, using the expanding tube experiment, the effect on the localization and fragmentation of Al 6061-O tubes of applying a uniform polymer coating.
- Design an experimental setup to test the localization and fragmentation properties of Al 6061-O in a plane strain condition, based on the expanding tube experiment.
- Design an experimental setup to accelerate flat metallic plates to high velocities using electromagnetic inductive loading techniques.

The following sections present conclusions and recommendations extracted from the results obtained from the above tasks.

4.1 Effect of Applying a Polymer Coating on the Localization and Fragmentation of Al 6061-O Tubes

Details of the test arrangement and sample configuration are presented in Section 2.1.1.1 and 2.1.1.2. Thirteen tests were performed, seven using polycarbonate sleeves and six with polyurea coatings. The results from these were compared to data obtained by Zhang and Ravi-Chandar (2010) for uncoated Al 6061-O tubes, yielding the following conclusions:

- Strain evolution patterns are similar for all specimens, regardless of coating. However, the strain levels attained for a particular discharge voltage used do vary; the bare aluminum specimens achieve the highest strain levels, followed by the polyurea coated tubes and finishing with the polycarbonate coated ones.
- All specimens exhibit shear localization by a strain level of 0.6. The bare aluminum and polyurea coated tubes fail according to the quasi-static forming limit of the material and localize as early as a strain of 0.35. The polycarbonate coated specimens however seem to fail at higher strain levels, appearing to shift the forming limit of the material upwards by about 6%.
- The stress state of the polymer coated specimens appears to migrate slightly from a uniaxial condition to a plane strain one, compared to the uncoated specimens. This may be caused by a modification of the stress state of the aluminum caused by a pressure loading applied by the polymer on the top surface of the tube. The migration of the polycarbonate coated specimens is larger than that of the polyurea coated ones, suggesting that the polycarbonate coating has a greater influence on the stress state of the aluminum than the polyurea.

- Adding a coating reduces the strain the aluminum can experience, since the acceleration of the additional mass will consume some of the energy that would otherwise be used in straining the metal.
- Plastically deforming the polycarbonate coating requires a much larger amount of energy than that needed to elastically deform the polyurea, as is expected from the material properties, resulting in slower expansion speeds and lower strain levels, as more of the driving force is dissipated by the coating.
- The combination of longer tubes (36 mm) and polycarbonate coating produces longitudinal bands in the aluminum tube specimens that resemble wrinkling. These bands mask any shear localization evidence on the specimens and seem to affect the specimen stability. These bands are not seen on any other specimens. An effort to investigate the nature of the banding observed in the 36 mm polycarbonate coated tubes should be performed, as this might shed some light on limitations of applying a coating on components that experience a plane strain deformation path.

4.2 Plane Strain Expanding Tube Testing of Al 6061-O Samples

The goal of this set of experiments was to better define the particularities of an experimental setup to investigate the plane strain behavior of Al 6061-O tubes. In order to do this, the expanding tube experimental setup was modified to incorporate a longer solenoid, which would allow the expansion of longer tube samples which would approach a plane strain condition. The new coil, 112 mm long was designed and fabricated, and used to test five Al 6061-O tube samples, in lengths of 50, 70 and 90 mm. The testing performed yielded the following conclusions:

- The 112 mm coil behaved relatively similar to a shorter 36 mm coil at low voltages. The differences were not large enough, or particularly negative, to affect the expanding ring experiment meaningfully; however, it is possible that at higher voltage discharges, larger variations may appear.
- Expansion speeds between 15.5 – 90.1 m/s were experienced, corresponding to strain rates of ~1000 - 5900 s^{-1}, using discharge voltages in the range of 8 – 16 kV. The added mass of the specimens proved to slow down the expansion speed, pointing towards the need for higher voltages to achieve the same expansion speeds and strain rates as observed in the expanding ring experiment for 18 mm and 36 mm long samples.
- All tests showed flaring at the edges of the specimen, indicating that the samples were all too short for the coil. In order to achieve a uniform expansion of the entire sample a specimen longer than 90 mm needs to be used.
- Strain path observed by the longest specimen followed $\epsilon_1 = -3.4\epsilon_2$, which constitutes a very large migration towards a plane strain condition from the uniaxial stress state given by $\epsilon_1 = -2\epsilon_2$. Use of longer samples (> 90 mm) might approximate the desired condition even more.
- A sinusoidal profile of the specimen body was observed in almost all cases. This might be caused by a non-uniform Lorentz force interaction, product of using too large of a pitch for the coil helix, or too large of a wire diameter.
- Longitudinal banding resembling wrinkling is observed in almost all specimens. No shear localization bands can be observed. Additionally, the failure strain exhibited by the specimens was in the vicinity of 0.2, which is extremely low. Failures were observed to initiate at the edges, and might be triggered by the

presence of the longitudinal bands, although there is no concrete evidence to support this.

Based on these conclusions and observations made previously, the following recommendations were formed that would make future experimentation in this area even more useful,

- Larger voltage evaluations of the 112 mm coil need to be performed, to compare its performance at typical test voltages with shorter coils.
- Future tests need to be performed at higher discharge voltages, as to achieve higher expansion speeds and strain rates and therefore allow for a better comparison between the tubes expanded with the 112 mm coil and shorter specimens.
- A larger conical mirror must be employed that can reflect the entire sample surface, allowing for real time local strain measurements to be performed on the specimens using the conical mirror unwrapping techniques described in Section 2.1.1.1.
- An effort to identify the source of the body profile oscillations and longitudinal banding observed on the specimens should be carried out. An in-depth analysis needs to be performed to find a suitable explanation for the phenomena.
- Alternative solenoid designs that use smaller diameter wire, thicker epoxy coatings and smaller pitch in the winding should be explored, as these might provide a more uniform platform to expand the tube specimens.

4.3 Design of an Experimental Method for Rapid Acceleration of Metallic Plates to High Linear Velocities

The goal of this set of experiments was to validate the design of an electromagnetic inductive loading method to accelerate flat plate samples to speeds between 100 and 200 m/s. In order to achieve this, the expanding tube experimental setup was modified to incorporate a flat spiral coil that would provide a unidirectional loading on a metallic plate specimen. Three tests were performed to carry out this validation, using specimens of 30 x 30 mm and 65 x 65 mm; speeds in the range of 45.3 – 251.0 m/s were achieved. The testing performed yielded the following conclusions:

- Plate specimens exhibited an extremely fast acceleration, comparable to that observed in the expanding ring experiments. Over a period of 200 μs, the observed expansion speed is maintained almost constant, exhibiting a slight decrease that can be modeled satisfactorily by a second order polynomial fit.
- Deformation induced by non-uniformities in the application of driving force on the specimen resulted in very low strain levels of 0.05. The strain path observed was given by $\epsilon_{11} = \epsilon_{22}$., where the measured directions correspond to the edges of the square plates used in the tests.

Based on these conclusions, the following recommendations were formed, that would make future experimentation in this area even more useful,

- Test of larger samples using larger discharge voltages should be performed, with the goal of better characterizing the full potential of the experimental method. Additionally tests with specimens clamped at the edges should be performed to explore the behavior of the experimental setup under those conditions.

- A change in the coil design needs to be made to modify the support system and avoid future coil failure; support needs to be added to avoid bending during loading. Also, the epoxy coating over the spiral coil could be made thicker to provide more resistance to any bending, and a less brittle material could be used instead of epoxy to encase the coil, reducing the possibility of cracking.

Looking at the goals set out for this work and the results obtained, it is clear that the desired objectives were achieved, providing useful data and designs for future research to be performed in the area of high strain rate behavior of metallic specimens.

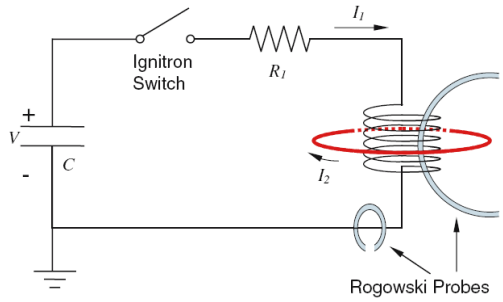

Figure 2.1. Schematic diagram of the expanding ring / tube experiment[3]. The specimen is shown in red.

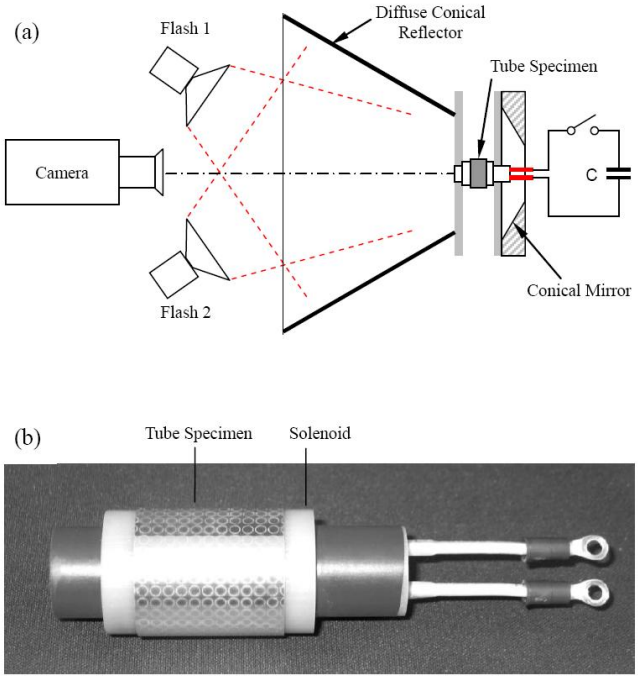

Figure 2.2 Images show a) schematic diagram of the experimental setup for the expanding tube experiment and a b) photograph of the solenoid and the tube specimen used in the expanding tube experiment.[4]

[3] Zhang H, Ravi-Chandar K (2006) On the dynamics of necking and fragmentation: I. Real-time and post mortem observations in Al-6061-O. Int J Fract 142:187. Fig. 1

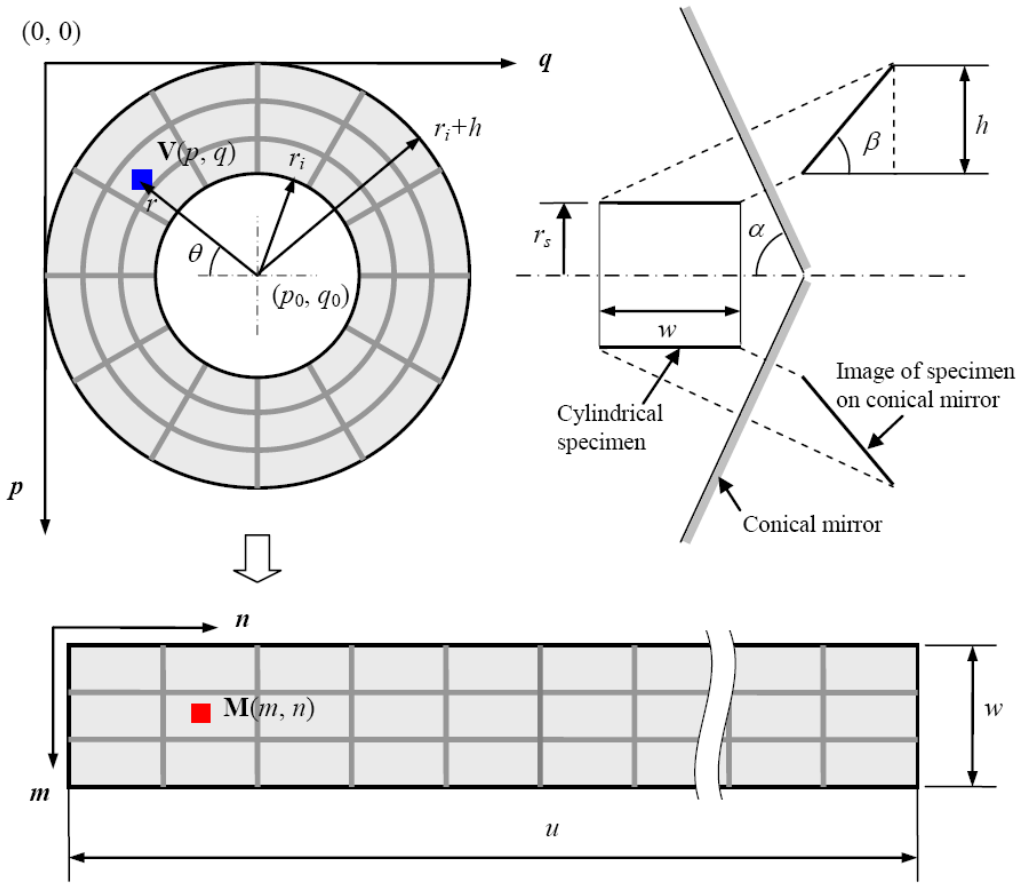

Figure 2.3 Schematic diagram showing the imaging optics for the conical mirror and mapping procedure used in the expanding tube experiment to convert the projected image on the mirror to the developed image of the surface of the cylindrical specimen[5]

---

[4] Zhang H, Ravi-Chandar K (2010) On the dynamics of necking and fragmentation: IV. Expansion of Al 6061-O tubes. Int J Fract 163:45. Fig. 1 a

[5] Zhang H, Ravi-Chandar K (2010) On the dynamics of necking and fragmentation: IV. Expansion of Al 6061-O tubes. Int J Fract 163:46. Fig. 2

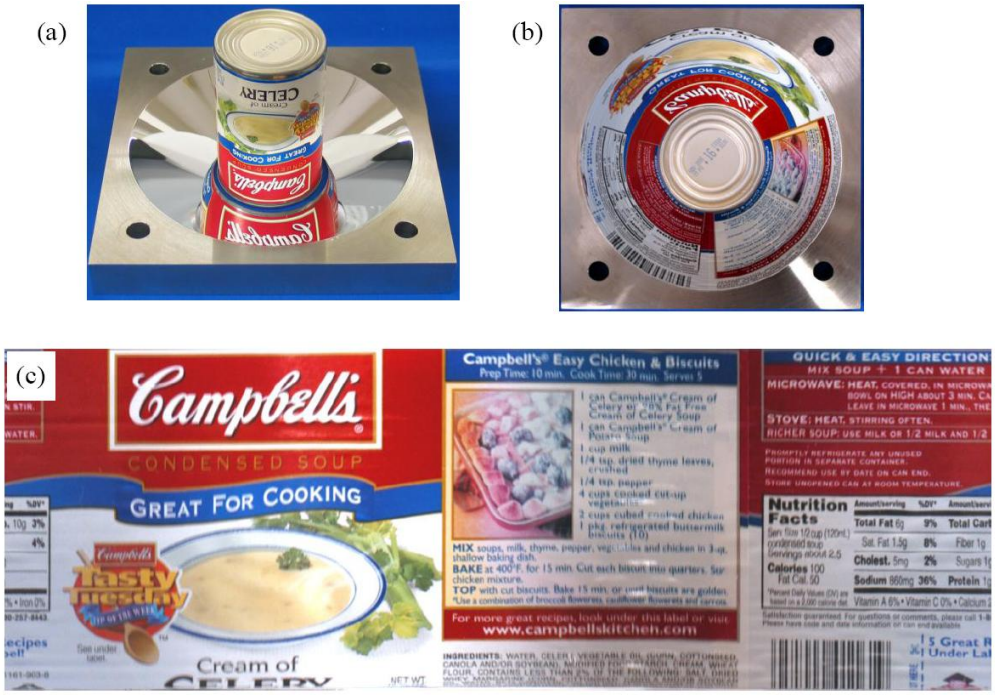

Figure 2.4 Example of unwrapping of a reflected image in a conical mirror as performed in the expanding tube experiment. Images show: a) conical mirror arrangement, b) direct view of reflected image and c) unwrapped image.[6]

6 Zhang H, Ravi-Chandar K (2010) On the dynamics of necking and fragmentation: IV. Expansion of Al 6061-O tubes. Int J Fract 163:47. Fig. 3

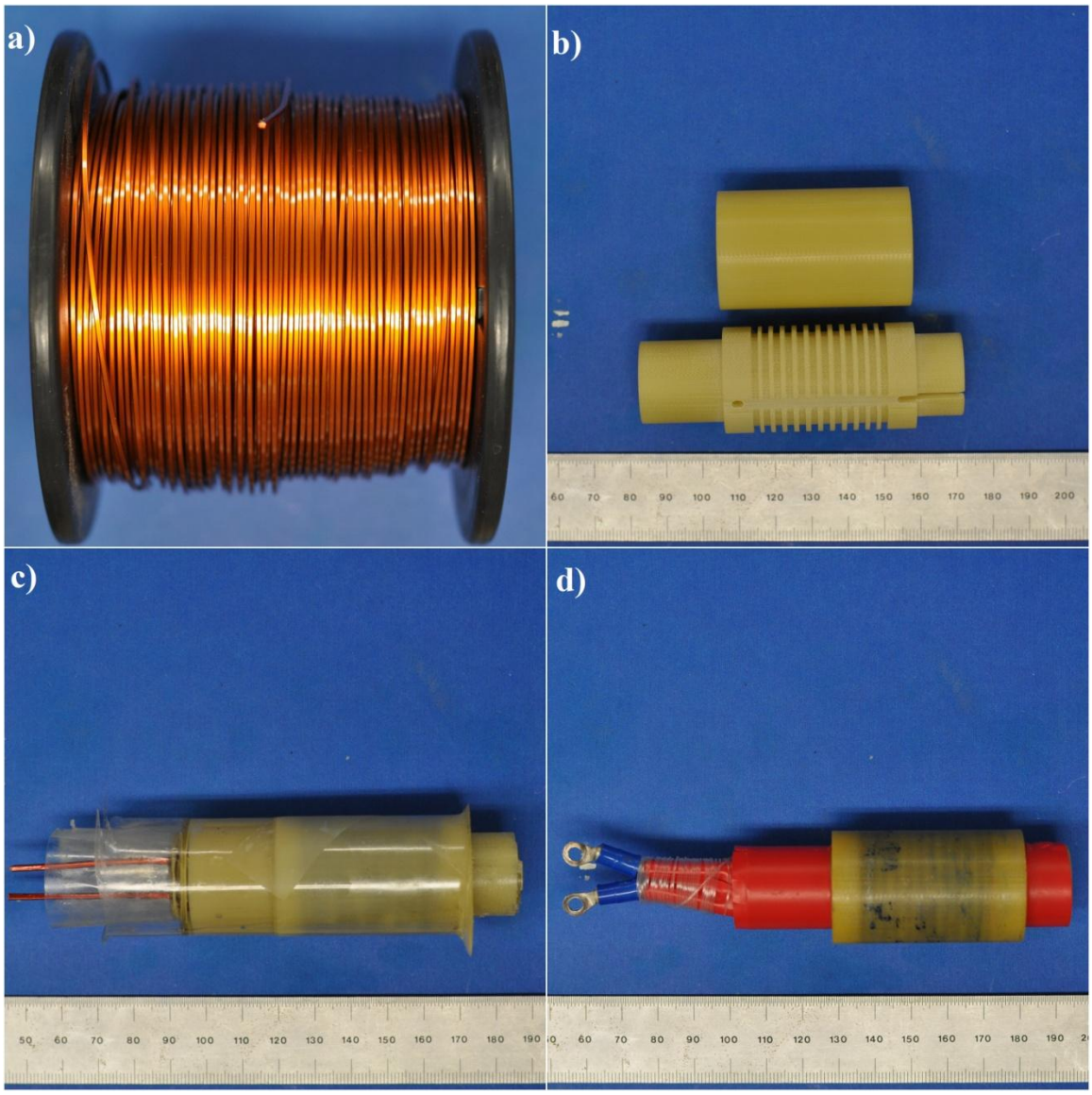

Figure 2.5 Sequence of 36 mm solenoid manufacture process. Images show a) 16-gauge square copper magnet wire spool b) 36 mm coil core and sleeve c) Epoxy covered 36 mm solenoid assembly d) Finished 36 mm solenoid.

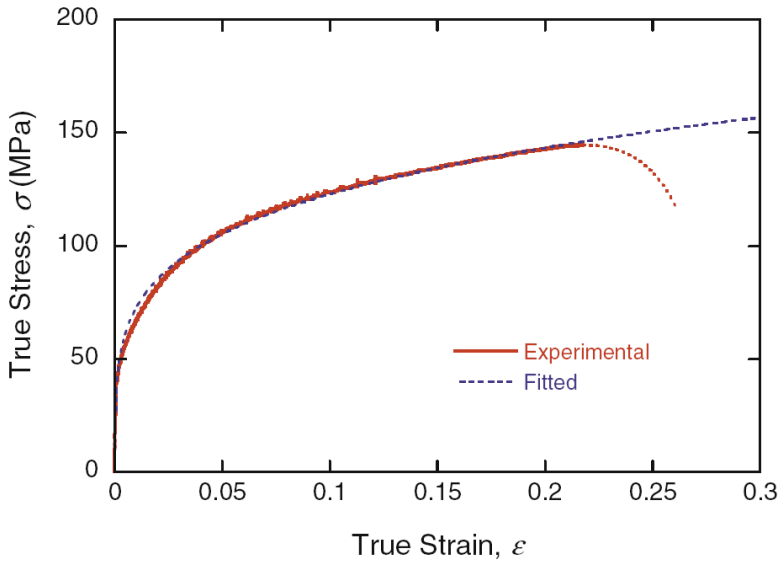

Figure 2.6 Quasi-static stress-strain curve for Al 6061-O. The dashed line is fitted by the power law described in Equation 2.16[7]

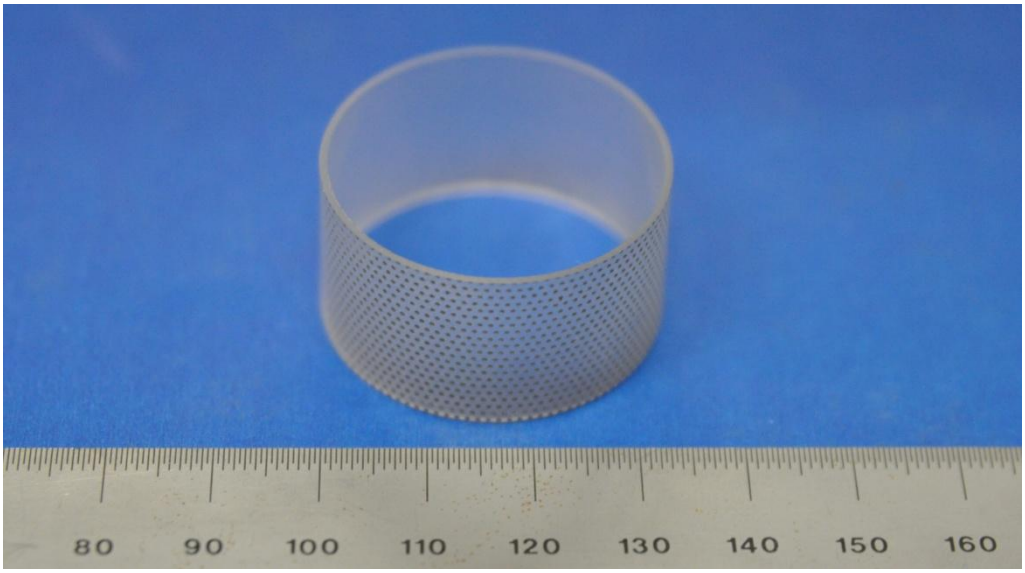

Figure 2.7 18 mm long polycarbonate sleeve showing a painted staggered dot pattern for real-time local strain measurement purposes

[7] Zhang H, Ravi-Chandar K (2006) On the dynamics of necking and fragmentation: I. Real-time and post mortem observations in Al-6061-O. Int J Fract 142:202. Fig. 14

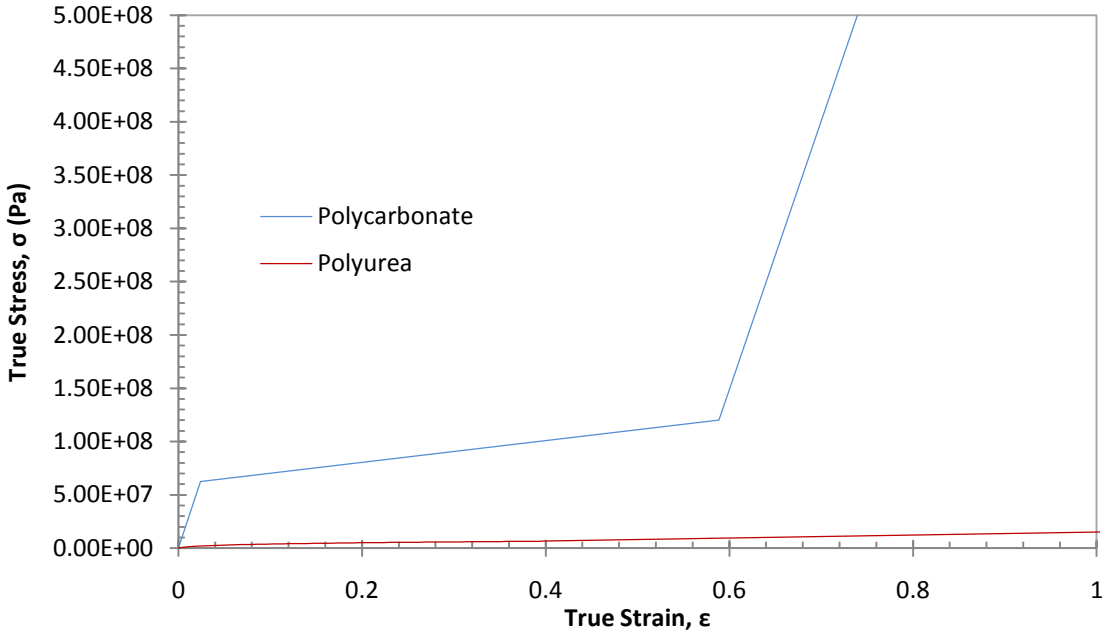

Figure 2.8 Quasi-static stress-strain curve for polycarbonate and polyurea

Figure 2.9 Solenoid prototype for expansion of Al 6061-O tube samples of lengths between 36 and 100 mm. Coil is 112 mm and contains a 23 turn helical winding made from 8-gauge copper wire.

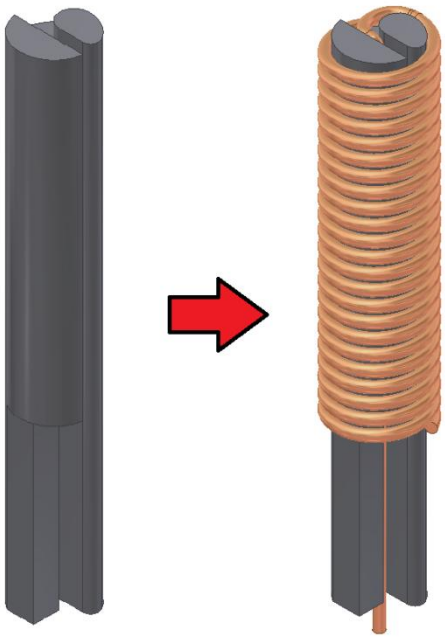

Figure 2.10 Winding tool and demonstration of helical coil winding for the manufacture of a 112 mm solenoid.

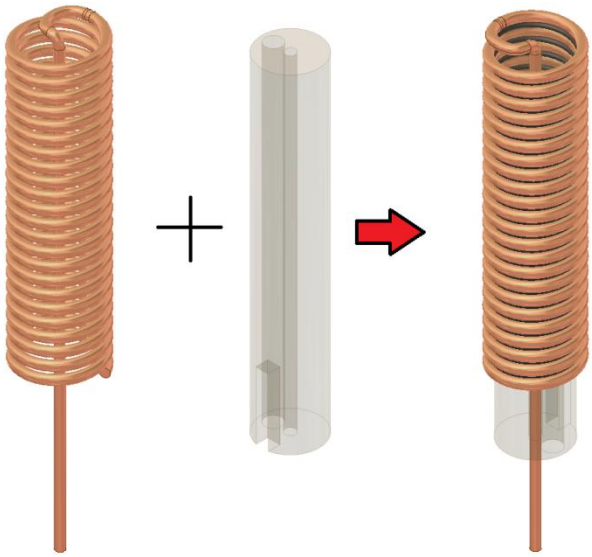

Figure 2.11 Polycarbonate core installation in helical winding during 112 mm solenoid manufacture

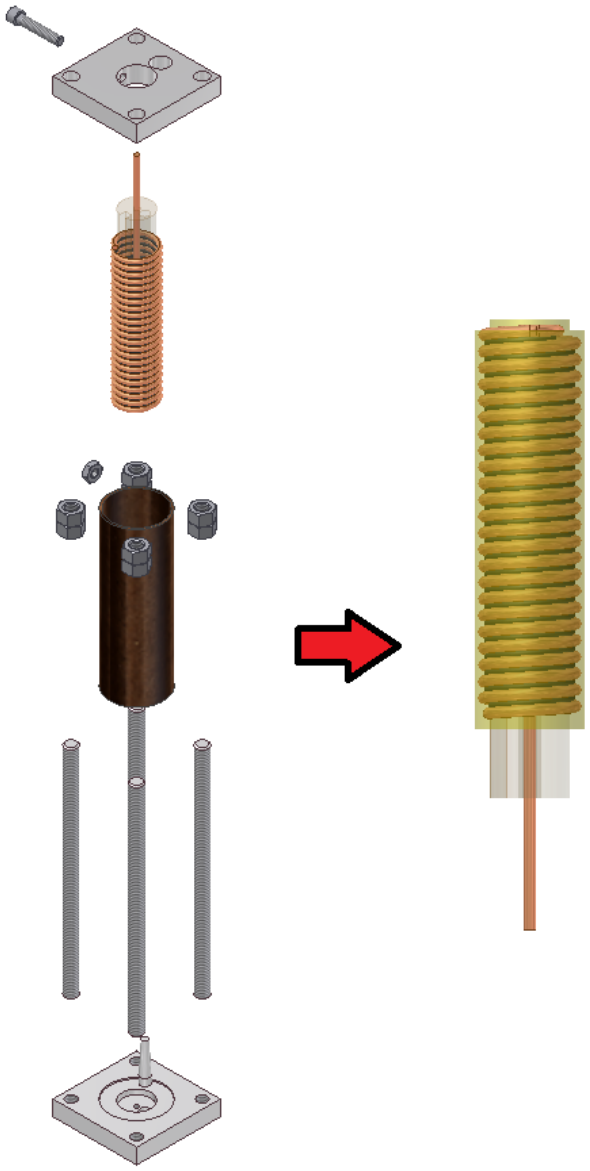

Figure 2.12 Exploded view of vertical mold used for 112 mm coil manufacture and illustration of finished solenoid.

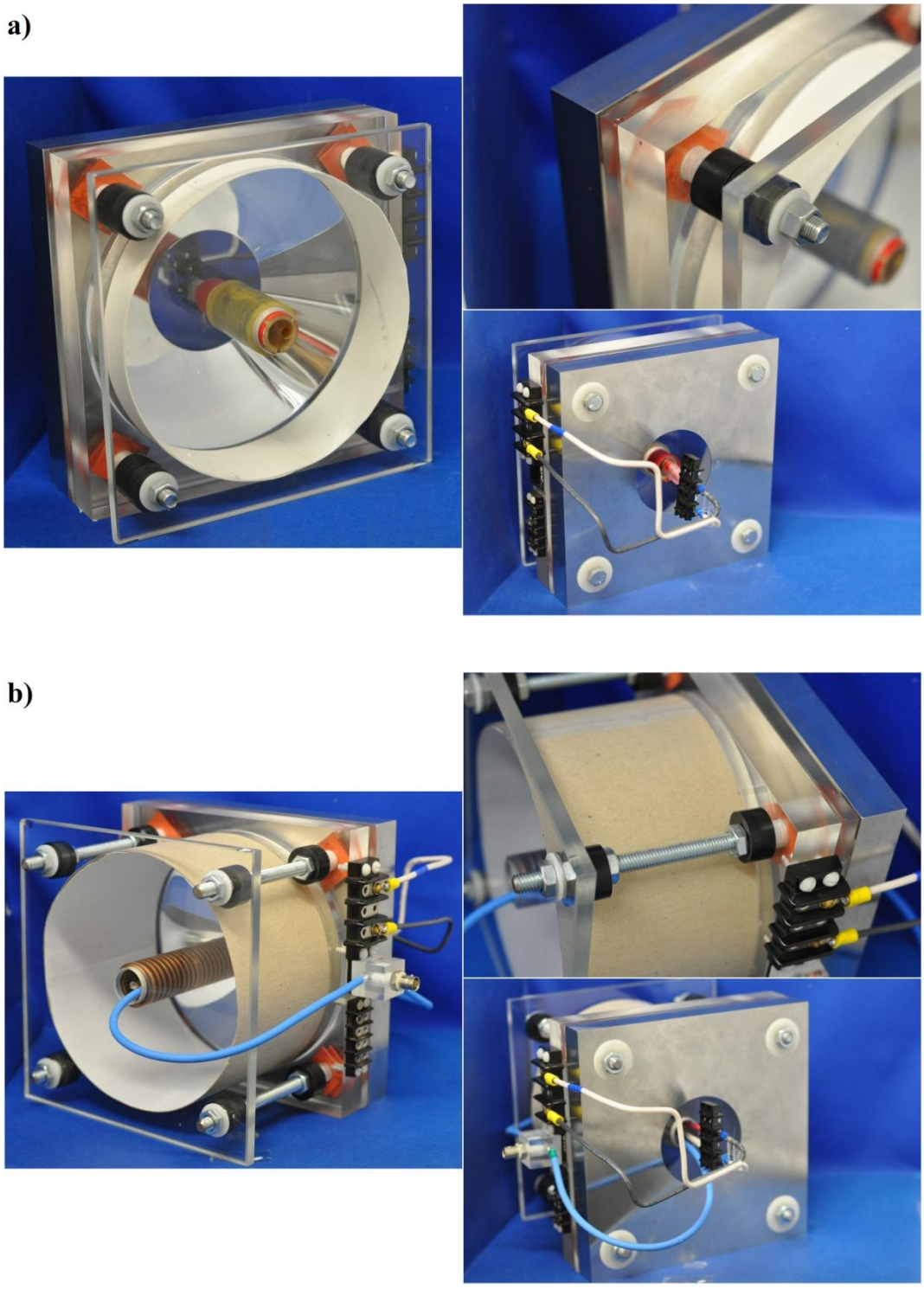

Figure 2.13 Containment enclosure for a) traditional expanding tube experiment and b) expanding tube experiment with 112 mm coil for plane strain testing

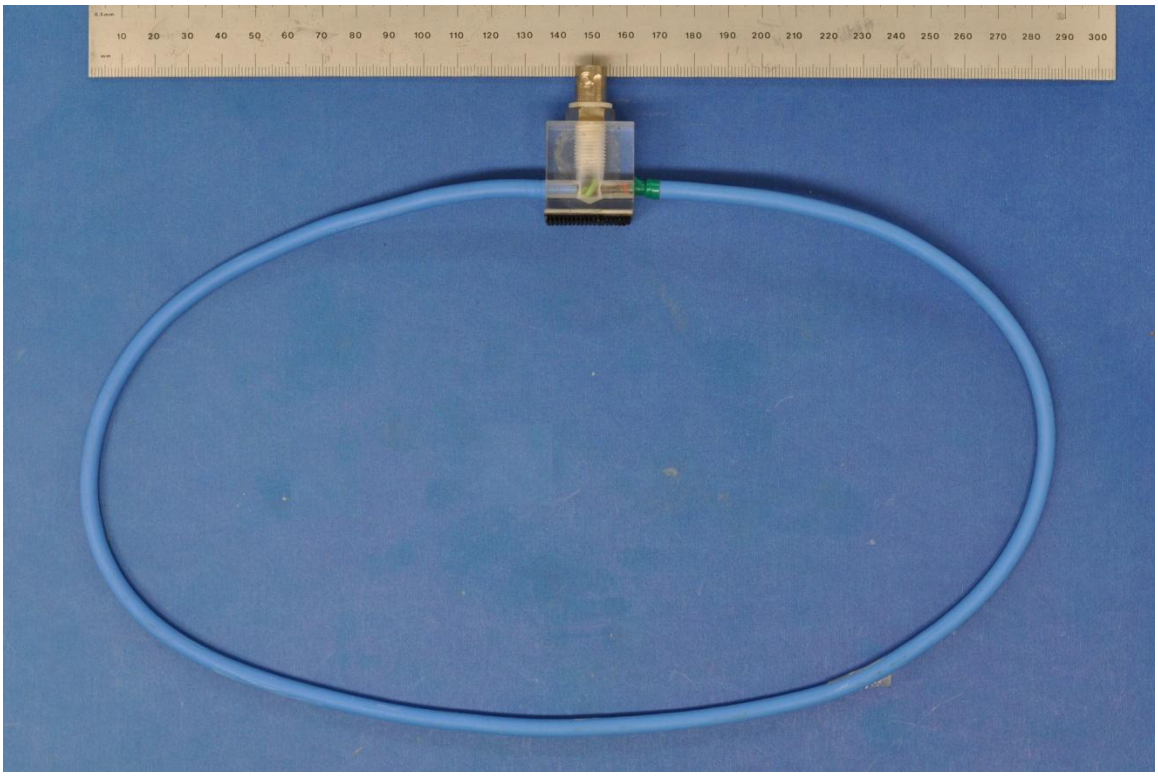

Figure 2.14 Rogowski coil for use with extended containment enclosure in expanding tube experiment with a 112 mm solenoid.

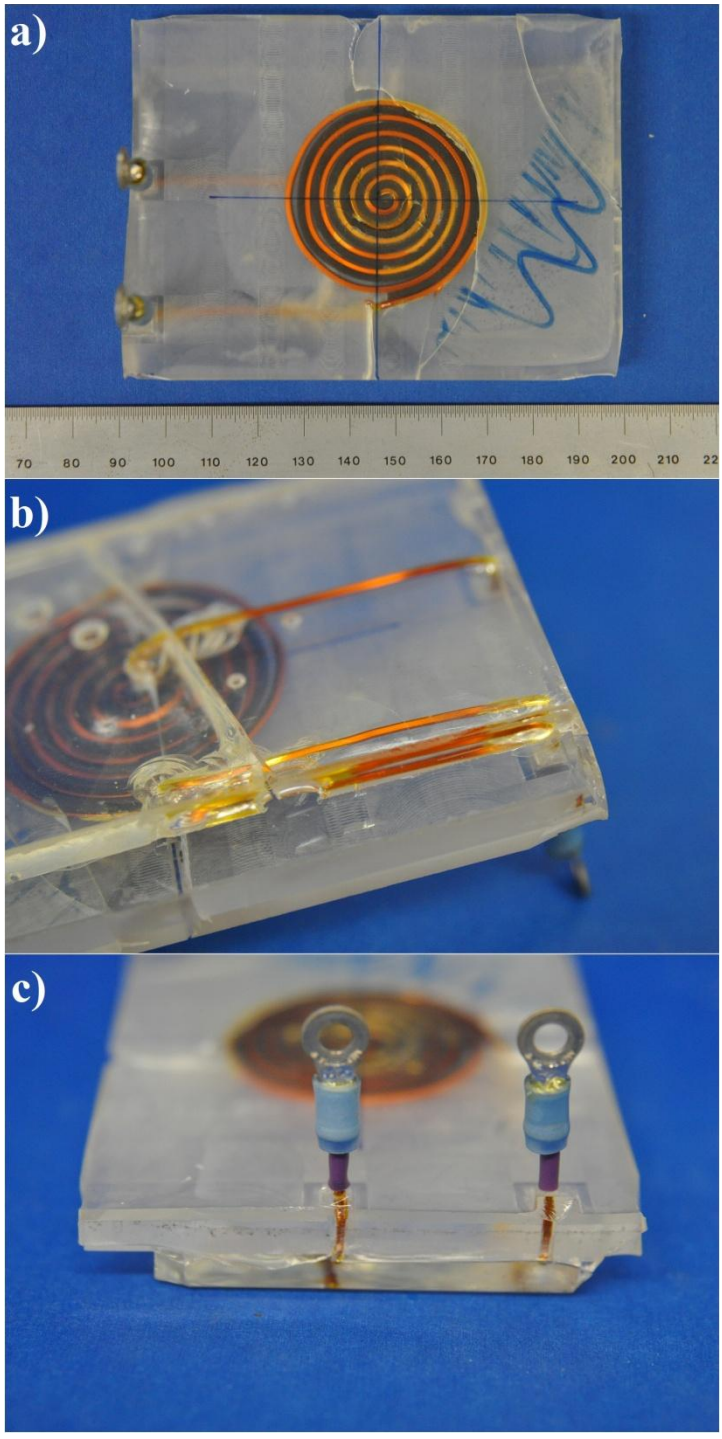

Figure 2.15 Images of spiral coil design, showing: a) close-up view of winding b) close-up view of methods used to lock wire under polycarbonate plate and c) detail view of connectors.

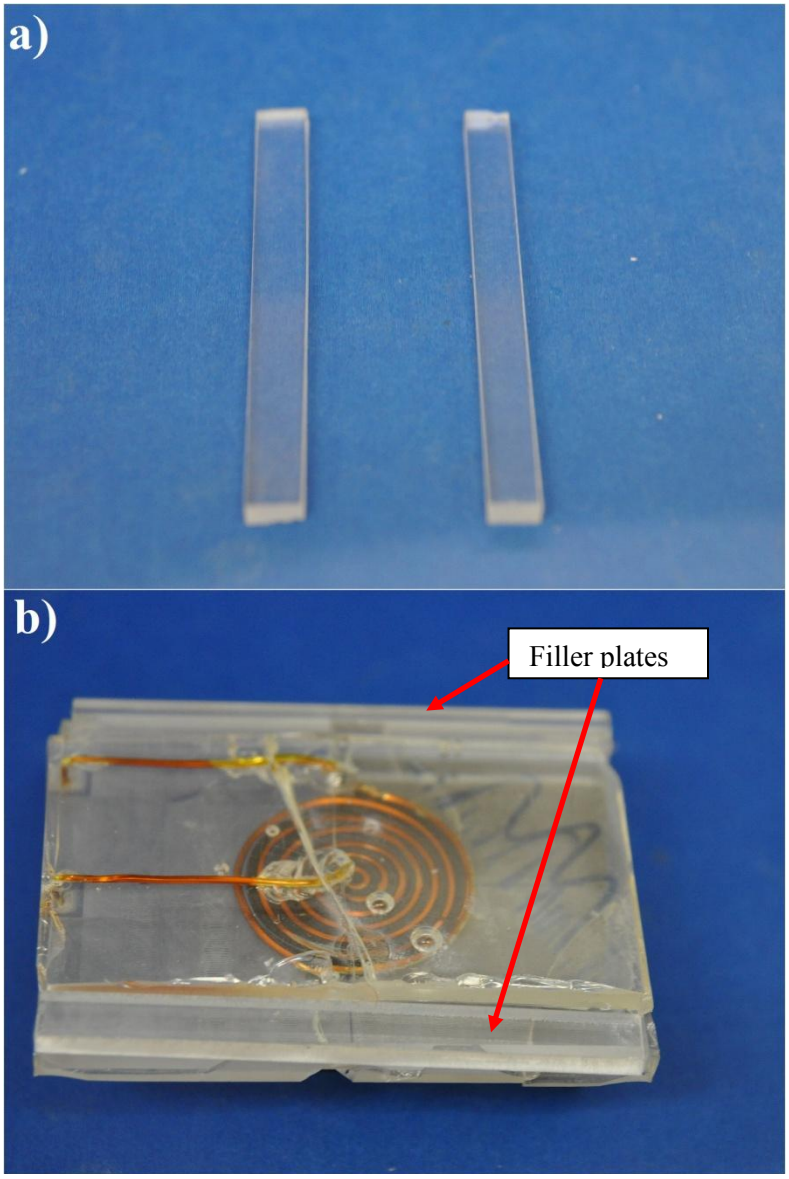

Figure 2.16 Images of filler plates used to mold reference cavities into epoxy covering of coil. Images show a) polycarbonate filler plates and b) location of filler plates with respect to the spiral winding during the epoxy pour. The surface shown in image b) corresponds to that in contact with the bottom of the mold.

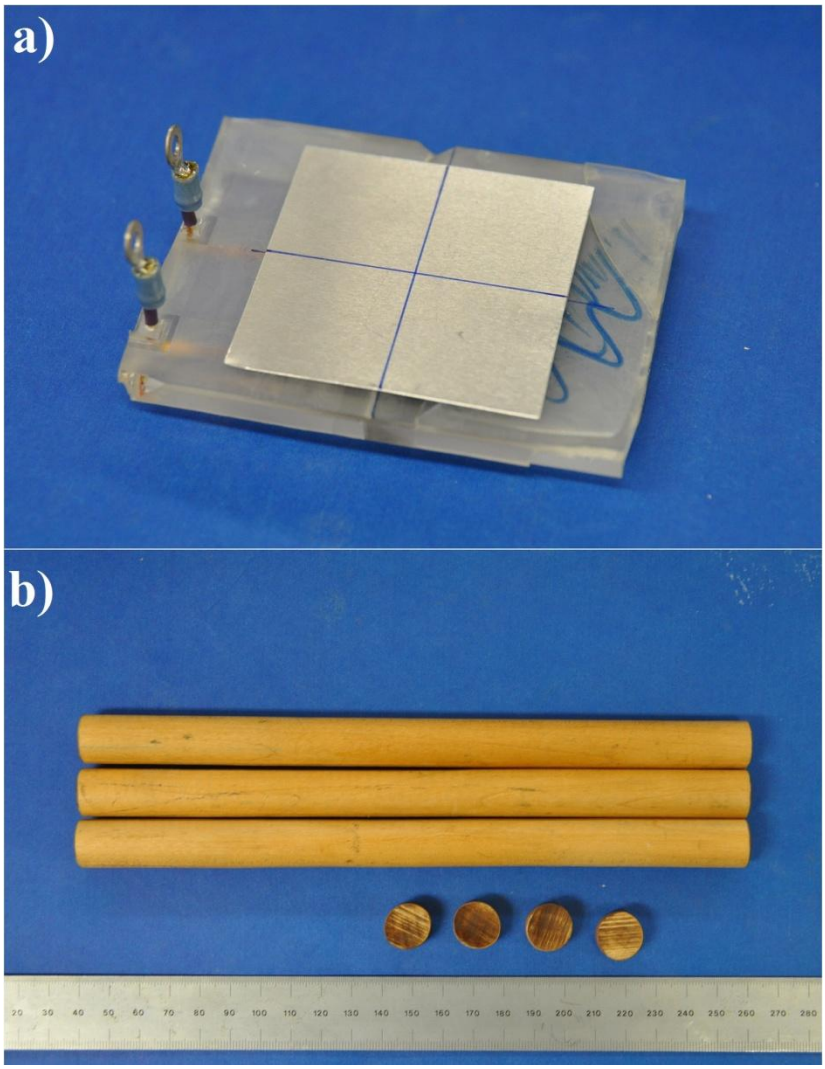

Figure 2.17 Images of elements of the experimental setup: a) plate specimen in position on the spiral coil and b) posts and spacers used to hold the coil in place during testing.

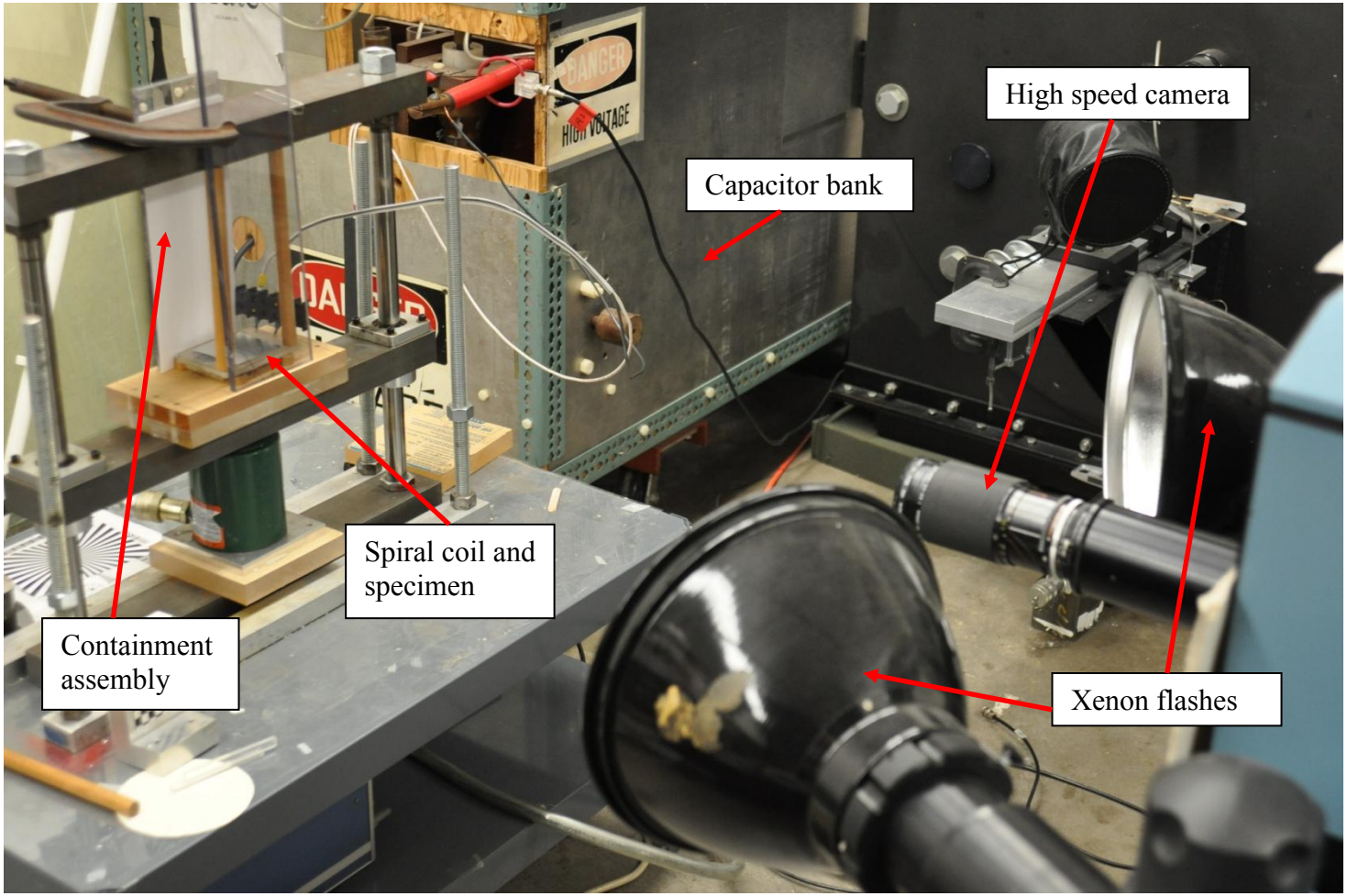

Figure 2.18 Image of experimental setup used for flat plate acceleration experiments.

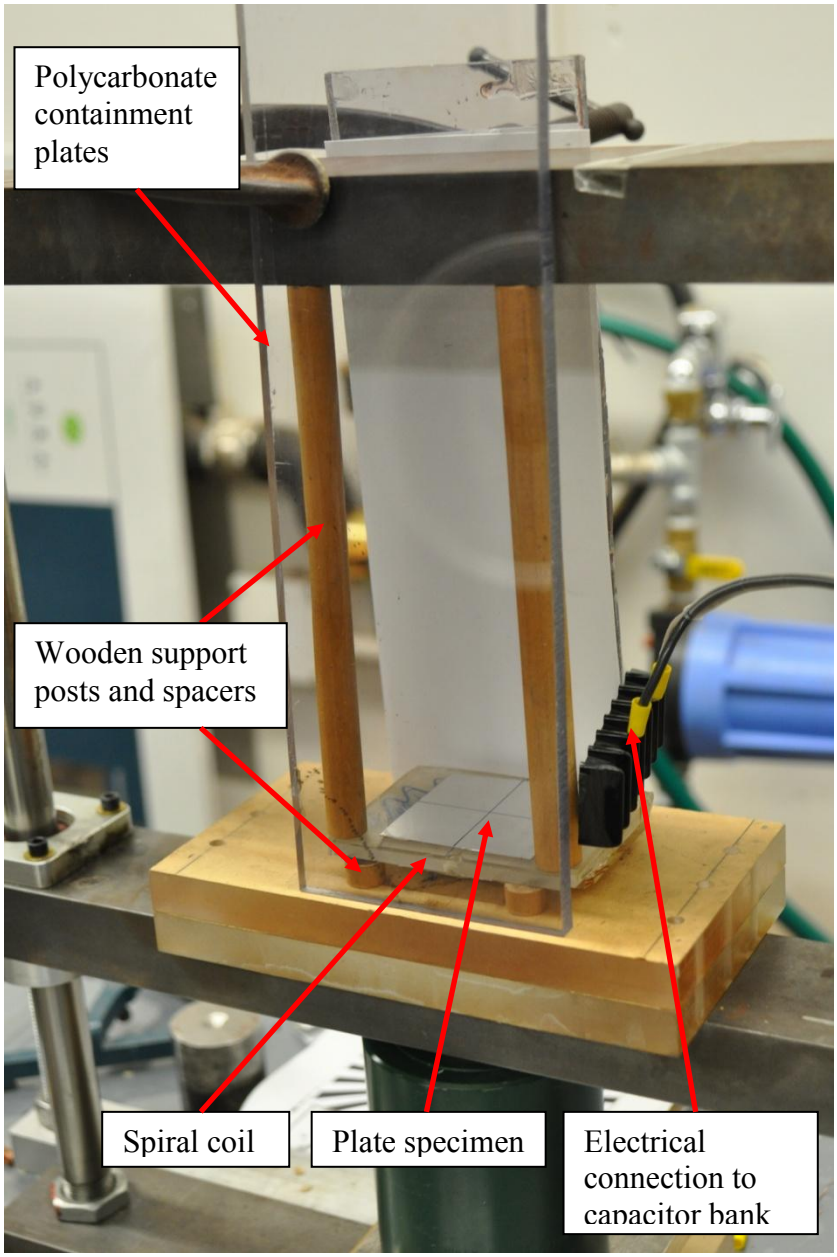

Figure 2.19 Close-up view of sample containment assembly for flat plate acceleration experiments

Table 1. List of high speed expanding tube tests on polymer coated Al 6061-O samples

Test number	Cladding material	Tube length (mm)	Charging voltage (kV)	Tube thickness (mm)	Cladding thickness (mm)	Expansion velocity (m/s)[a]	Strain rate (s^-1)
PC-1	Polycarbonate	18	13	0.51	0.49	64.6	4236
PC-2	Polycarbonate	18	14	0.50	0.50	83.3	5462
PC-3	Polycarbonate	18	15	0.51	0.50	90.4	5928
PC-4	Polycarbonate	18	16	0.53	0.49	82.4	5403
PC-5	Polycarbonate	36	13	0.50	0.48	61.1	4007
PC-6	Polycarbonate	36	14	0.50	0.49	67.5	4426
PC-7	Polycarbonate	36	15	0.50	0.48	86.6	5679
PU-1	Polyurea	18	14	0.50	0.32	102.8	6741
PU-2	Polyurea	18	15	0.50	0.32	141.3	9266
PU-3	Polyurea	18	16	0.50	0.34	136.1	8925
PU-4	Polyurea	36	13	0.50	0.45	81.4	5338
PU-5	Polyurea	36	15	0.50	0.70	55	3607
PU-6	Polyurea	36	15	0.50	0.50	101.5	6656

[a] The steady ring expansion speed reached in the 15-50μs interval is quoted.

Table 2. List of high speed expanding tube tests on bare Al 6061-O samples[8]

Test number	Tube length (mm)	Charging voltage (kV)	Expansion velocity (m/s)[a]	Strain rate (s^-1)
Al-1	18	12	69	4525
Al-2	18	12	120	7869
Al-3	18	13	141	9246
Al-4	18	14	176	11541
Al-5	18	14	167	10951
Al-6	18	14	196	12852
Al-7	36	12	100	6557
Al-8	36	13	116	7607
Al-9	36	14	156	10230
Al-10	36	14	146	9574
Al-11	36	15	171	11213
Al-12	36	15	170	11148

[a] The steady ring expansion speed reached in the 15-50μs interval is quoted.

[8] Data comes from Zhang H, Ravi-Chandar K (2010) On the dynamics of necking and fragmentation: IV. Expansion of Al 6061-O tubes. Int J Fract 163:49. Table 1

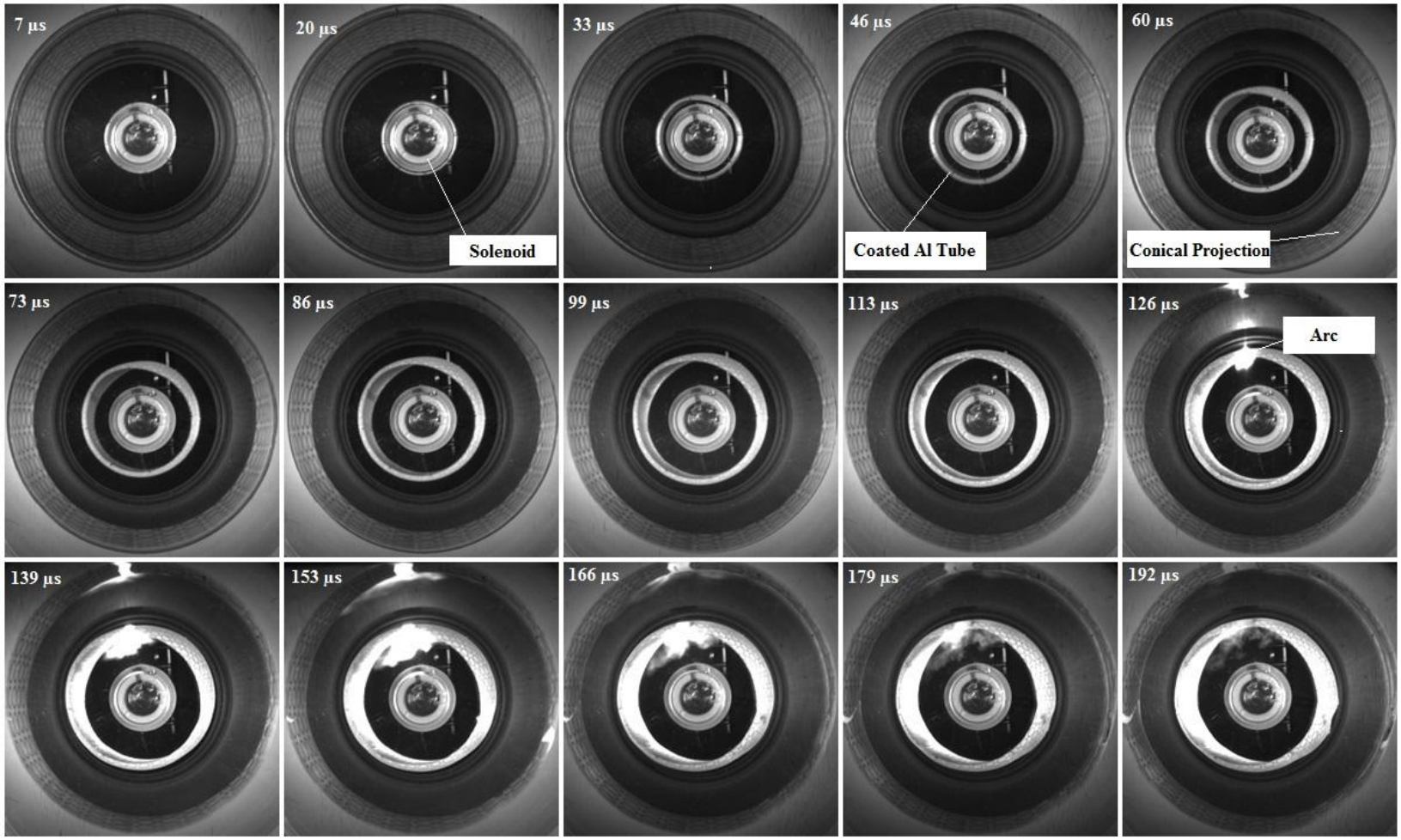

Figure 3.1 High speed images showing expansion of an Al 6061-O tube (w = 18mm) with a polyurea coating, expanding at 136.1 m/s (Test PU-3)

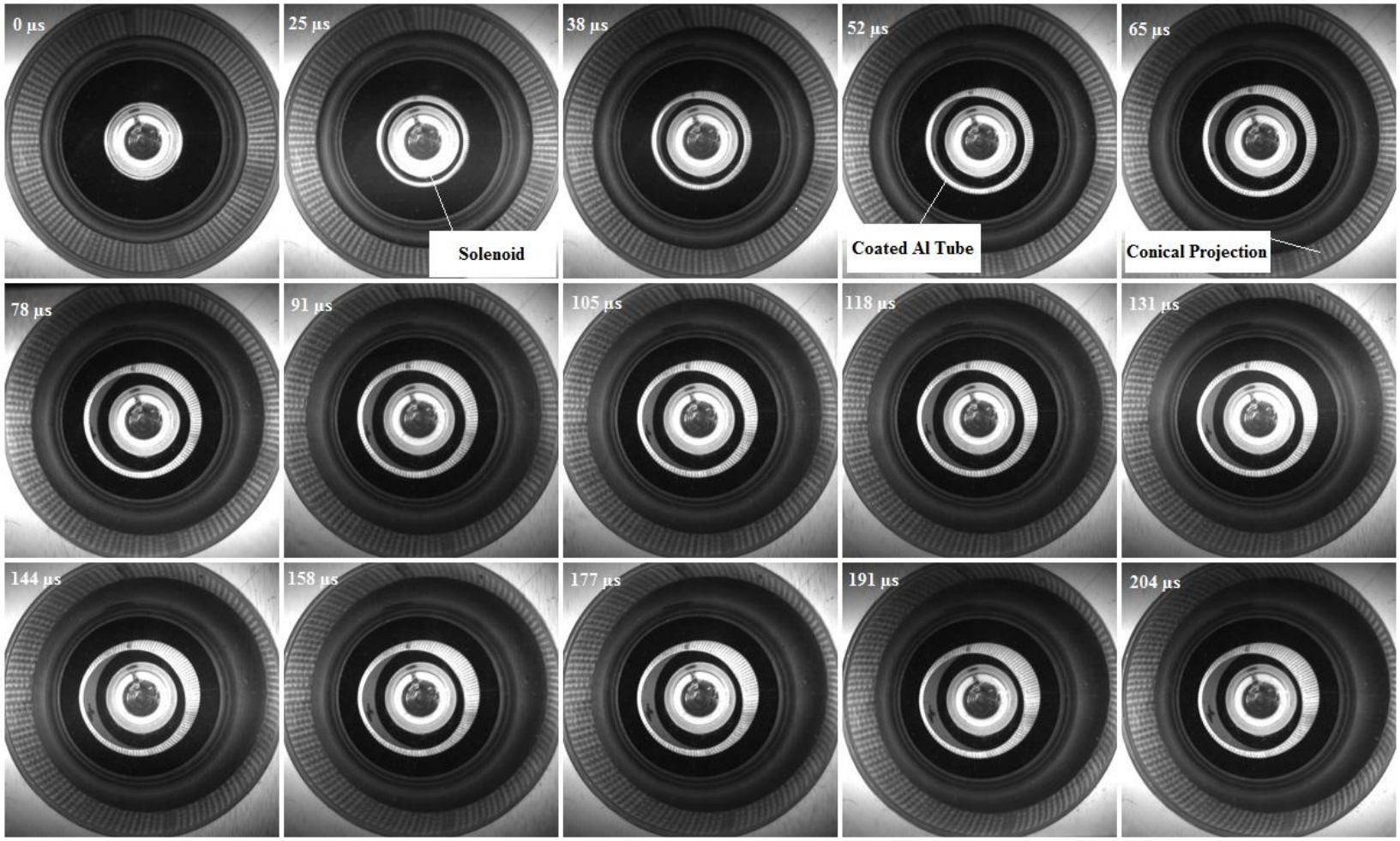

Figure 3.2 High speed images showing expansion of an Al 6061-O tube (w = 18mm) with a polycarbonate coating, expanding at 90.4 m/s (Test PC-3)

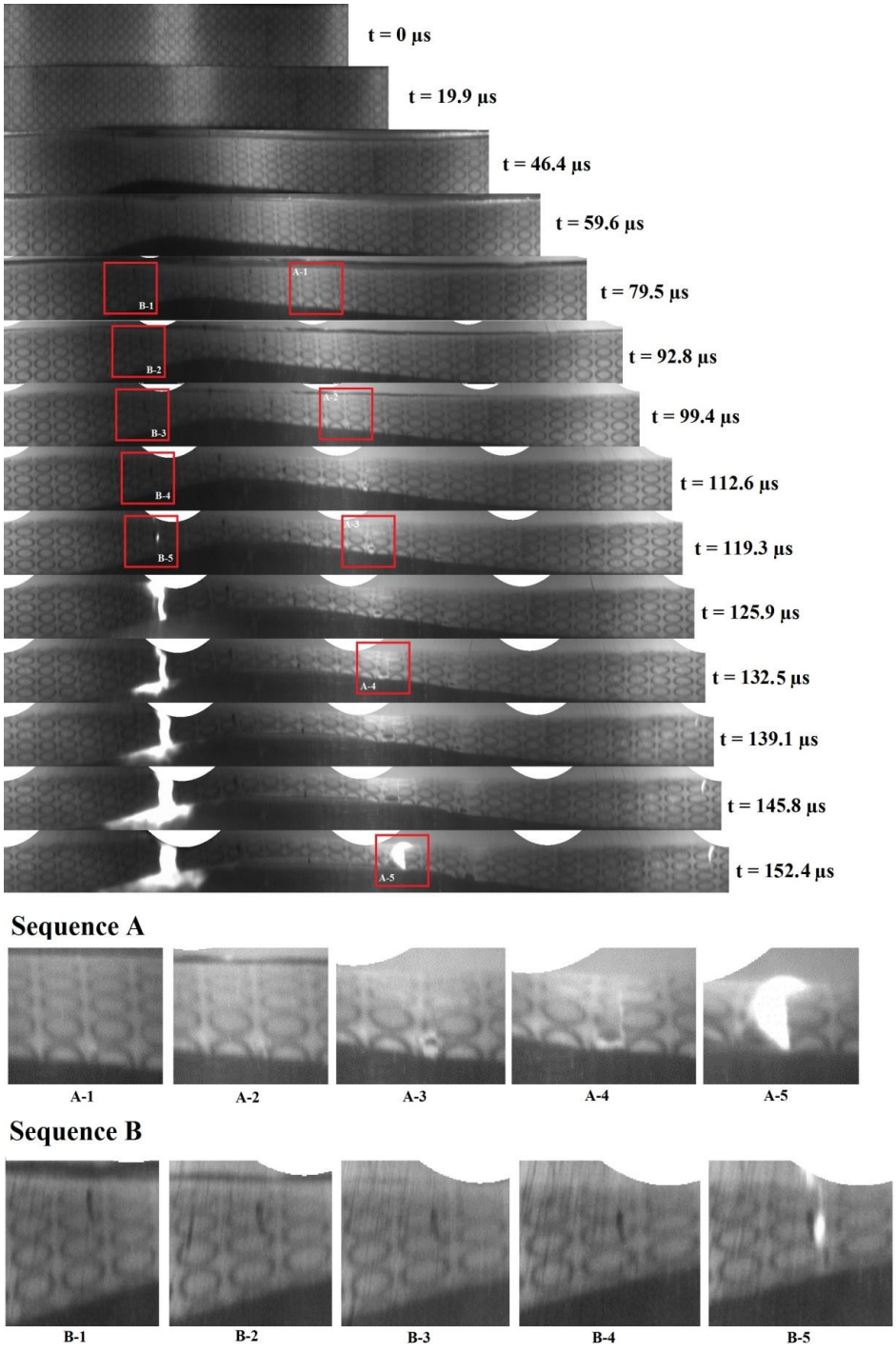

Figure 3.3 Sequence of unwrapped images for test PU-3 indicating the deformation on the surface of the cylinder.

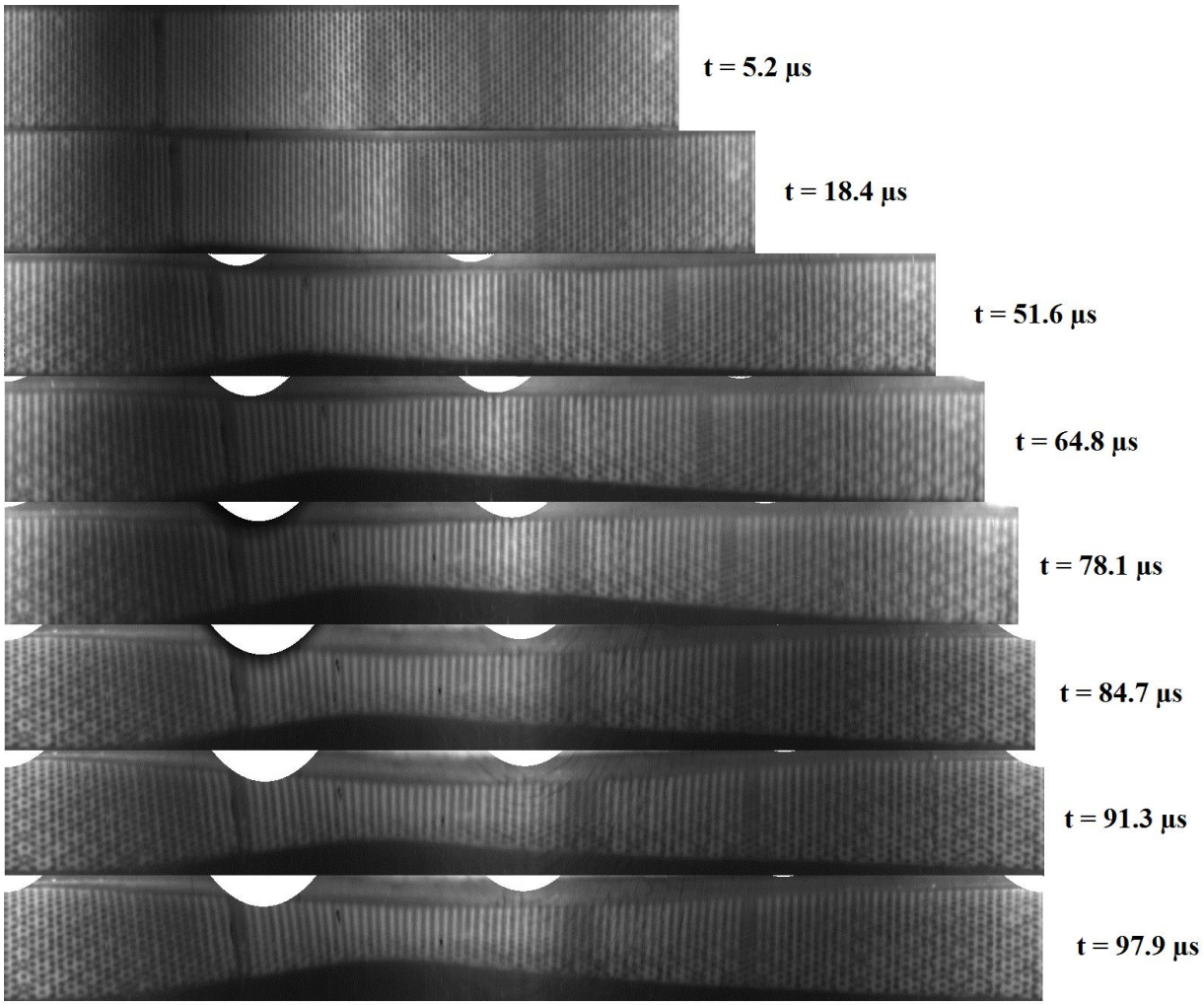

Figure 3.4 Sequence of unwrapped images for test PC-3 Indicating the deformation on the surface of the cylinder.

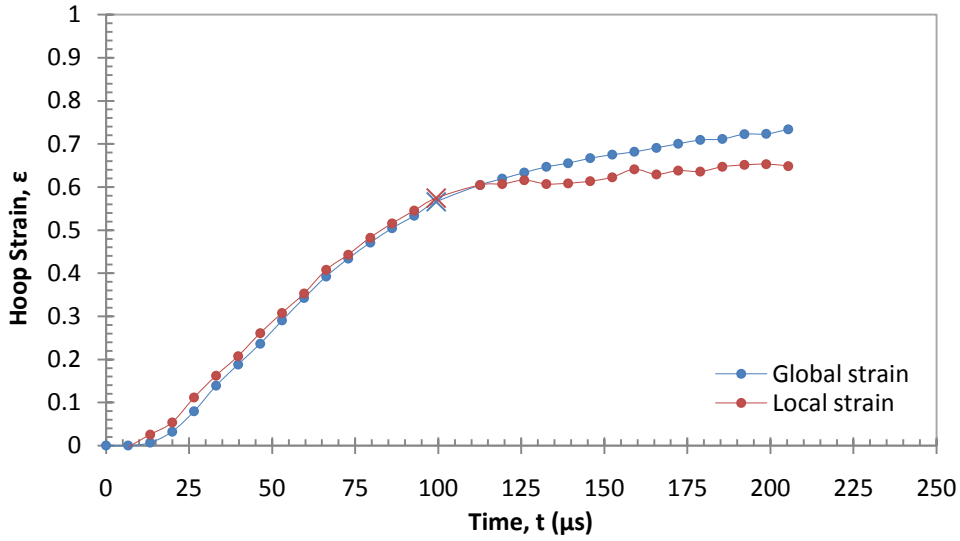

Figure 3.5 Variation of hoop strain with time for test PU-3: the global quantity was determined by measuring the variation of average tube radius, while the local strain was obtained from measurements of the deformation of an etched circle on the sample surface. The X marks the fracture point.

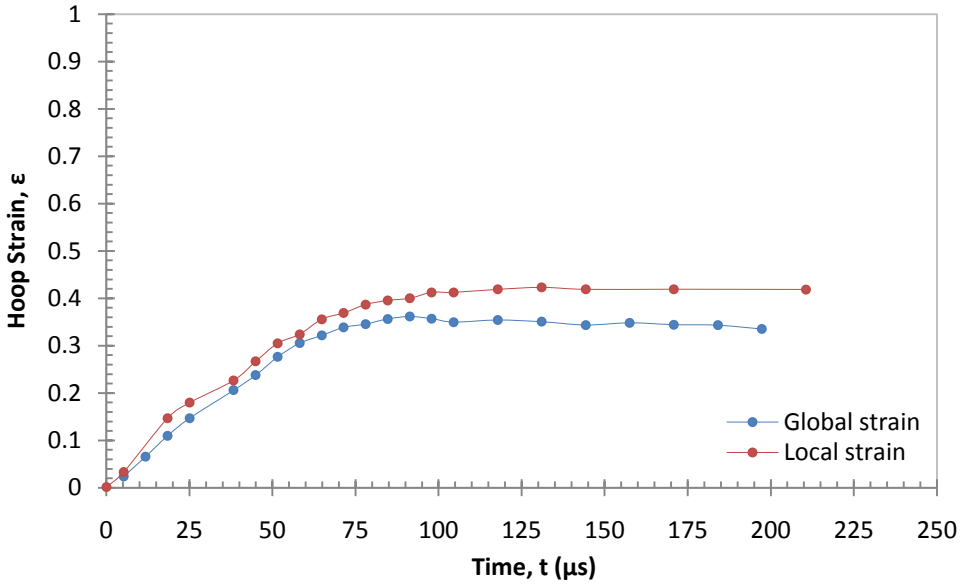

Figure 3.6 Variation of hoop strain with time for test PC-3: the global quantity was determined by measuring the variation of average tube radius, while the local strain was obtained from measurements of the deformation of a staggered circle pattern painted on the coating surface.

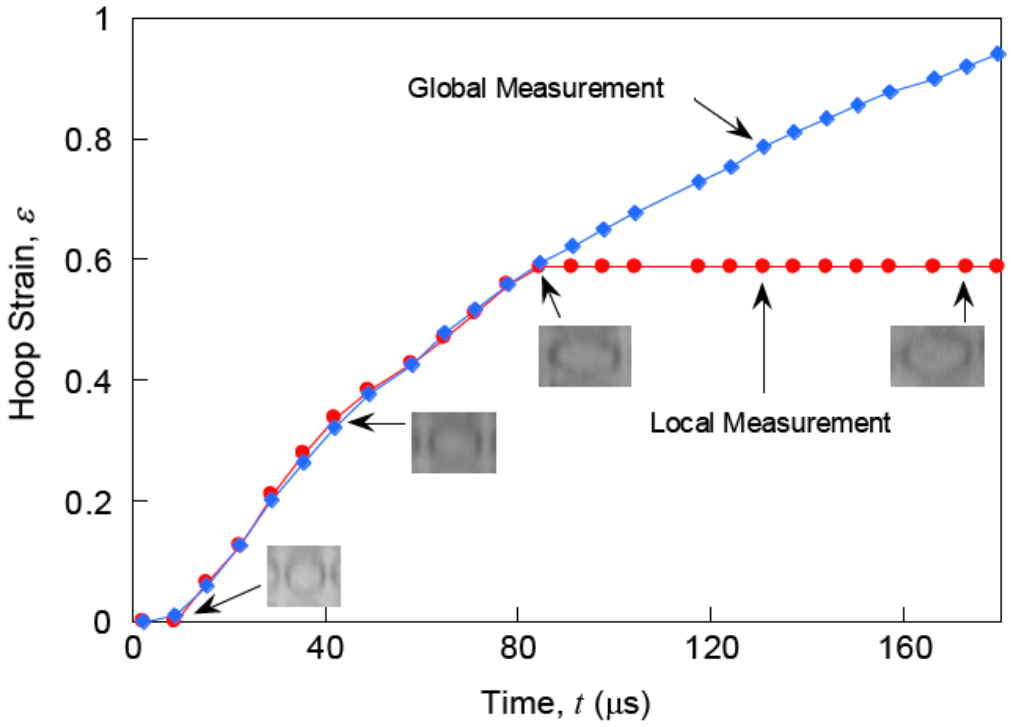

Figure 3.7 Variation of the hoop strain with time for an uncoated Al-6061-O, 36 mm tube[9].

[9] Zhang H, Ravi-Chandar K (2010) On the dynamics of necking and fragmentation: IV. Expansion of Al 6061-O tubes. Int J Fract 163:52. Fig. 3

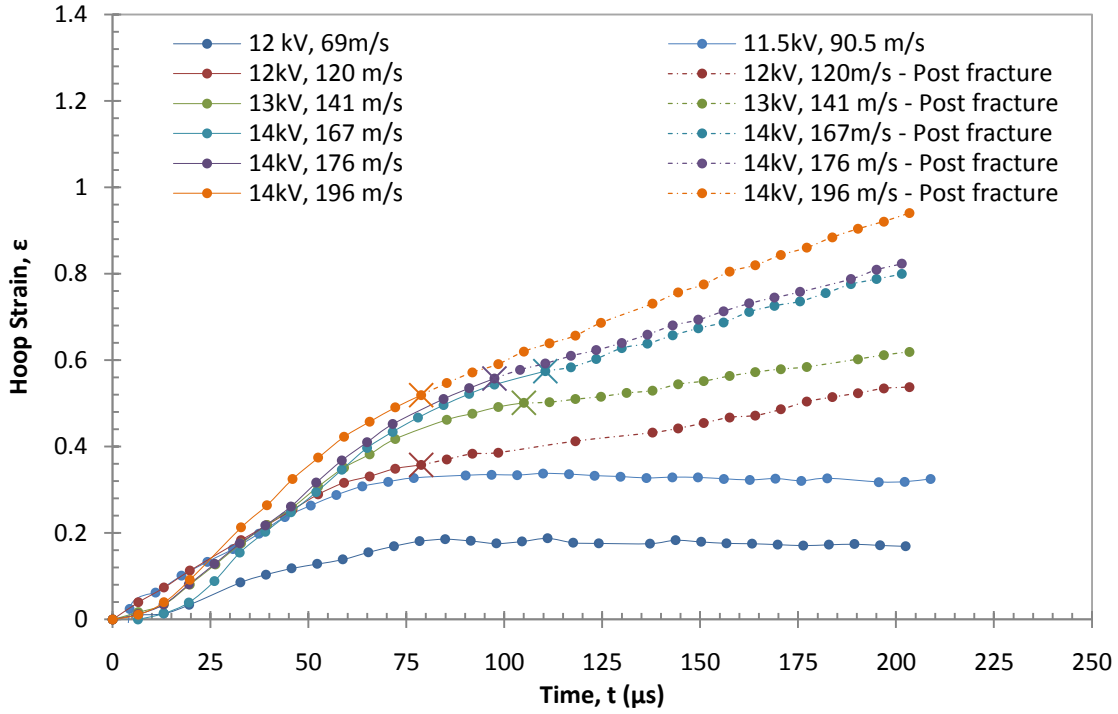

Figure 3.8 Variation of global hoop strain with time for uncoated Al 6061-O 18 mm tubes used by Zhang and Ravi-Chandar (2010). Note the rigid body expansion observed in all the fractured specimens. The samples that did not fracture hit a plateau after the driving force was extinguished. The X marks the fracture point.

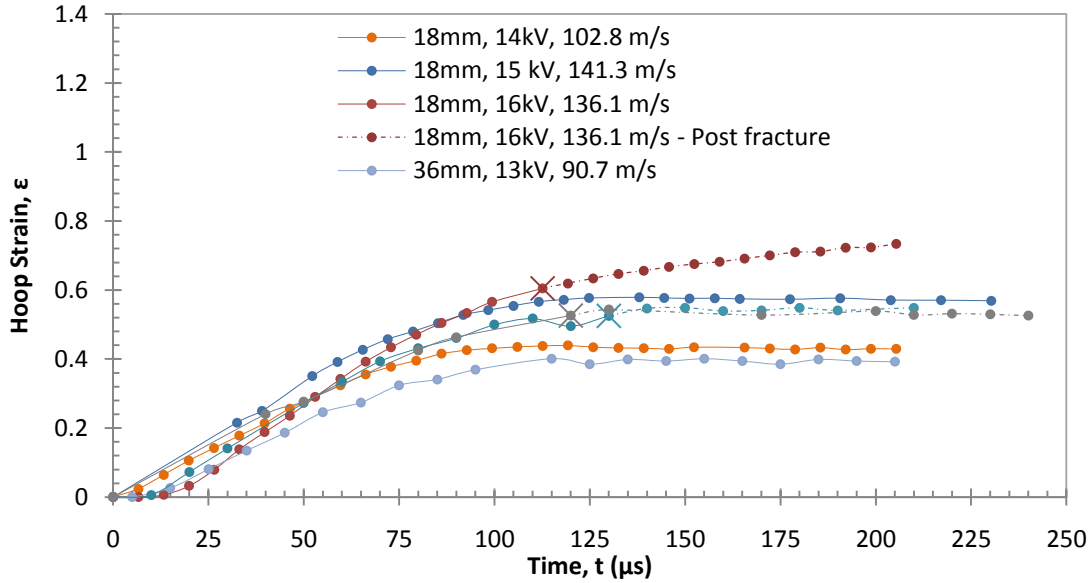

Figure 3.9 Variation of global hoop strain with time for polyurea coated Al 6061-O tubes of 18 mm and 36 mm lengths: Note the rigid body expansion observed in all the fractured specimens. The samples that did not fracture hit a plateau after the driving force was extinguished. The X marks the fracture point.

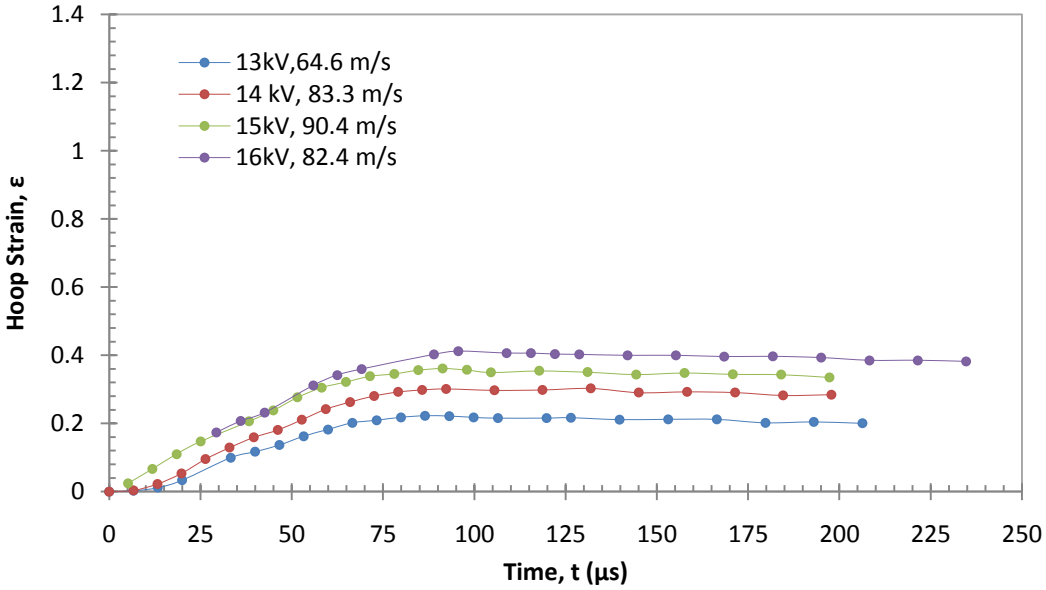

Figure 3.10 Variation of global hoop strain with time for 18 mm long polycarbonate coated Al 6061-O tubes: Note that the samples did not fracture; hitting a plateau after the driving force was extinguished.

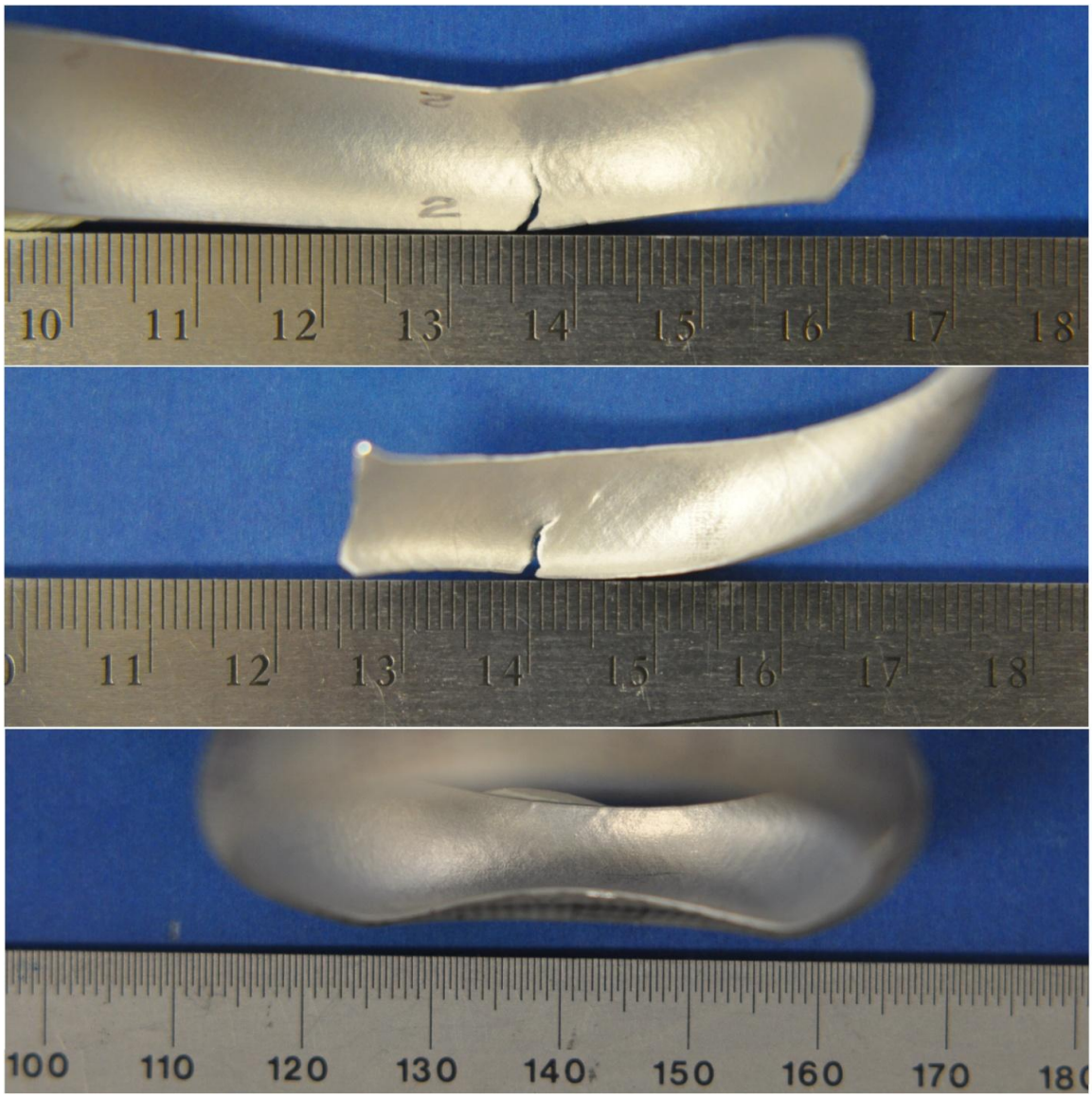

Figure 3.11 Variation of localization band intensity and distribution for different tests. The top image corresponds to an 18 mm long bare Al 6061-O cylinder under a 12 kV discharge, generating a expansion velocity of 120 m/s (Al-2). The middle image corresponds to test PU-3. The lower image corresponds to test PC-4. Note how in the top image, the most defined localization bands occur around the crack and become less defined as you move away from it. In the other two images, the distribution of the localization bands is uniform throughout, being a lot more defined for the PU-3 test.

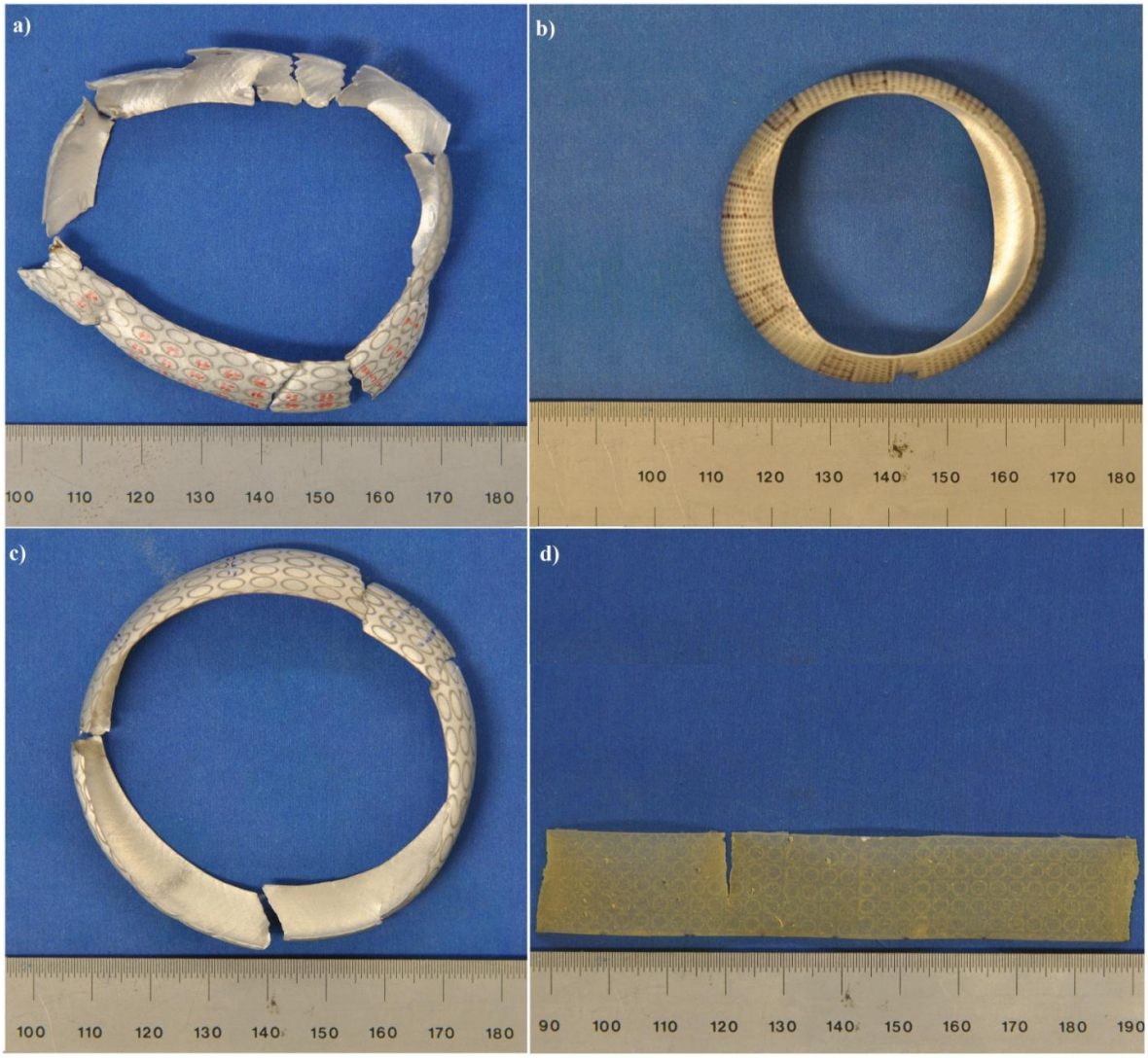

Figure 3.12 Expansion comparisons for bare Al 6061-O, polyurea coated Al 6061-O and polycarbonate coated Al 6061-O. Image a) corresponds to a bare Al 6061-O tube, 18 mm long, expanded with a discharge voltage of 14 kV and attaining a radial expansion speed of 196 m/s. Image b) corresponds to a polycarbonate coated Al 6061-O tube, 18 mm long, expanded with a discharge voltage of 16 kV and attaining a radial expansion speed of 82.4 m/s (Test PC-4). Finally, images c) and d) correspond to a polyurea coated Al 6061-O tube, 18 mm long, expanded with a discharge voltage of 16 kV and attaining a radial expansion speed of 136.1 m/s. Note that image c) shows the expanded aluminum tube and d) the polyurea coating. The coating has contracted back approximately to its original dimensions, implying that the polyurea coating absorbs energy via elastic deformation. The polycarbonate coating does so in the form of plastic deformation.

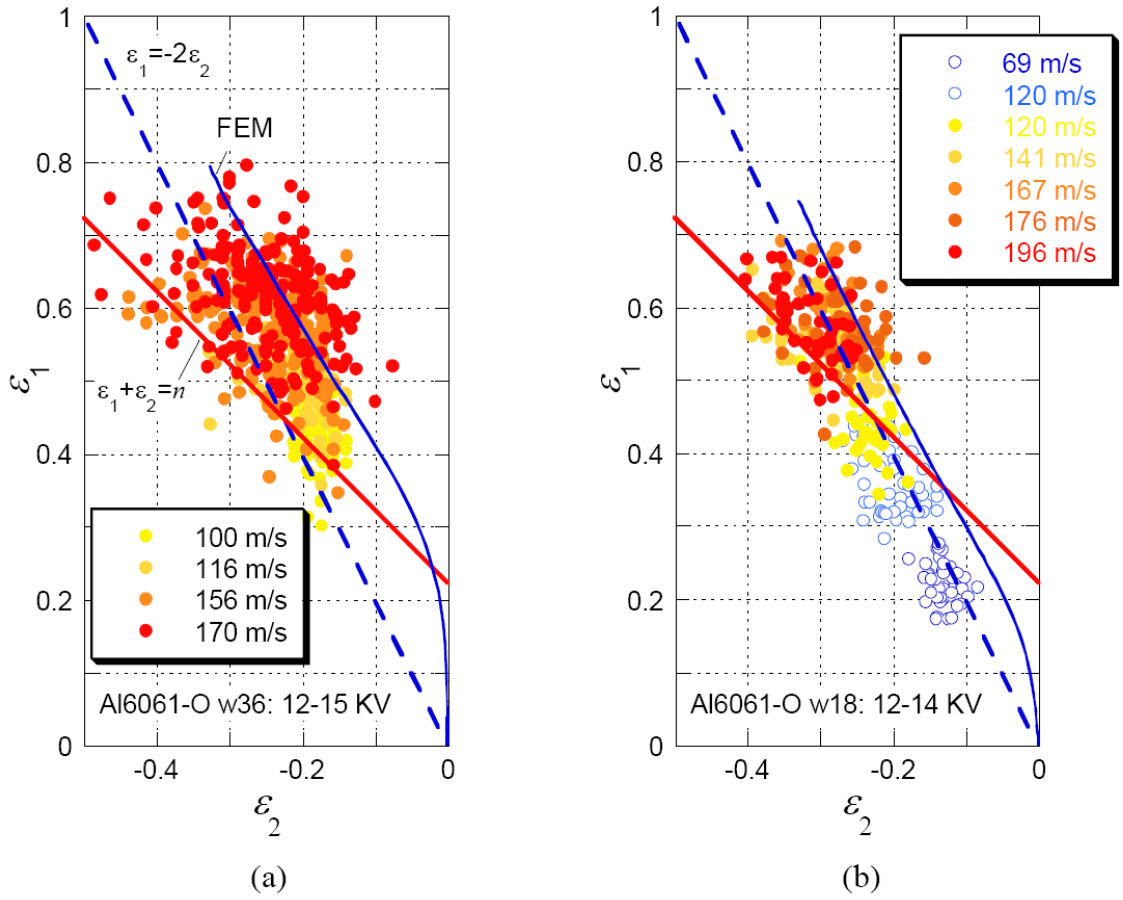

Figure 3.13 Forming limit diagrams for bare Al 6061-O a) 36 mm wide tubes; and b) 18mm wide tubes. *Open circular symbols* correspond to principal strains measured from regions where no localization is observed, and the *filled circular symbols* correspond to regions where localization is observed. The *blue dashed line* indicates the uniaxial path $\epsilon_1 = -2\epsilon_2$, and the *dashed line* indicates the quasi-static forming limit $\epsilon_1 + \epsilon_2 = n$ based on maximum tension criteria[10]

[10] Zhang H, Ravi-Chandar K (2010) On the dynamics of necking and fragmentation: IV. Expansion of Al 6061-O tubes. Int J Fract 163:56. Fig. 10

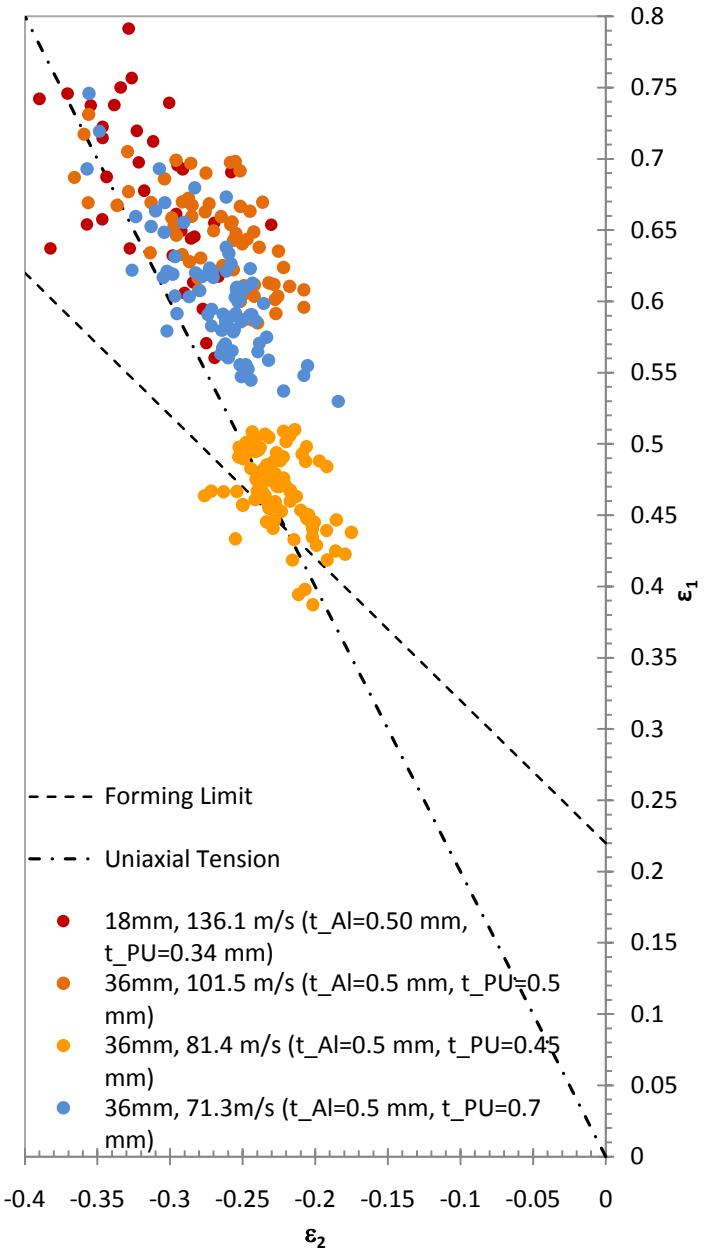

Figure 3.14 Dynamic Forming Limit diagram for Polyurea coated Al 6061-O samples. *Open circular symbols* correspond to principal strains measured from regions where no localization is observed, and the *filled circular symbols* correspond to regions where localization is observed. The *dash-dot line* indicates the uniaxial path $\epsilon_1 = -2\epsilon_2$, and the *dashed line* indicates the quasi-static forming limit $\epsilon_1 + \epsilon_2 = n$ based on maximum tension criteria

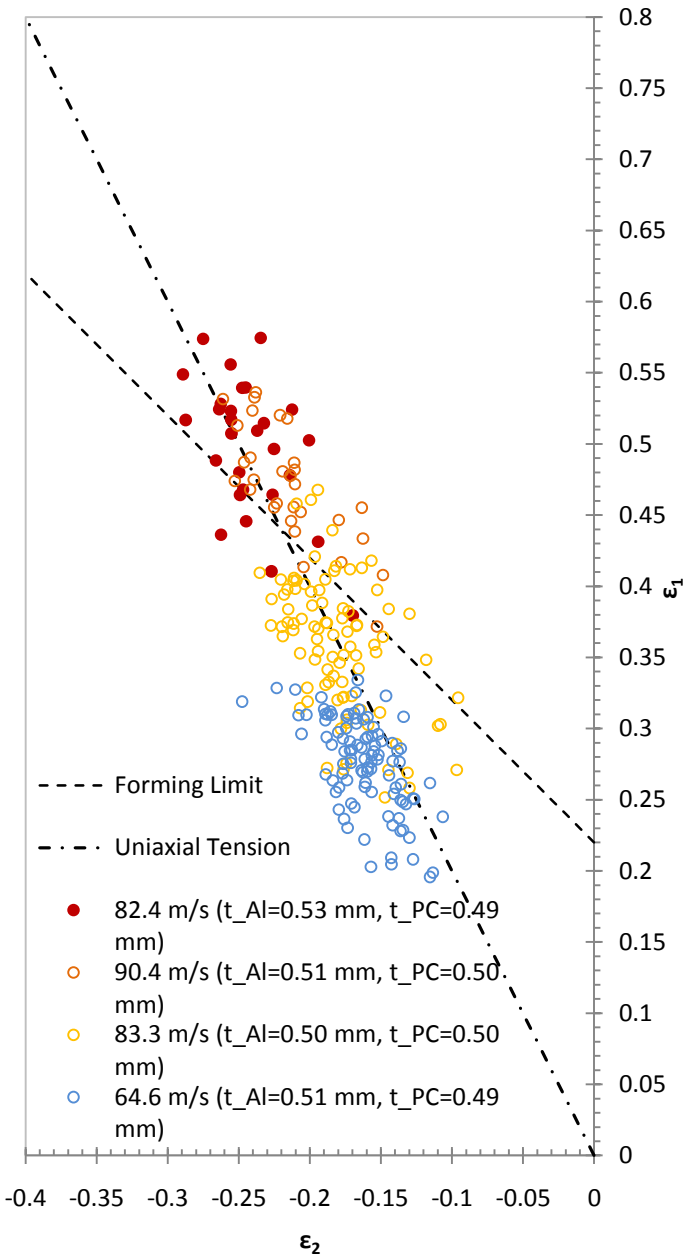

Figure 3.15 Dynamic Forming Limit diagram for Polycarbonate coated Al 6061-O samples. *Open circular symbols* correspond to principal strains measured from regions where no localization is observed, and the *filled circular symbols* correspond to regions where localization is observed. The *dash-dot line* indicates the uniaxial path $\epsilon_1 = -2\epsilon_2$, and the *dashed line* indicates the quasi-static forming limit $\epsilon_1 + \epsilon_2 = n$ based on maximum tension criteria

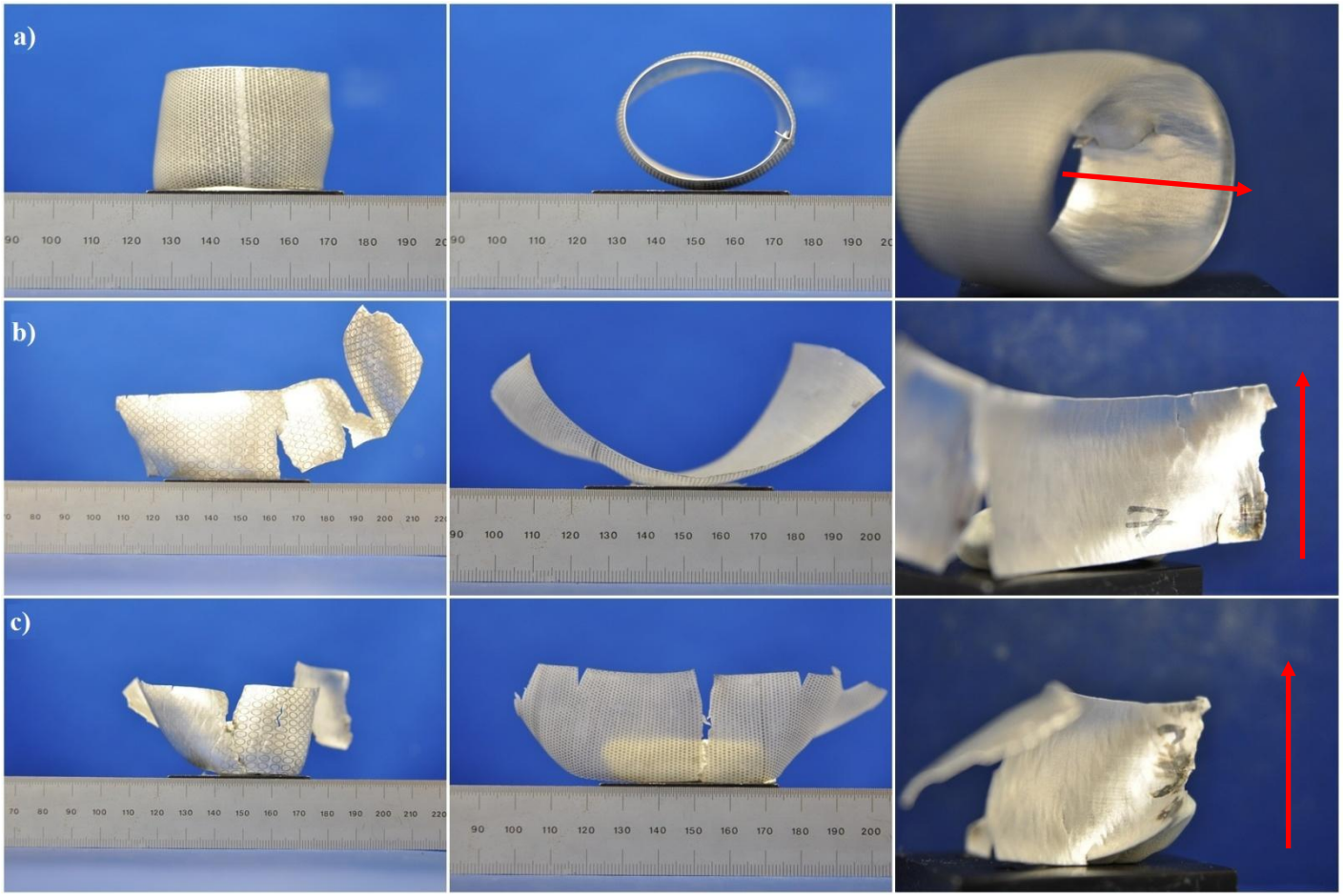

Figure 3.16 Post-mortem imaging of 36 mm polycarbonate coated Al 6061-O tubes. Row a) corresponds to PC-5, b) corresponds to PC-6 and c) displays images for PC-7. Note how all samples show clearly uniform longitudinal banding on their inside surface, as seen in the images of the third column. The red arrows show the longitudinal axis direction for the specimens.

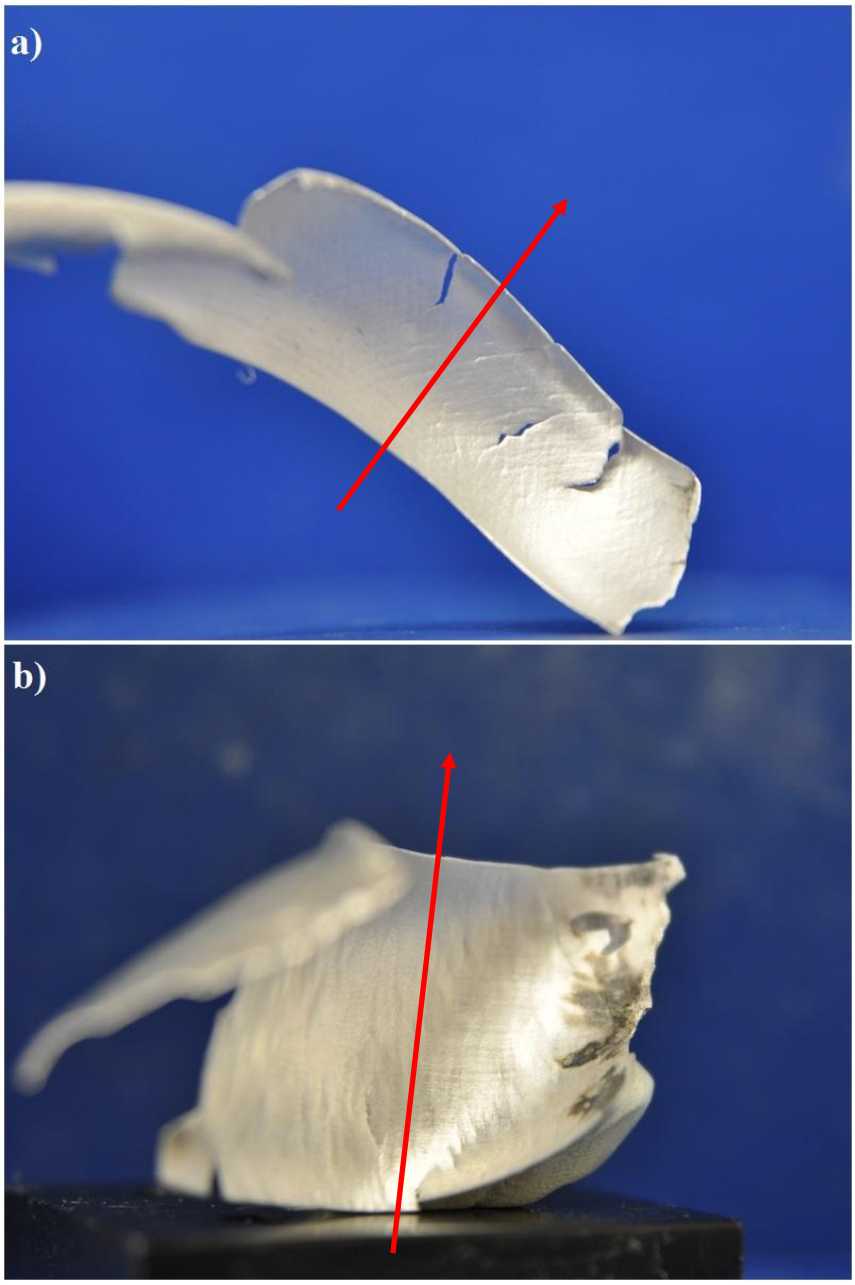

Figure 3.17 Comparison of fragments from 36 mm tubes. Image a) Shows a fragment from a polyurea coated Al 6061-O sample and b) presents a fragment from a polycarbonate coated Al 6061-O tube. Note how the top fragment presents shear localization bands, clearly defined on the inside surface of the fragment, while the bottom specimen presents clearly visible longitudinal banding on the same surface. The red arrows show the longitudinal axis direction for the specimens.

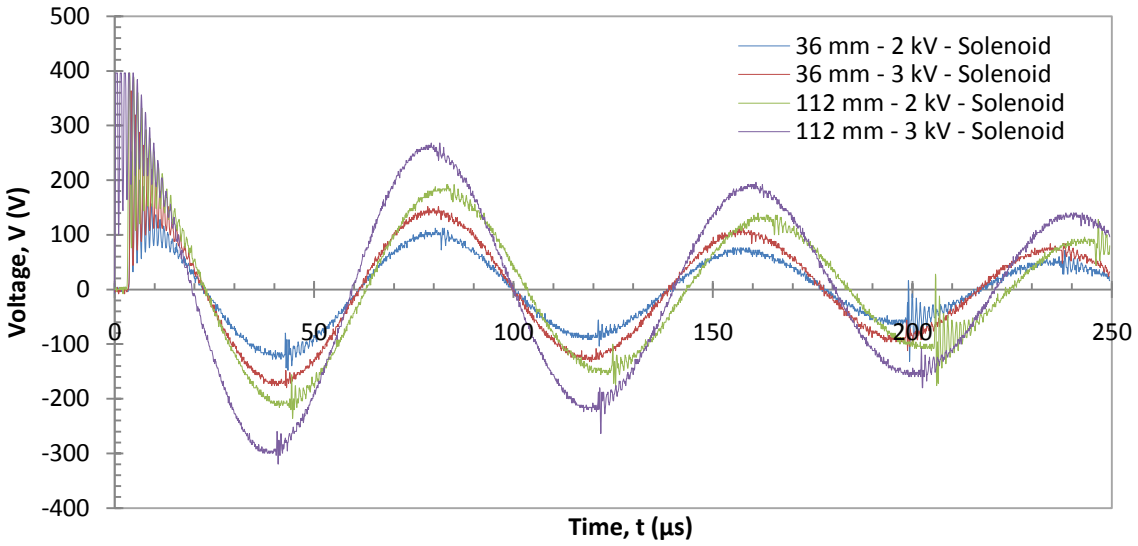

Figure 3.18 Comparison of Rogowski coil output from a current measurement through a solenoid subjected to a discharge pulse from an RLC circuit corresponding to the expanding tube experiment, without a sample in place. Two coils were analyzed: 36 mm long solenoid and a 112 mm long solenoid. The discharge pulses used were 2 and 3 kV.

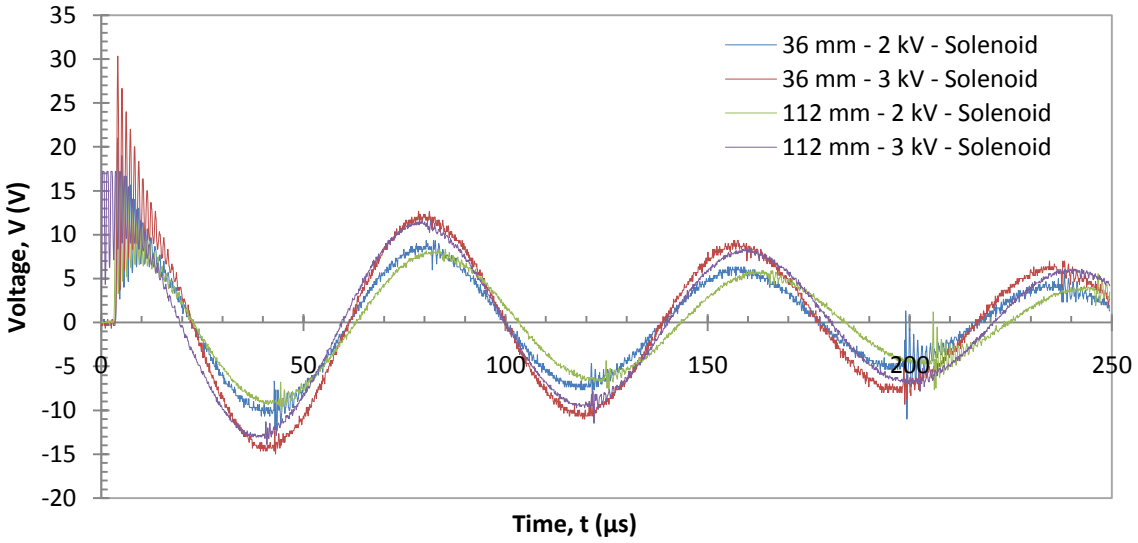

Figure 3.19 Comparison of Rogowski coil output for a single solenoid loop when measuring the current through the solenoid during a discharge pulse from an RLC circuit corresponding to the expanding tube experiment, without a sample in place. Two coils were analyzed: 36 mm long solenoid and a 112 mm long solenoid. The discharge pulses used were 2 and 3 kV.

Table 3. List of high speed, plane strain expanding tube tests on bare Al 6061-O samples

Test number	Tube length (mm)	Charging voltage (kV)	Tube thickness (mm)	Expansion velocity (m/s)[a]	Strain rate (s^-1)
PS-1	50	8	0.36	15.5	1016
PS-2	50	10	0.35	33.7	2210
PS-3	50	10	0.51	45.4	2977
PS-4	70	13	0.52	65.2	4275
PS-5	90	16	0.53	90.1	5908

[a] The steady ring expansion speed reached in the 15-50μs interval is quoted.

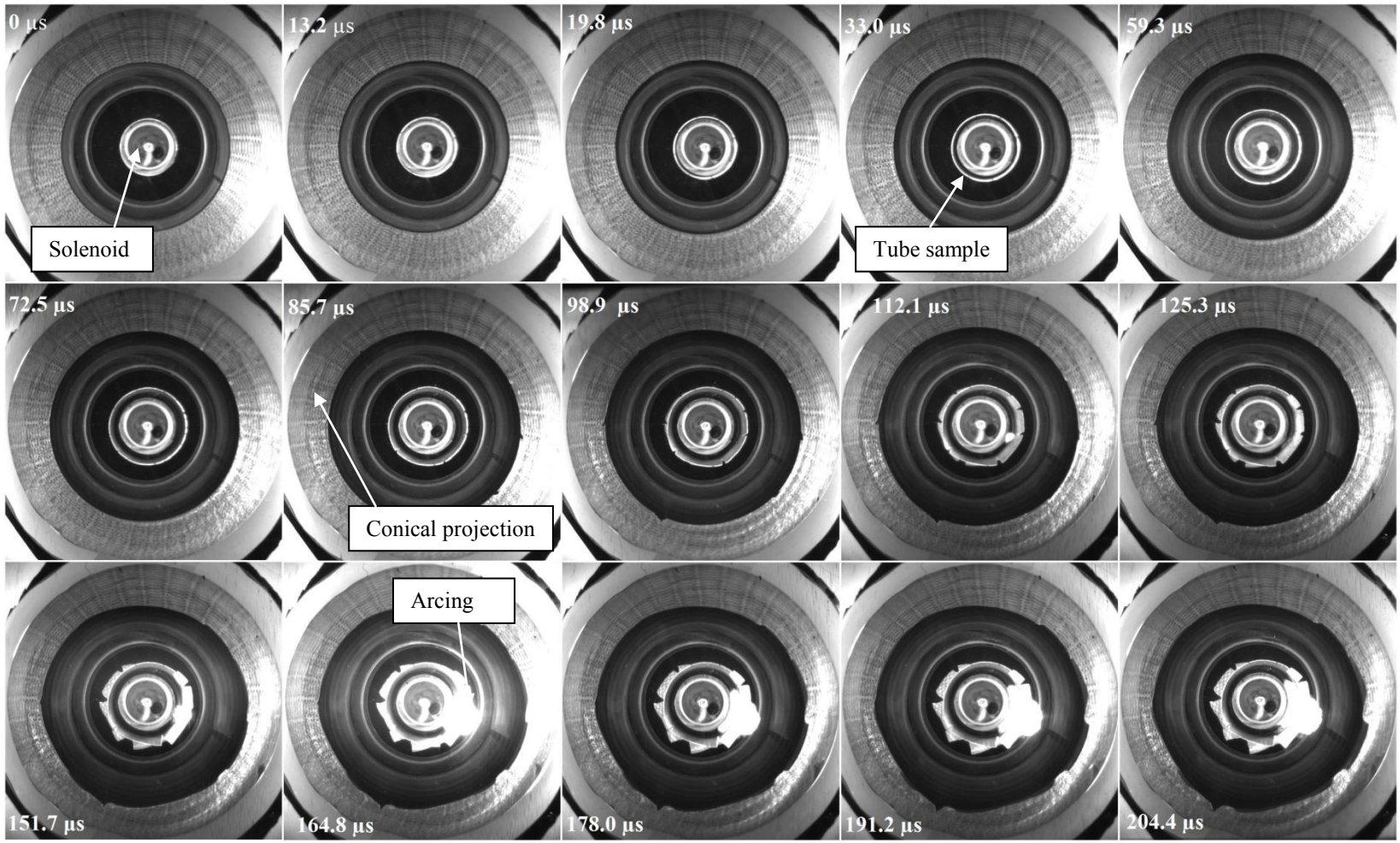

Figure 3.20 High speed images showing expansion of an Al 6061-O tube (w = 90 mm), expanding at 90.1 m/s (Test PS-5)

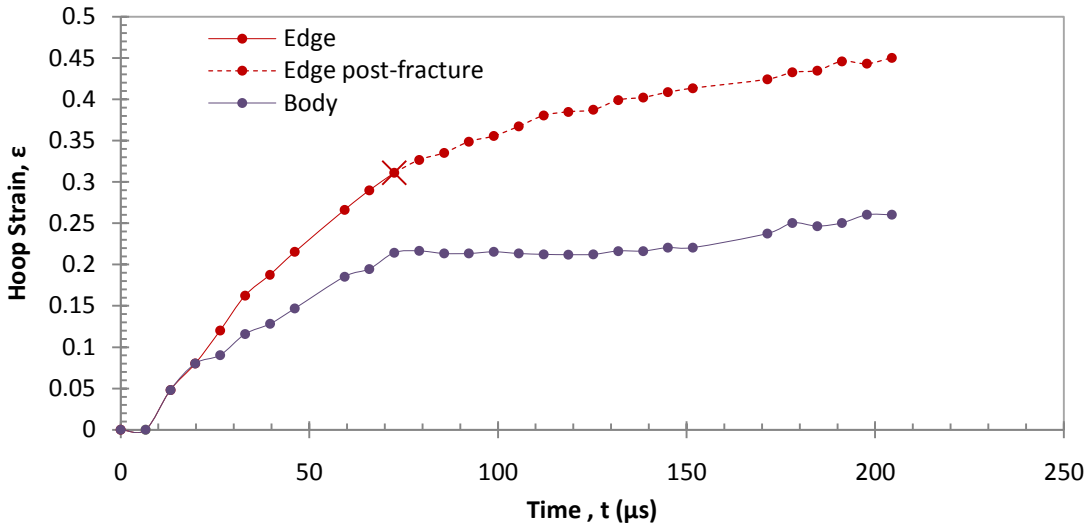

Figure 3.21 Variation of average global hoop strain with time for test PS-5: the *body* measurements correspond to the variation of average tube radius at the middle of the specimen, lengthwise; the *edge* hoop strain correspond to measurements of the variation of average tube radius at the edge of the specimen. The X marks the fracture point.

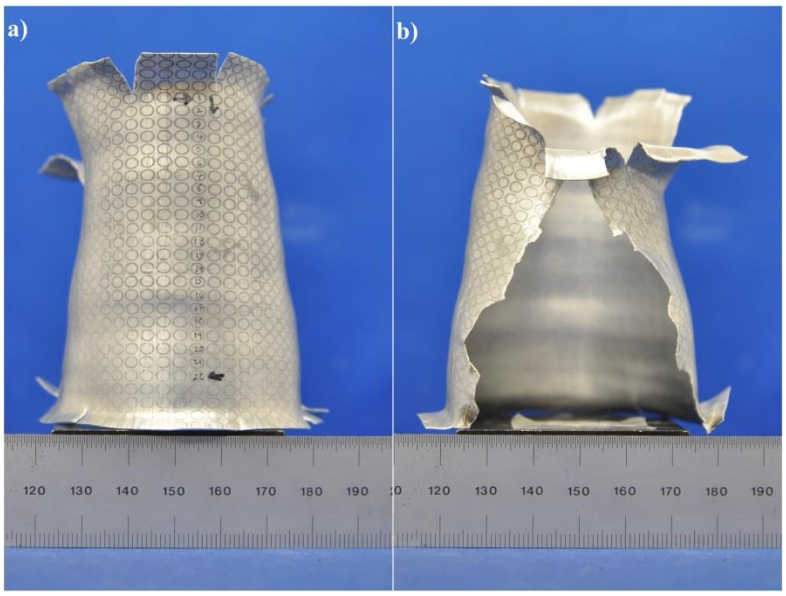

Figure 3.22 *Post mortem* photographs of the PS-5 specimen, a) front and b) back. Note the presence of flaring at the edges of the sample and a oscillatory profile of the main body.

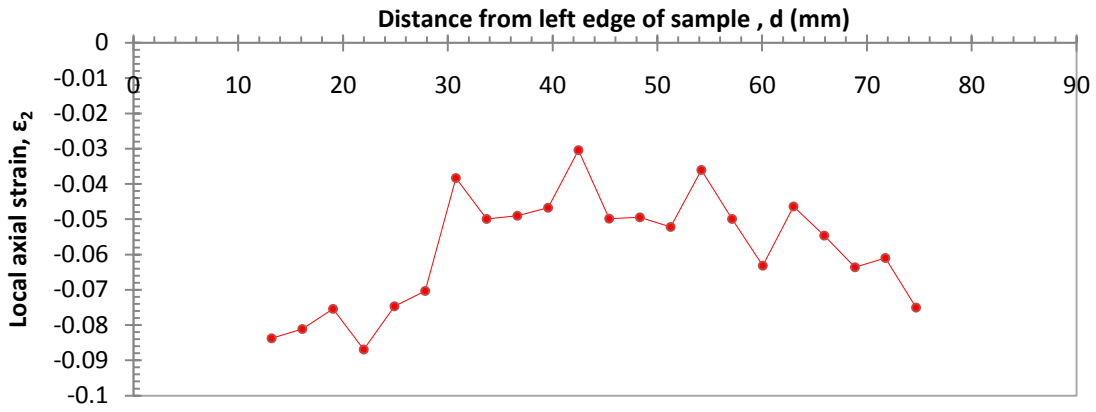

Figure 3.23 Variation of axial local strain along the length of the PS-5 specimen. All points were obtained from measurements of the deformation of a series of etched circles on the sample surface, spanning the entire length of the sample. Note the oscillatory tendency of the strains along the length of the sample.

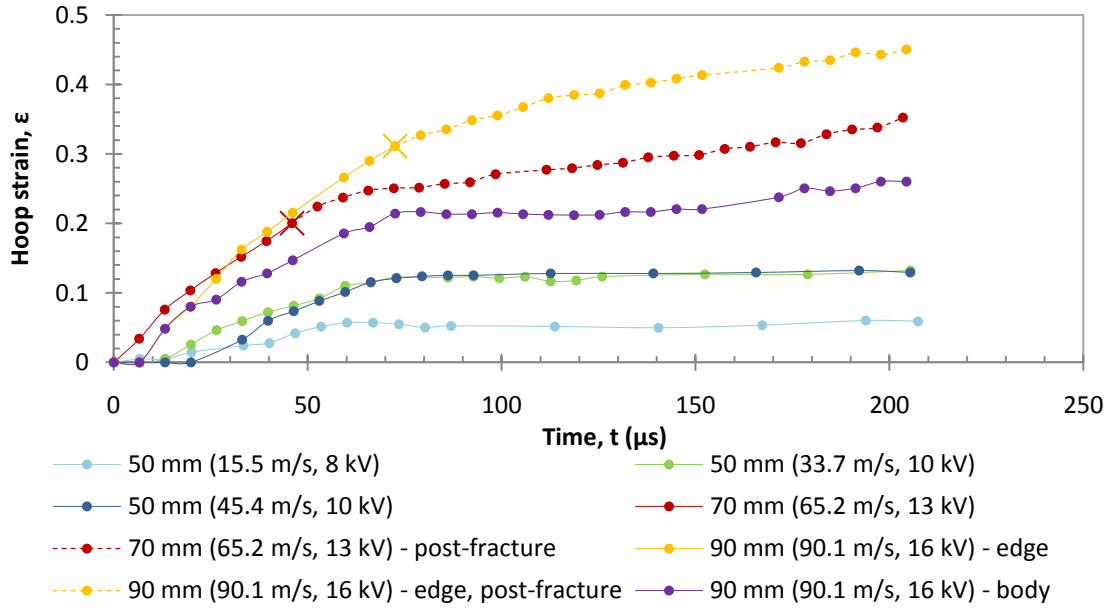

Figure 3.24 Variation of global hoop strain with time for uncoated Al 6061-O in lengths of 50, 70 and 90 mm. Note the 'rigid body' expansion observed in all the fractured specimens. The samples that did not fracture hit a plateau after the driving force was extinguished. The X marks the fracture point. Also observe that for the 90 mm sample, the edge of the specimen behaves differently from the main body.

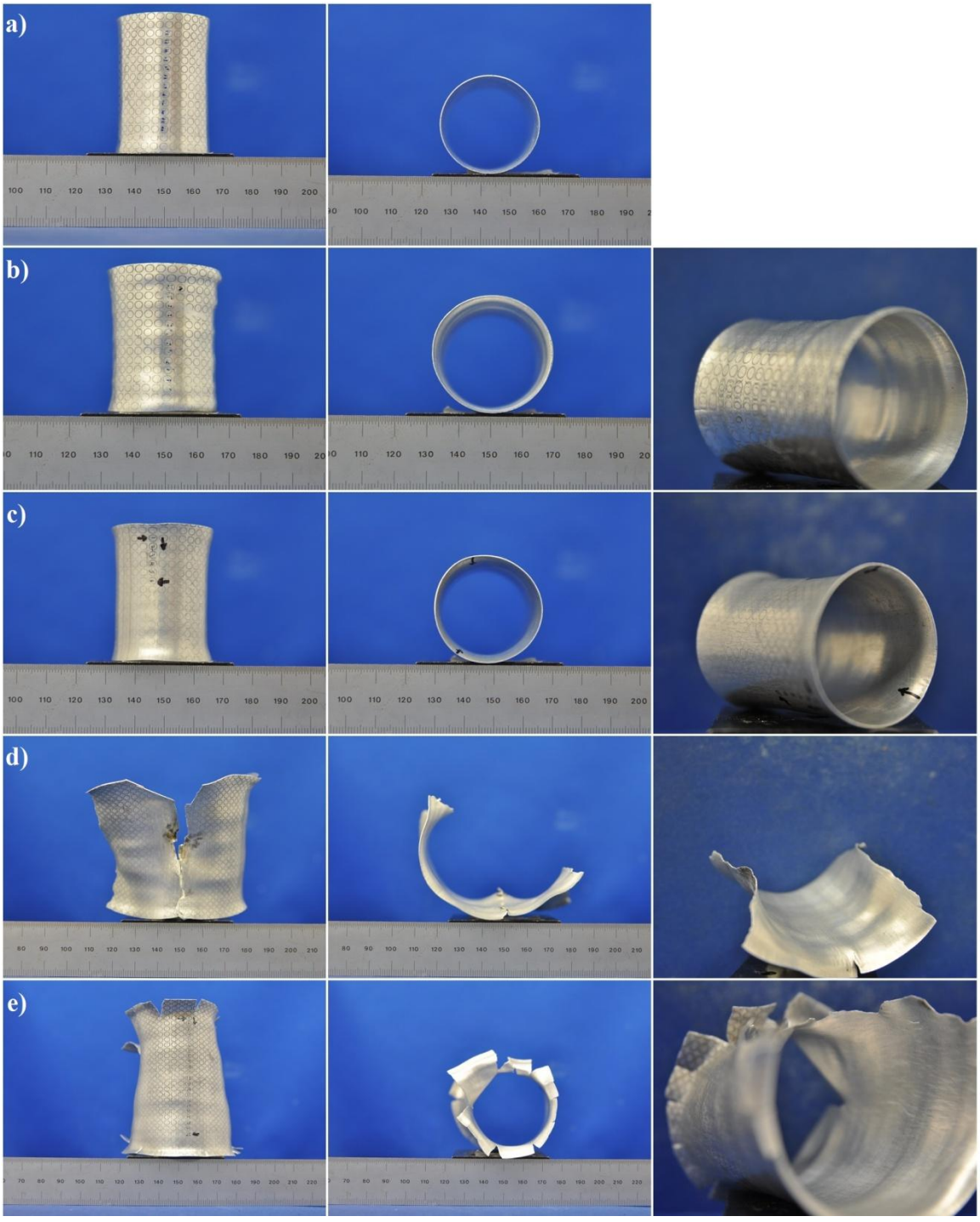

Figure 3.25 *Post mortem* photographs of a) PS-1, b) PS-2, c) PS-3, d) PS-4 and e) PS-5 specimens. The third column shows the presence of longitudinal banding on all samples except PS-1.

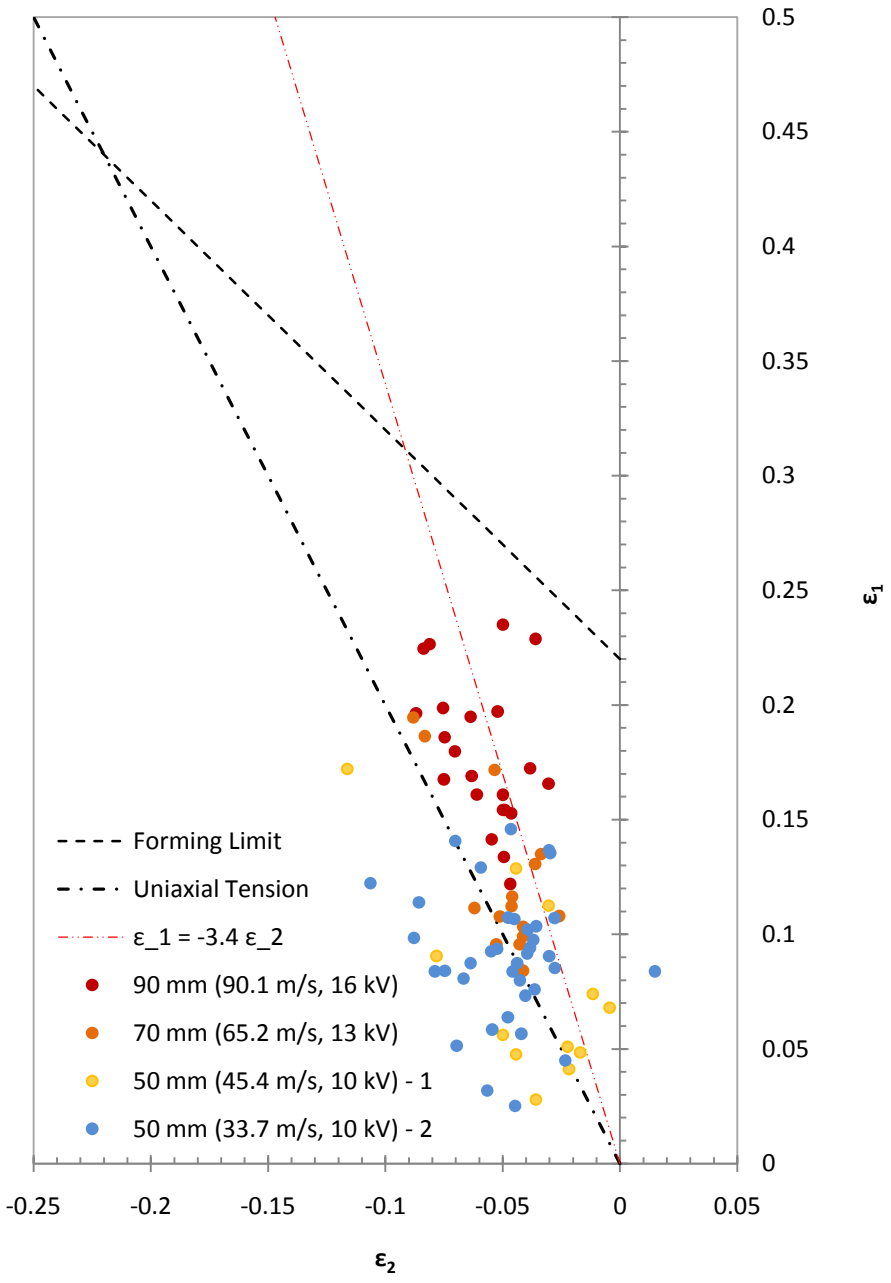

Figure 3.26 Dynamic Forming Limit diagram for 50, 70 and 90 mm long bare Al 6061-O tube samples. *Circular symbols* correspond to principal strains measured at several locations on the sample surface. The *dash-dot line* indicates the uniaxial path $\epsilon_1 = -2\epsilon_2$, the *dashed line* indicates the quasi-static forming limit $\epsilon_1 + \epsilon_2 = n$ based on maximum tension criteria and the *red dash-dot-dot line* indicates the uniaxial path $\epsilon_1 = -3.4\epsilon_2$

Table 4. List of flat plate acceleration tests on bare Al 6061-O and steel samples

Test number	Material	Side length (mm)	Plate thickness (mm)	Sample weight (g)	Charging voltage (kV)	Expansion velocity (m/s)[a]
FC-1	Al 3003 H14	30	0.394	0.975	8	251.0
FC-2	Steel	30	0.50	3.719	8	45.3
FC-3	Al 3003 H14	65	0.394	4.513	8	160.3

[a] The steady speed reached in the 15-50μs interval is quoted.

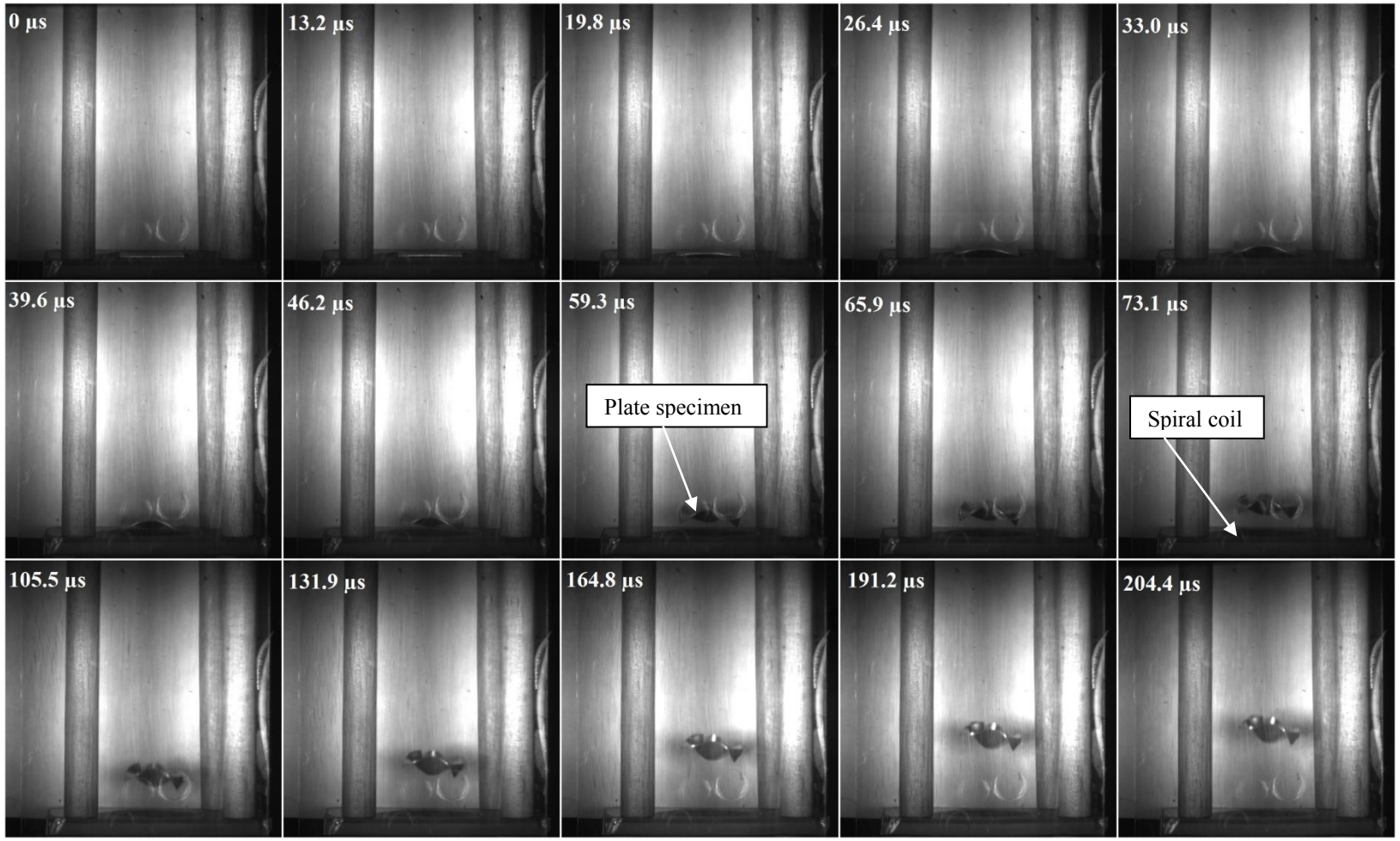

Figure 3.27 High speed images showing the displacement of a Al 3003 H14 plate (30 x 30 x 0.394 mm), moving at a speed of 251 m/s (Test FC-1)

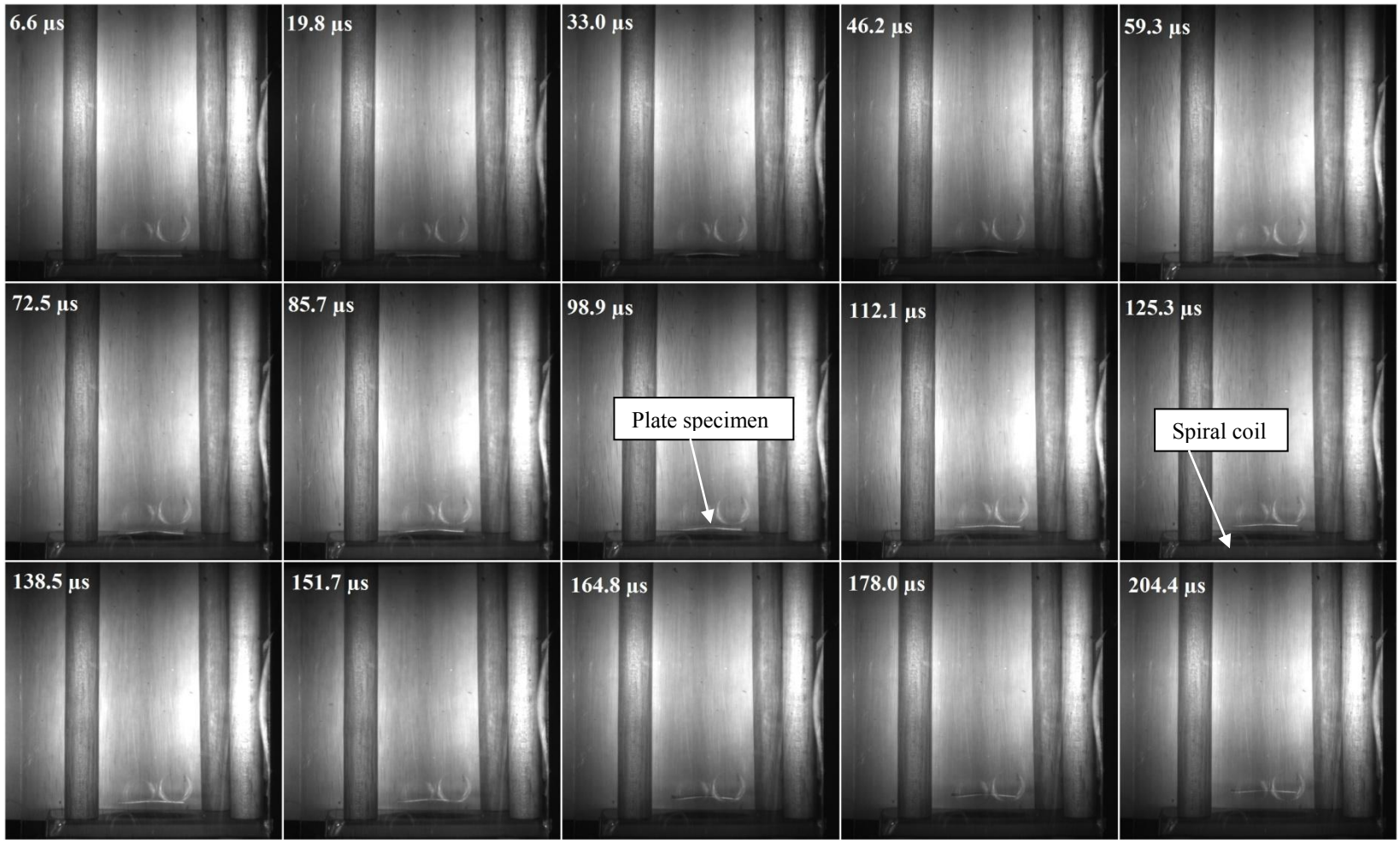

Figure 3.28 High speed images showing the displacement of a Steel plate (30 x 30 x 0.5 mm), moving at a speed of 45.3 m/s (Test FC-2)

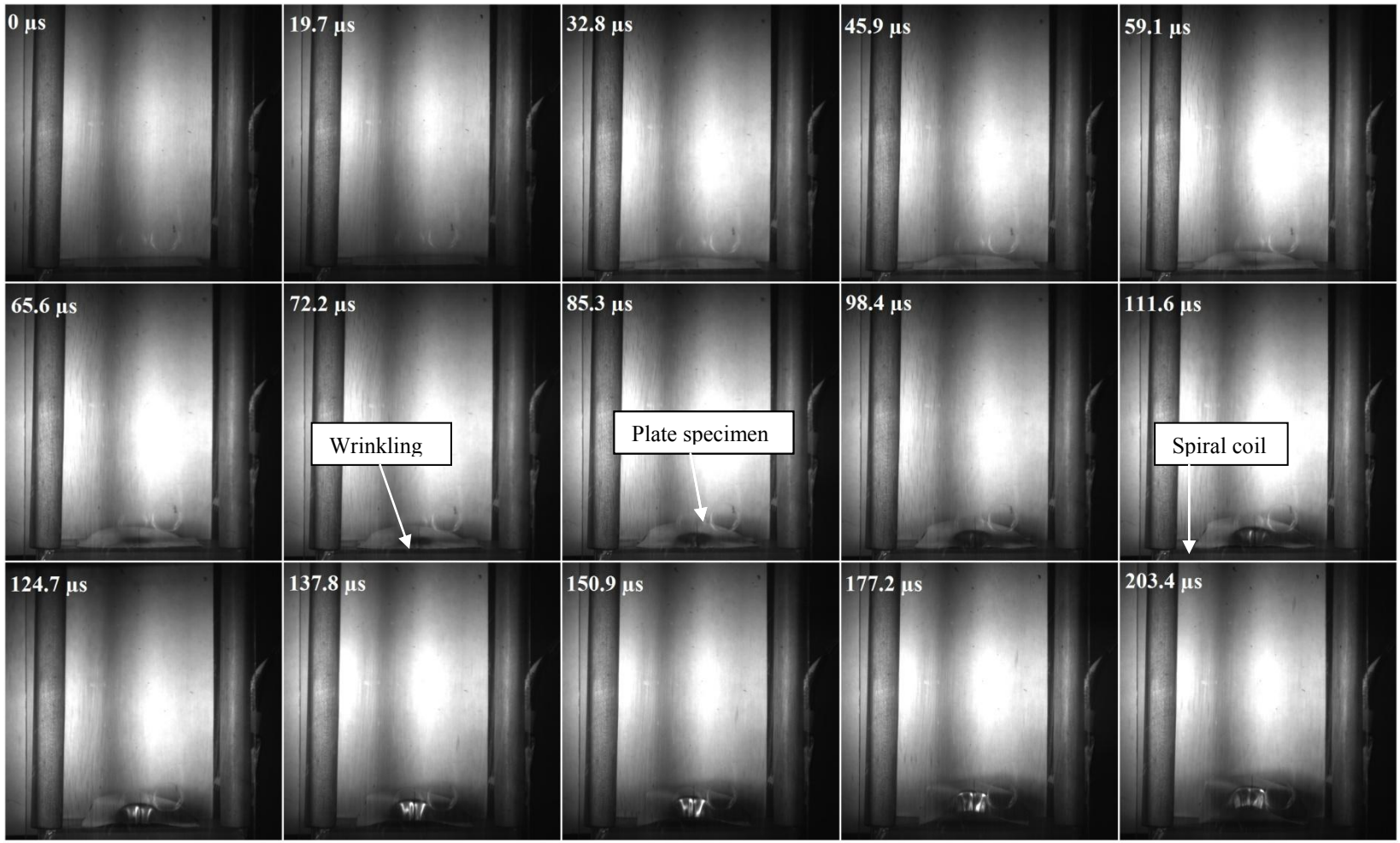

Figure 3.29 High speed images showing the displacement of a Al 3003 H14 plate (65 x 65 x 0.394 mm), moving at a speed of 160.3 m/s (Test FC-1)

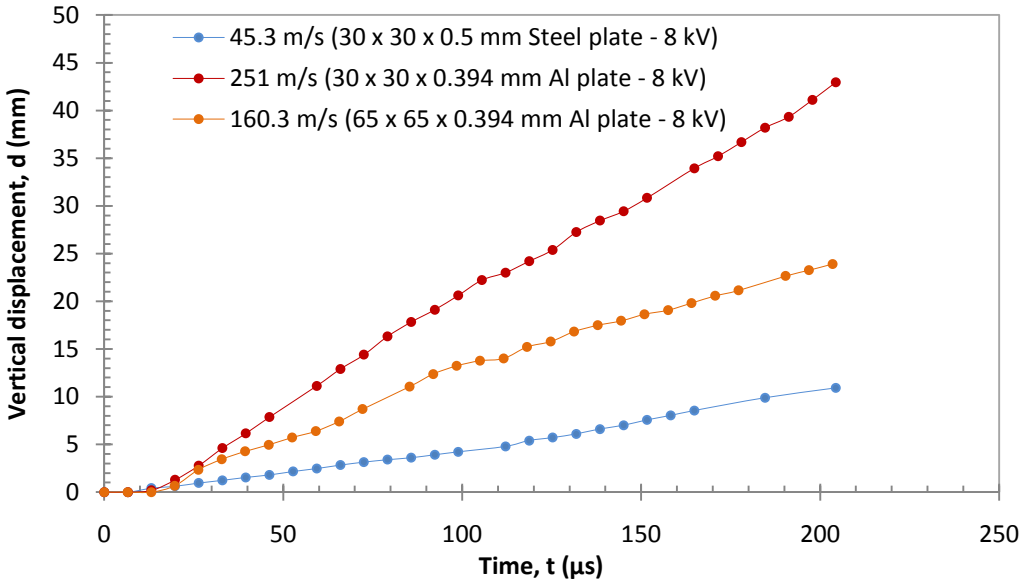

Figure 3.30 Variation of vertical displacement for flat plate specimens accelerated via spiral coil.

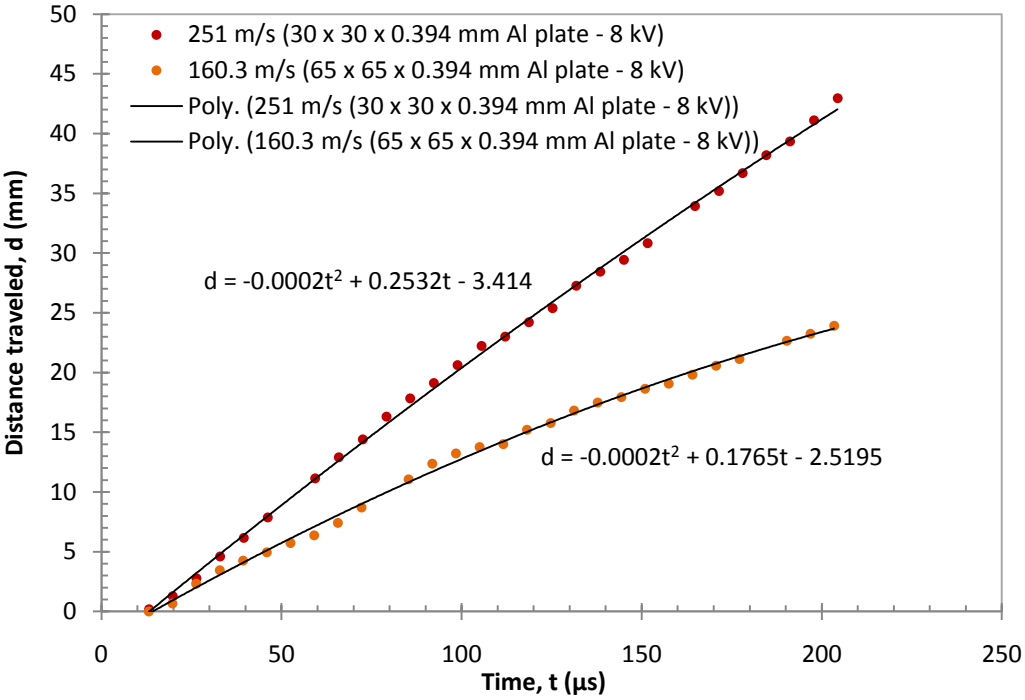

Figure 3.31 Polynomial fit of variation of vertical displacement with time for flat plate specimens FC-1 and FC-3

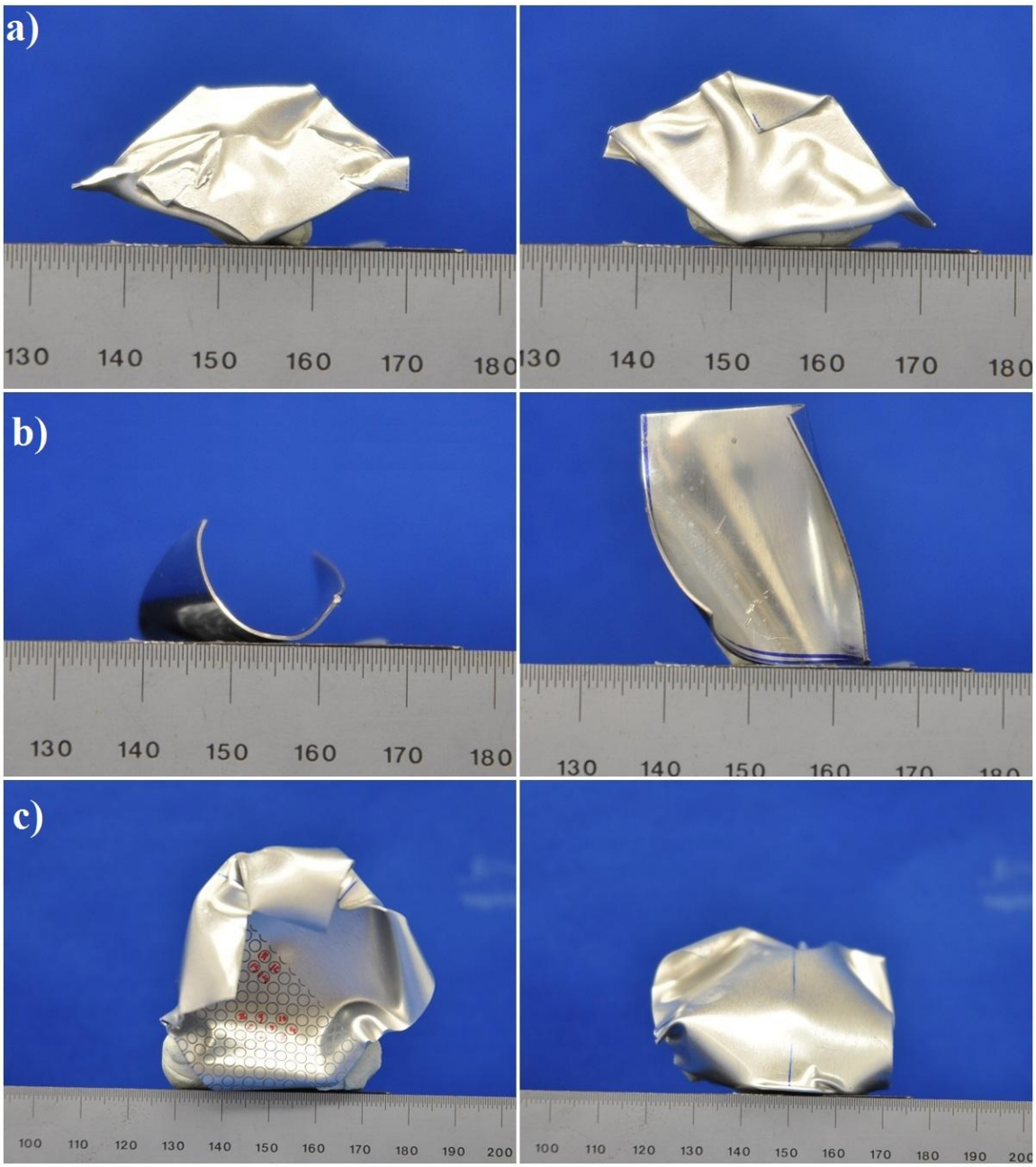

Figure 3.32 *Post mortem* photographs of a) FC-1, b) FC-2, c) FC-3 specimens. Note the *draping* observed in FC-1 and FC-3.

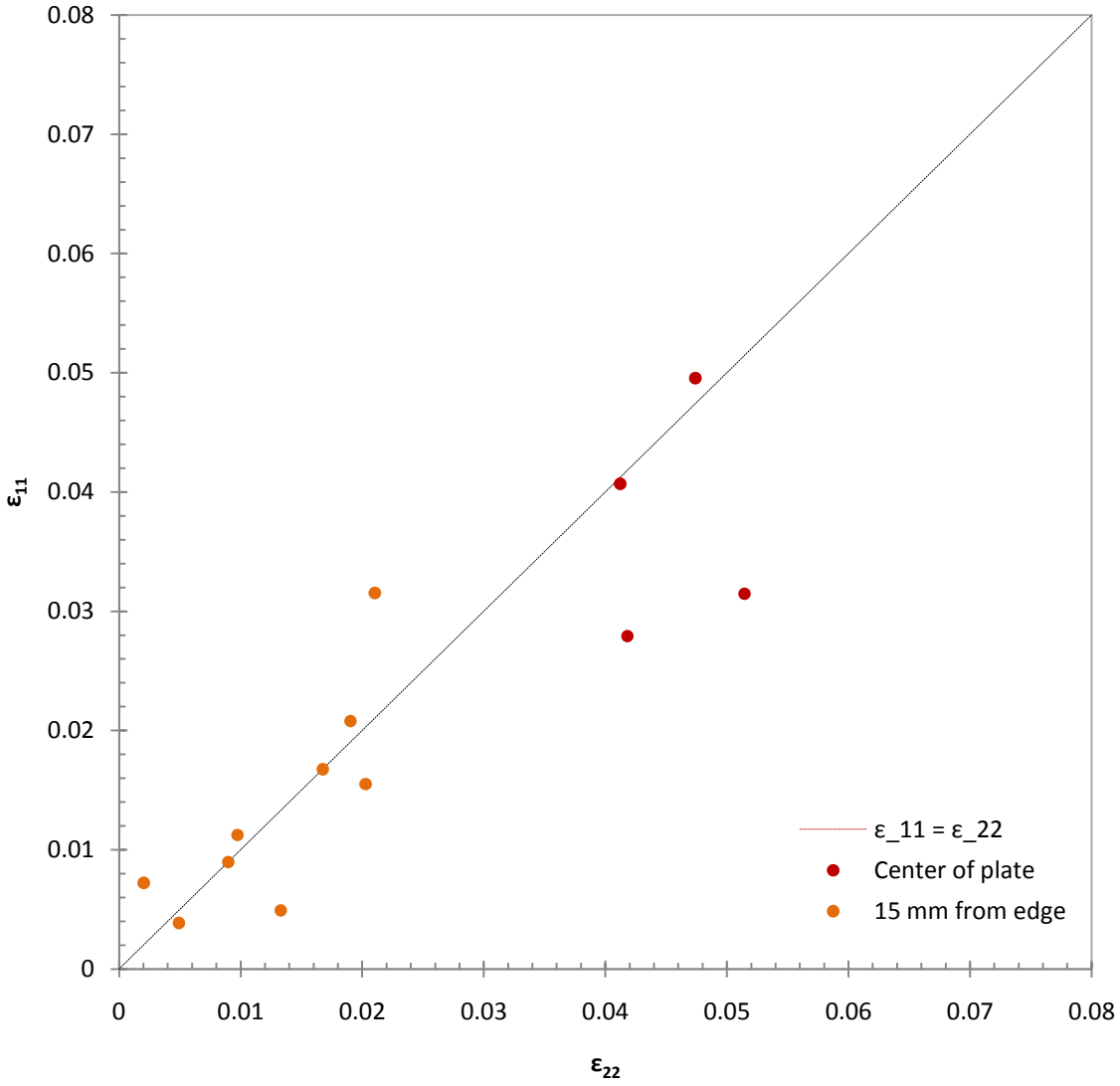

Figure 3.33 *Post mortem* local strain measurements for flat plate specimen FC-3. Data was obtained by measuring the deformation of circular markings on the surface of the sample. The *black dash line* indicates the path $\epsilon_{11} = \epsilon_{22}$, where the 11 and 22 directions correspond to the directions parallel to adjacent edges of the specimen. The orange circles were measured from an area ~15 mm from one edge of the plate; the red circles correspond to measurements from the center of the plate

Appendices

A. Engineering Drawings for Winding Mandrel, Polycarbonate Core and Machining of 112 mm Solenoid

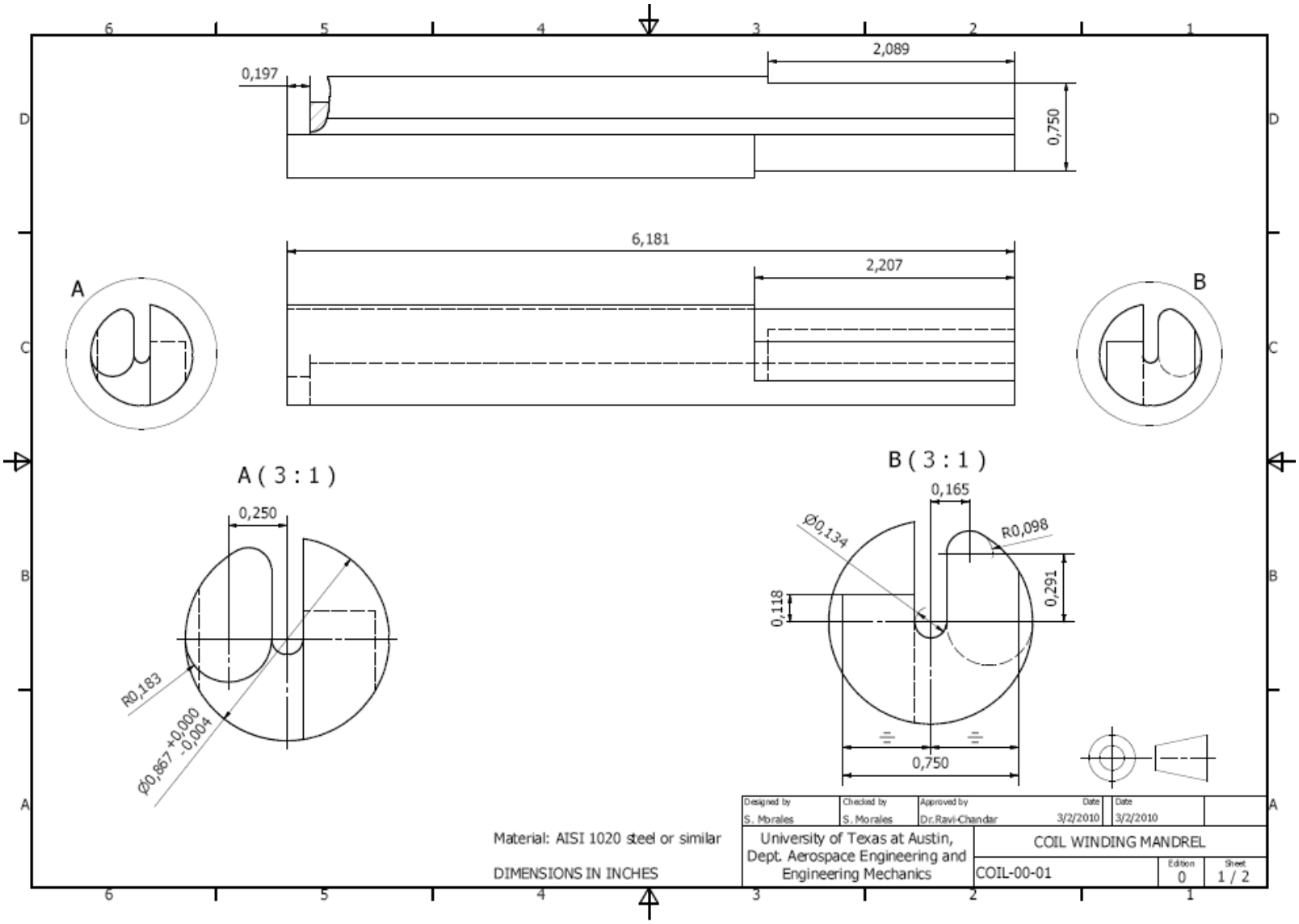
2,089
0,197
0,750
6,181
2,207
A
B
A (3 : 1)
B (3 : 1)
0,250
R0,183
Ø0,867 +0,000 -0,004
0,165
Ø0,134
R0,098
0,291
0,118
0,750
Material: AISI 1020 steel or similar
DIMENSIONS IN INCHES
Designed by S. Morales
Checked by S. Morales
Approved by Dr.Ravi-Chandar
Date 3/2/2010
Date 3/2/2010
University of Texas at Austin, Dept. Aerospace Engineering and Engineering Mechanics
COIL WINDING MANDREL
COIL-00-01
Edition 0
Sheet 1 / 2

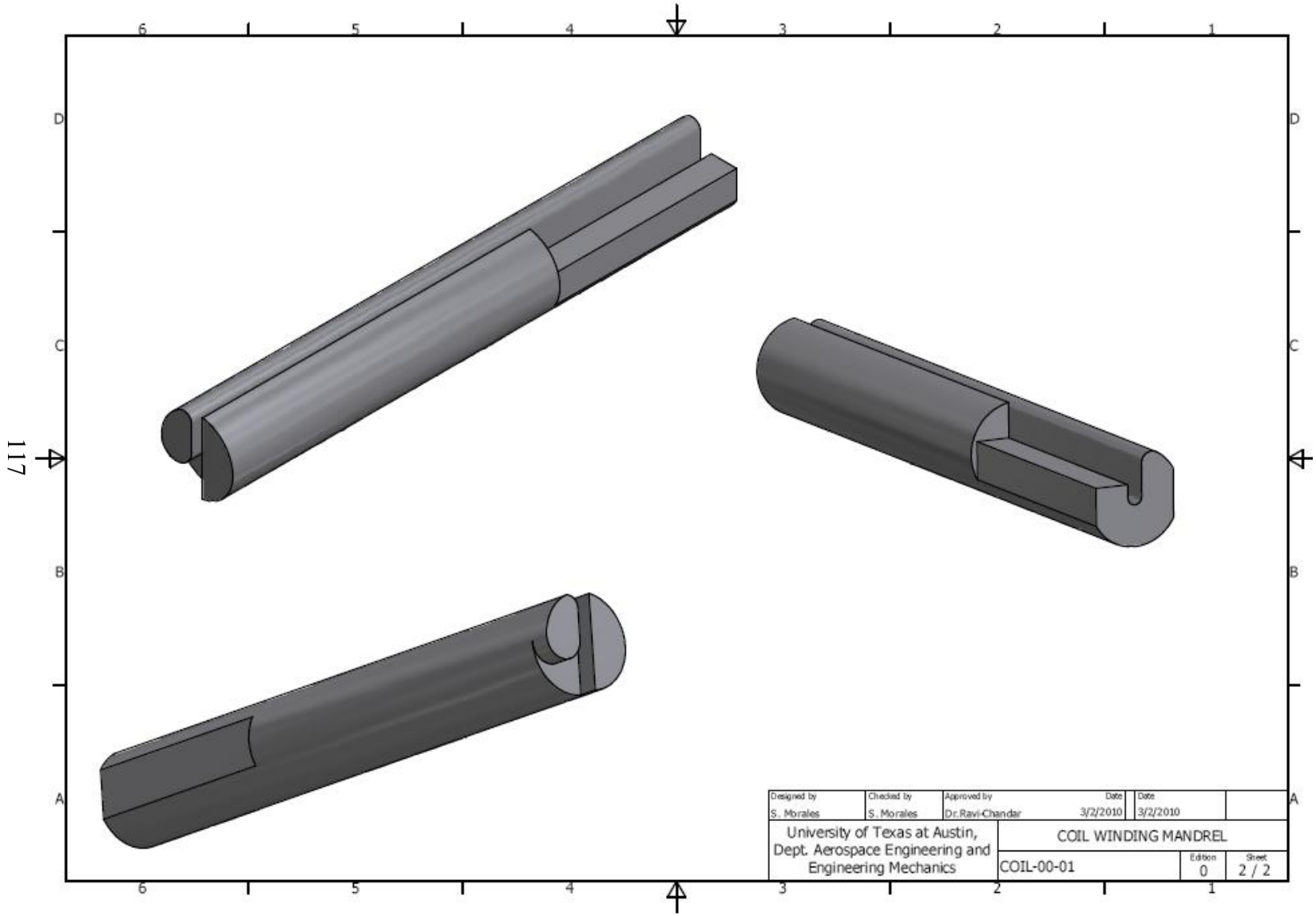
6
5
4
3
2
1
D
C
B
A
Designed by
S. Morales
Checked by
S. Morales
Approved by
Dr.Ravi-Chandar
Date
3/2/2010
Date
3/2/2010
University of Texas at Austin,
Dept. Aerospace Engineering and
Engineering Mechanics
COIL WINDING MANDREL
COIL-00-01
Edition
0
Sheet
2 / 2

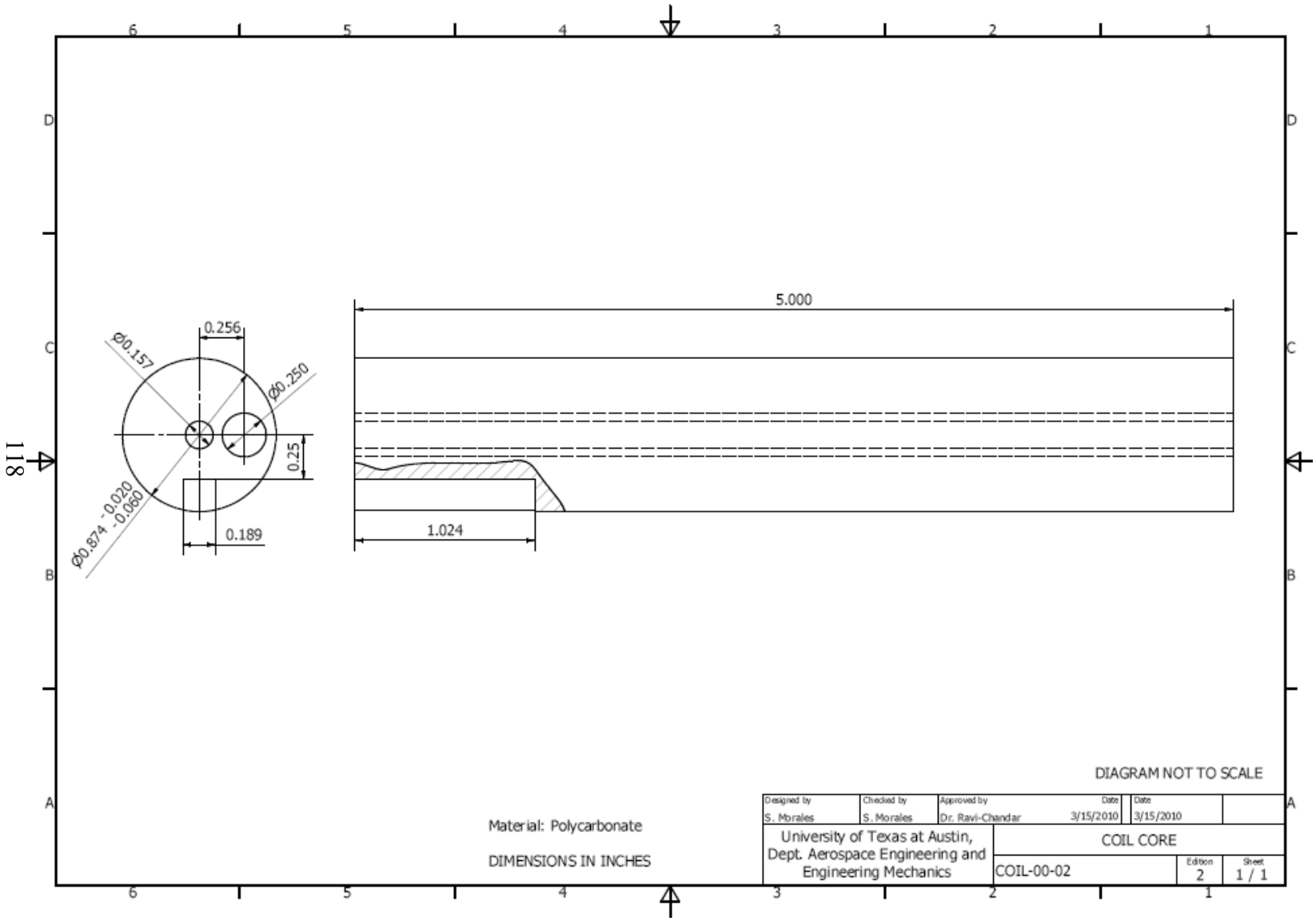
6
5
4
3
2
1
D
C
B
A
0.256
Ø0.157
Ø0.250
0.25
Ø0.874 -0.020 -0.060
0.189
5.000
1.024
DIAGRAM NOT TO SCALE
Material: Polycarbonate
DIMENSIONS IN INCHES
Designed by
S. Morales
Checked by
S. Morales
Approved by
Dr. Ravi-Chandar
Date
3/15/2010
Date
3/15/2010
University of Texas at Austin,
Dept. Aerospace Engineering and
Engineering Mechanics
COIL CORE
COIL-00-02
Edition
2
Sheet
1 / 1

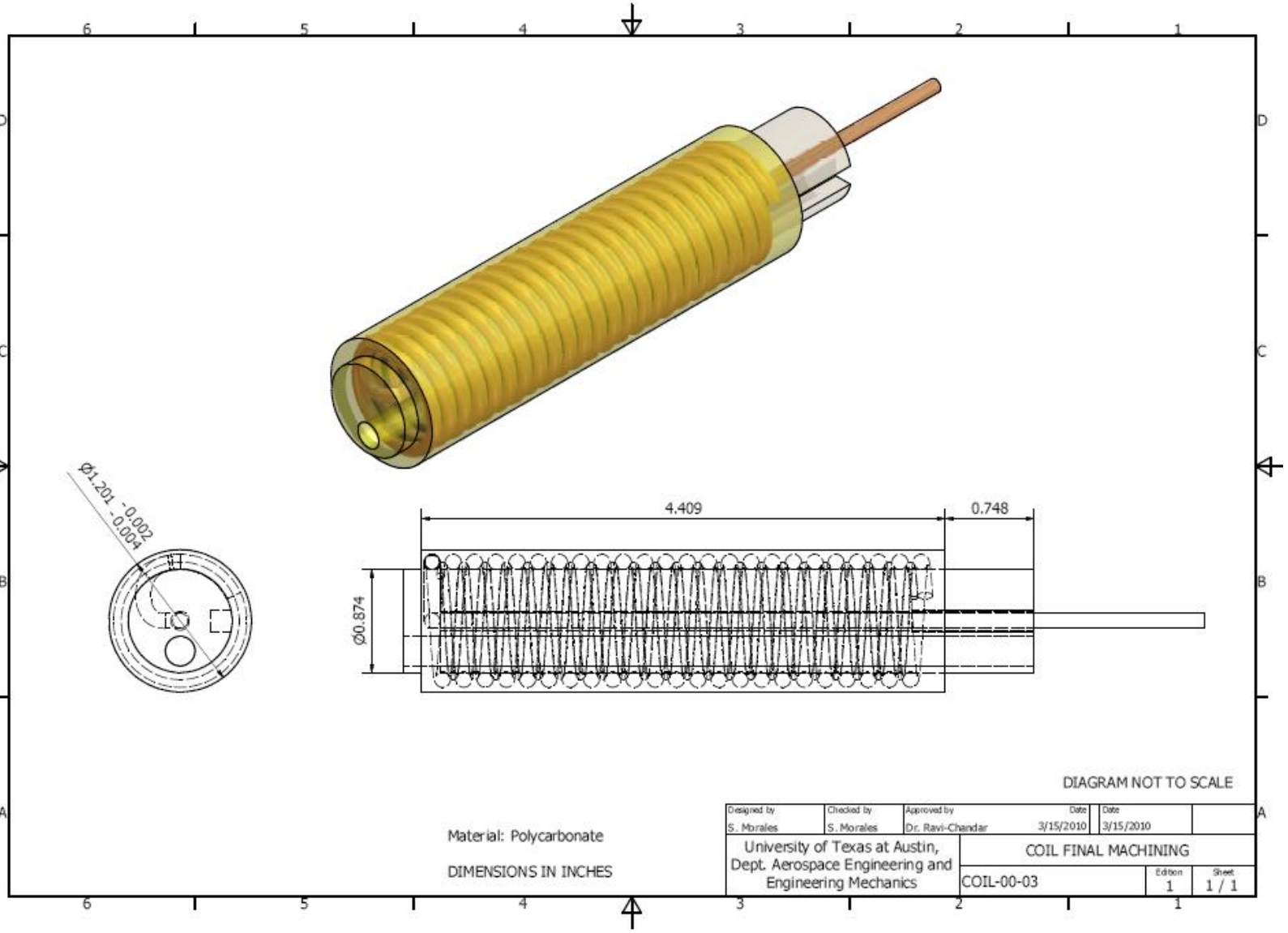
Ø1.201 -0.002
-0.004
4.409
0.748
Ø0.874
DIAGRAM NOT TO SCALE
Material: Polycarbonate
DIMENSIONS IN INCHES
Designed by
S. Morales
Checked by
S. Morales
Approved by
Dr. Ravi-Chandar
Date
3/15/2010
Date
3/15/2010
University of Texas at Austin,
Dept. Aerospace Engineering and
Engineering Mechanics
COIL FINAL MACHINING
COIL-00-03
Edition
1
Sheet
1 / 1

B. Engineering Drawings for Vertical Mold Used to Cover 112 mm Solenoid Winding in Epoxy

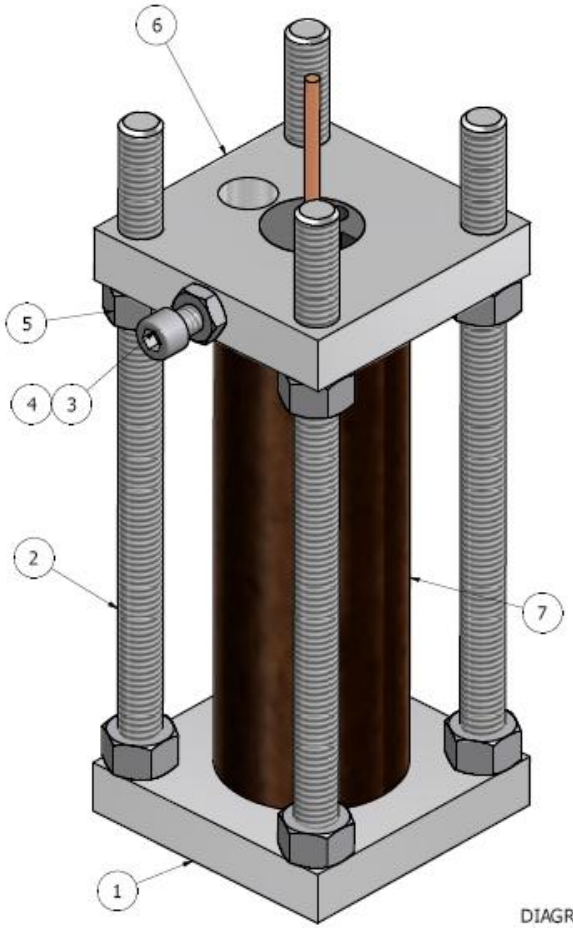

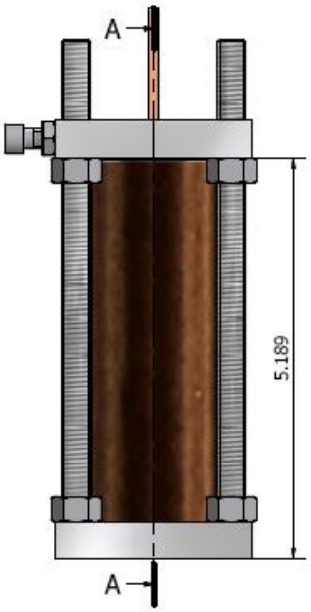

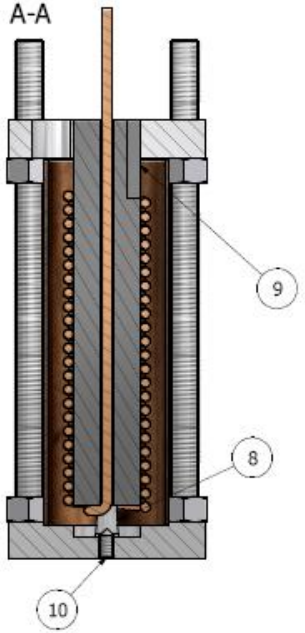

NO.	QTY.	NAME	PART NO.	NOTES
10	1	CENTERPOINT PLUG	-	CONE POINT SET SCREW - 10-24 UNC x 0.38" LONG
9	1	COIL	-	PREVIOUS ASSEMBLY
8	1	PLUG	VM-01-05	
7	1	CYLINDER	VM-01-04	EXPENDABLE COMPONENT
6	1	TOP PLATE	VM-01-03	
5	8	-	-	3/8 - HEX NUT
4	1	-	-	1/4 - HEX NUT
3	1	-	-	1/4 UNC - ALLEN BOLT - 1.25" LONG
2	4	POST ROD	VM-01-02	
1	1	BASE PLATE	VM-01-01	

Designed by	Checked by	Approved by		Date
S. Morales	S. Morales	Dr. Ravi-Chandar		5/26/2010

DIAGRAM NOT TO SCALE

DIMENSIONS IN INCHES

University of Texas at Austin, Dept. Aerospace Engineering and Engineering Mechanics

VERTICAL MOLD ASSEMBLY

Part No.	Edition	Sheet
VM-01-00	0	1 / 6

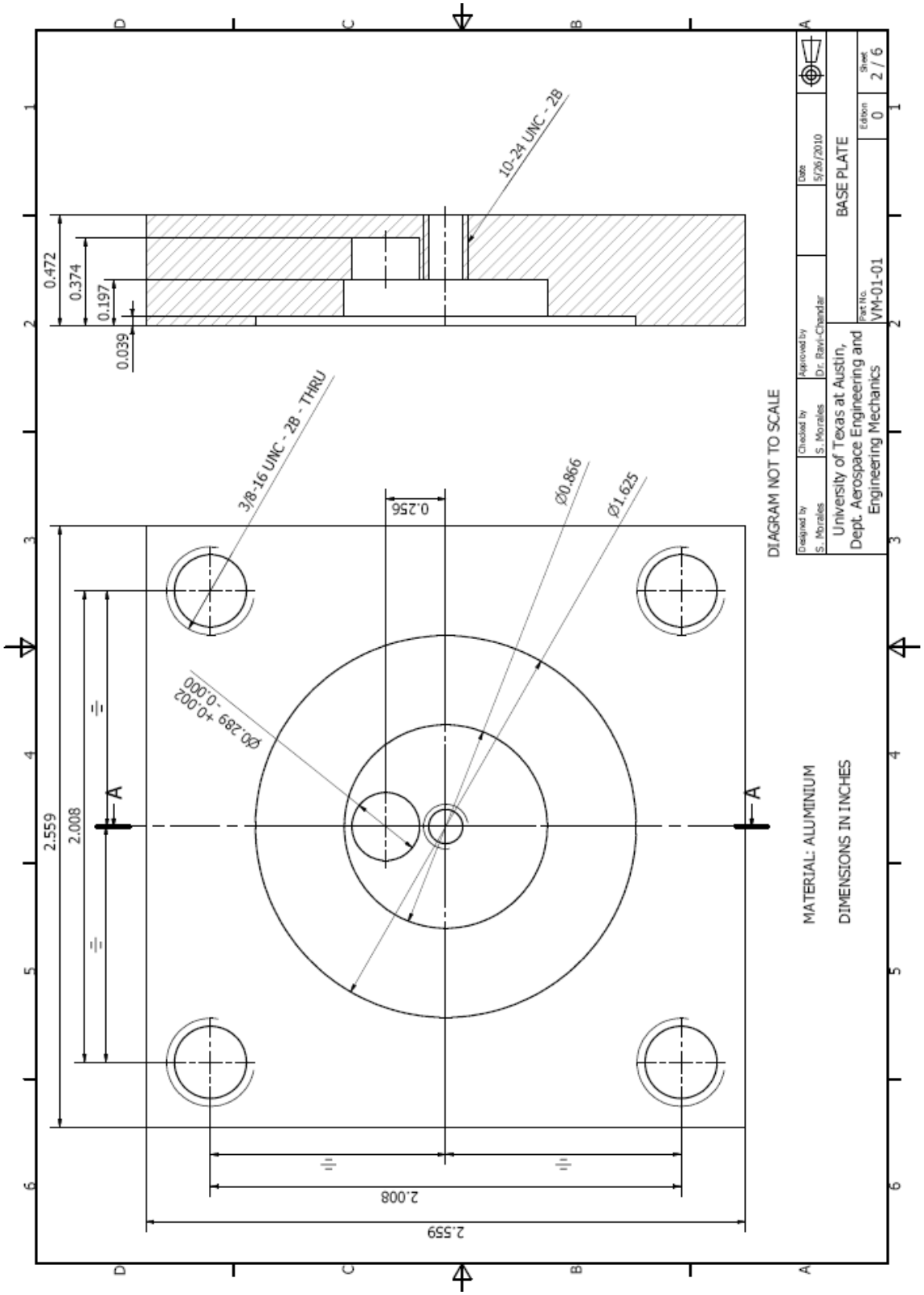
10-24 UNC - 2B
0.472
0.374
0.197
0.039
3/8-16 UNC - 2B - THRU
0.256
Ø0.866
Ø1.625
Ø0.289 +0.002 -0.000
2.559
2.008
2.008
2.559
A
A
DIAGRAM NOT TO SCALE
MATERIAL: ALUMINIUM
DIMENSIONS IN INCHES
Designed by S. Morales
Checked by S. Morales
Approved by Dr. Ravi-Chandar
Date 5/26/2010
University of Texas at Austin, Dept. Aerospace Engineering and Engineering Mechanics
BASE PLATE
Part No. VM-01-01
Edition 0
Sheet 2 / 6

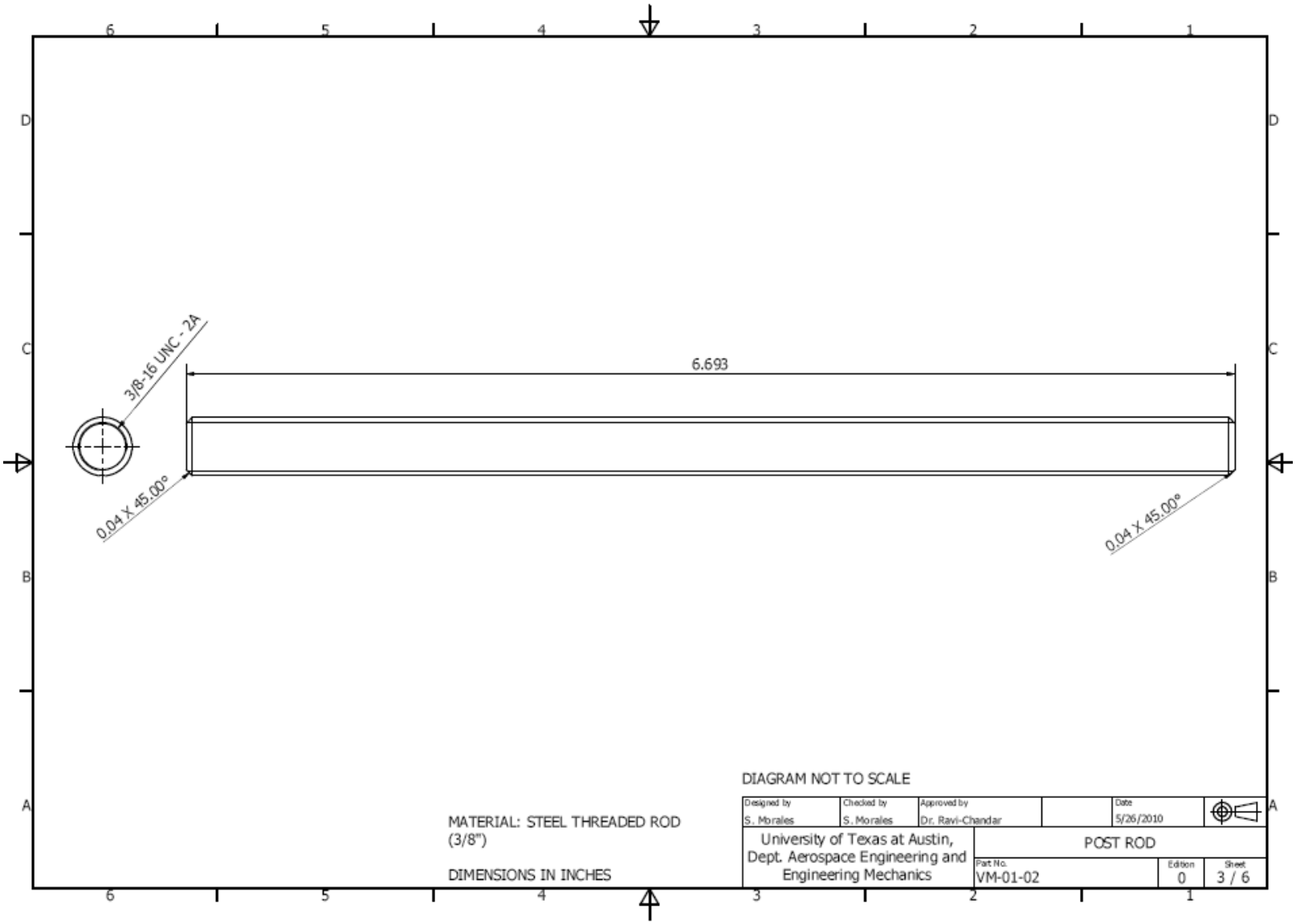
6
5
4
3
2
1
D
C
B
A
3/8-16 UNC - 2A
6.693
0.04 X 45.00°
0.04 X 45.00°
DIAGRAM NOT TO SCALE
MATERIAL: STEEL THREADED ROD
(3/8")
DIMENSIONS IN INCHES
Designed by
S. Morales
Checked by
S. Morales
Approved by
Dr. Ravi-Chandar
Date
5/26/2010
University of Texas at Austin,
Dept. Aerospace Engineering and
Engineering Mechanics
POST ROD
Part No.
VM-01-02
Edition
0
Sheet
3 / 6

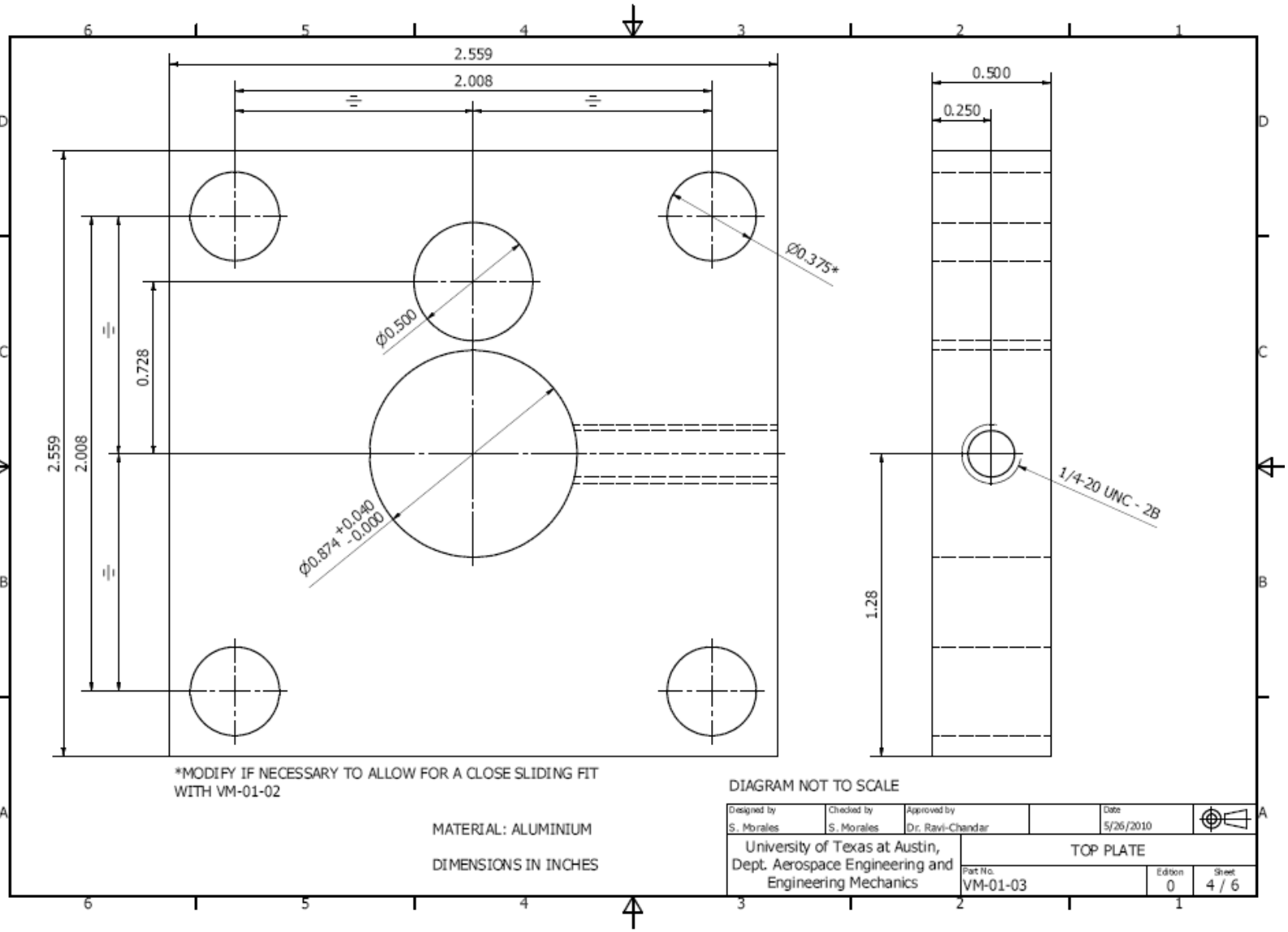
2.559
2.008
0.500
0.250
Ø0.375*
Ø0.500
0.728
2.559
2.008
Ø0.874 +0.040 -0.000
1/4-20 UNC - 2B
1.28
*MODIFY IF NECESSARY TO ALLOW FOR A CLOSE SLIDING FIT WITH VM-01-02
DIAGRAM NOT TO SCALE
MATERIAL: ALUMINIUM
DIMENSIONS IN INCHES
Designed by S. Morales
Checked by S. Morales
Approved by Dr. Ravi-Chandar
Date 5/26/2010
University of Texas at Austin, Dept. Aerospace Engineering and Engineering Mechanics
TOP PLATE
Part No. VM-01-03
Edition 0
Sheet 4 / 6

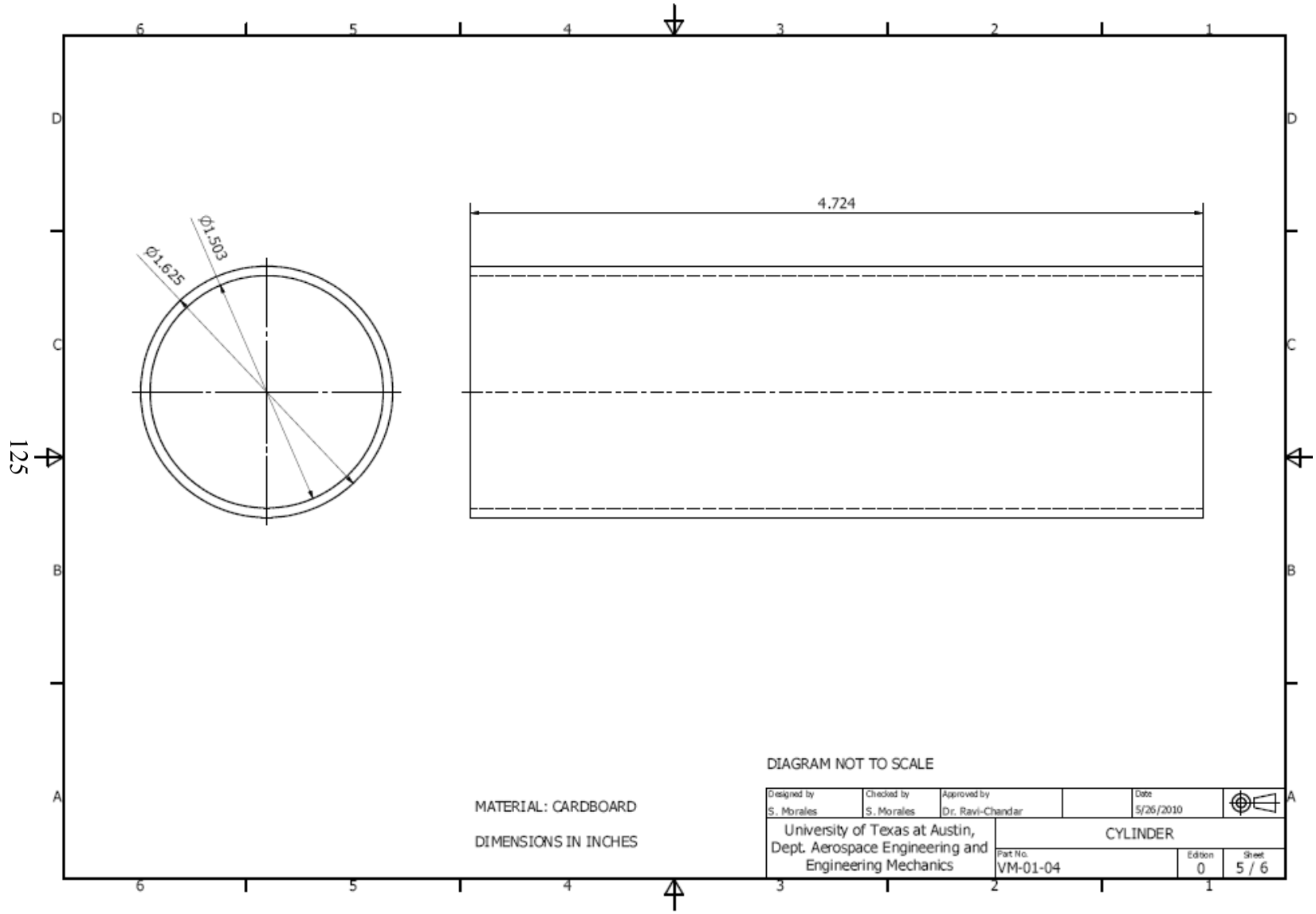
Ø1.503
Ø1.625
4.724
DIAGRAM NOT TO SCALE
MATERIAL: CARDBOARD
DIMENSIONS IN INCHES
Designed by S. Morales
Checked by S. Morales
Approved by Dr. Ravi-Chandar
Date 5/26/2010
University of Texas at Austin, Dept. Aerospace Engineering and Engineering Mechanics
CYLINDER
Part No. VM-01-04
Edition 0
Sheet 5 / 6

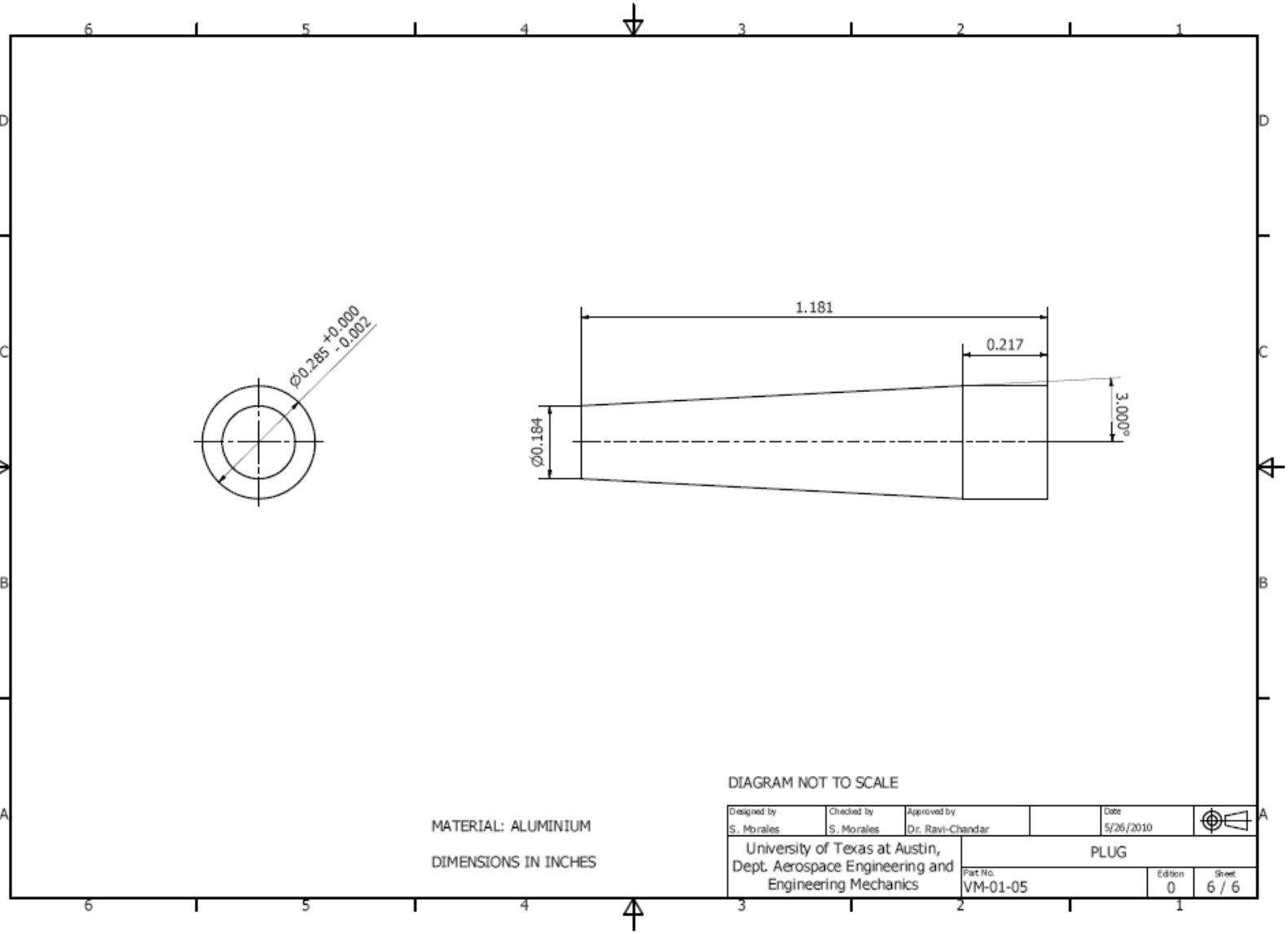
Ø0.285 +0.000 - 0.002
1.181
0.217
Ø0.184
3.000°
DIAGRAM NOT TO SCALE
MATERIAL: ALUMINIUM
DIMENSIONS IN INCHES
Designed by S. Morales
Checked by S. Morales
Approved by Dr. Ravi-Chandar
Date 5/26/2010
University of Texas at Austin, Dept. Aerospace Engineering and Engineering Mechanics
PLUG
Part No. VM-01-05
Edition 0
Sheet 6 / 6

References

Forrestal MJ, Duggin BW Butler RI (1980) An explosive loading technique for the uniform expansion of 304 stainless steel cylinders at high strain rates. J Appl Mech 47:17-20

Gourdin WH (1989) Analysis and assessment of electro-magnetic ring expansion as a high strain-rate test. J Appl Phys 65:411-422

Grady DE, Benson DA (1983) Fragmentation of metal rings by electromagnetic loading. Exp Mech 12:393-400.

Hopkinson B (1910) Collected Scientific Papers, Cambridge University Press

Hopkinson J (1872) Collected Scientific Papers, Cambridge University Press

Imbert J.M., Winkler S.L., Worswick M.J., Oliveira D.A., Golovashchenko S (2005) The Effect of Tool-Sheet Interaction on Damage Evolution in Electromagnetic Forming of Aluminum Alloy Sheet. Journal of Engineering Materials and Technology Vol. 127:145-153

Jansen J (1968) Some Measurements of the Expansion of a Metallic Cylinder with Electromagnetic Pulses. IEEE Transactions on Industry and General Applications Vol. IGA-4, No.4

Mathews W (2004) Services test spray-on vehicle armor, Army Times, May 3, 2004

Mock W, Hold WH (1983) Fragmentation behavior of Armco iron and HF-1 steel explosive-filled cylinders. J Appl Phys 54: 2344-2351

Mott NF (1947) Fragmentation of shell cases. Proc Roy Soc Lond, Series A 189:300-308

Niordson FI (1965) A unit for testing materials at high strain rates. Exp Mech 5:23-32

Oliveira D.A., Worswick M.J., Finn M, Newman D (2005) Electromagnetic forming of aluminum alloy sheet: Free-form and cavity fill experiments and model. Journal of Materials Processing Technology 170:350-362

Seth M, Vohnout V.J., Daehn G.S. (2004) Formability of steel sheet in high velocity impact. Journal of Materials Processing Technology 168:390-400

Takatsu N, Kato M, Sato K, Tobe T (1988) High-Speed Forming of Metal Sheets by Electromagnetic Force. JSME International Journal Series III Vol. 31 No. 1

Tang X, Prakash V, Lewandowski J (2005) Dynamic Deformation of Aluminum 6061 in Two Different Heat-treatments. SEM

Thomas J.D., Seth M, Daehn G.S., Bradley J.R., Triantafyllidis N (2007) Forming limits for electromagnetically expanded aluminum alloy tubes: Theory and experiment. Acta Materialia 55:2863-2873

von Karman T, Duwez P (1950) The propagation of plastic deformation in solids. J Appl Phys 21:987-994

Wesenbert DL, Sagartz MJ (1977) Dynamic fracture of 6061-T6 aluminum cylinders. J Appl Mech 44:643-646

Winter RT (1979) Measurement of fracture strain at high strain rates. Inst Phys Conf Ser 47:81-89

Zhang H, Ravi-Chandar K (2006) On the dynamics of necking and fragmentation: I. Real-time and post mortem observations in Al-6061-O. Int J Fract 142:183-217

Zhang H, Ravi-Chandar K (2008) On the dynamics of necking and fragmentation: II. Effect of material properties, geometrical constraints and absolute size. Int J Fract 150:3-36

Zhang H, Ravi-Chandar K (2009) On the dynamics of necking and fragmentation: III. Effect of cladding with a polymer. Int J Fract 155:101-118

Zhang H, Ravi-Chandar K (2010) On the dynamics of necking and fragmentation: IV. Expansion of Al 6061-O tubes. Int J Fract 163:41-65

Vita

Santiago Adolfo Morales was born in San José, Costa Rica, in 1984. After obtaining his International Baccalaureate at the British School of Costa Rica in December 2002, he entered the University of Costa Rica in March 2003. He received the degree of Bachelor of Science in Mechanical Engineering in October 2007. From January 2007 to June 2009 he was employed as a Design Engineer at TechShop International S.A., San José, Costa Rica. In August 2009, he entered the Graduate School at the University of Texas at Austin to pursue the degree of Master of Science in Aerospace Engineering.

Publications:

Morales SA, Albrecht AB, Zhang H, Liechti KM, Ravi-Chandar K (2011) On the dynamics of localization and fragmentation – V. Response of polymer coated Al 6061-O tubes. Int J Fract (submitted)

Permanent email: santiagomoraleszamora@gmail.com

This thesis was typed by the author.